Microwave plasma synthesis of nano-sized silicon carbide at atmospheric pressure

UNIVERSITEIT VAN PRETORIA
UNIVERSITY OF PRETORIA
YUNIBESITHI YA PRETORIA

JH van Laar

Department of Mechanical and Aeronautical Engineering

Faculty of Engineering, Built Environment and Information Technology

University of Pretoria

Supervisor: Prof JFM Slabber

Co-supervisor: Prof PL Crouse

Co-supervisor: Prof JP Meyer

2014

Acknowledgements

It is with much appreciation that I thank Prof PL Crouse in the Department of Chemical Engineering at the University of Pretoria for his financial support, guidance and time invested in this project. I also thank my spouse, Kelly, for her patience and love, and my colleague Sybrand “Hubbly King” Hagan who always listened and laughed with me. And of course a big thank you to both my parents for always encouraging and supporting me both financially and emotionally.

Furthermore, I acknowledge the South African National Research Foundation and the Department of Mechanical Engineering at the University of Pretoria for their financial support, as well as the South African Nuclear Energy Corporation for the use of its equipment, especially Dr J van der Walt for his contributions.

A final thank you to Prof JFM Slabber in the Department of Mechanical and Aeronautical Engineering for his help and guidance, and for inspiring me to continue my postgraduate education.

Abstract

The favourable physical and mechanical properties of silicon carbide (SiC) nanopowders allow application across many areas, including high-power, high-frequency electronics and high-temperature technologies. Many different synthesis methods for the creation of SiC nanoparticles have been studied, including carbothermic reduction, pulsed laser deposition, sol-gel processes, microwave heating and various plasma techniques.

Among the different synthesis methods reported in the literature, very few experiments investigate the microwave-induced plasma synthesis of SiC nanoparticles. The few reported studies show promising results with regard to particle size and production rate.

In this work, the synthesis of SiC nanoparticles from methyltrichlorosilane (MTS) is reported using a microwave-induced plasma, operating at atmospheric pressure.

The investigation was done experimentally using a 1 500 W power supply, a microwave generator operating at 2.45 GHz, a stub tuner, a waveguide and a sliding short. Quartz tubes were used, in which the plasma was generated and maintained. Hydrogen served as an added reductant for the conversion reaction, and argon served as the MTS carrier gas. The parameters studied were the H_2:MTS molar ratio and the total enthalpy, in the ranges 0 to 10 and 70 to 220 MJ/kg respectively.

X-ray diffraction studies confirmed the presence of β-SiC and optical emission spectrometry showed the majority of peaks to be that of elementary silicon, carbon and argon, indicative of MTS decomposition in the plasma. Scanning electron microscopy shows average individual particle sizes ranging between 50 and 135 nm, whereas transmission electron microscopy shows average

individual particle sizes ranging from 15 to 140 nm. Larger agglomerates are also present, ranging in sizes from 460 to 1 800 nm.

Through response surface methodology (RSM), it was shown that the optimum conditions for the production of nanoparticles lie within the range of enthalpy > 180 MJ/kg and H_2:MTS ratio of > 5.

Nomenclature

a_w	Waveguide wall length	m
b_w	Waveguide wall breadth	m
c	Speed of light	m s^{-1}
d	Tube diameter	m
d_p	Particle diameter	m
e	Electron charge	C
E	Electric field strength	V m^{-1}
E_H	Ionisation energy of hydrogen atom	eV
E_{max}	Maximum electric field strength	V m^{-1}
E_o	Electric field amplitude	V m^{-1}
f	Frequency	Hz
H	Enthalpy	J kg^{-1}
k	Boltzmann constant	m^2 kg s^{-2} K^{-1}
k_T	Thermal conductivity	W m^{-1} K^{-1}
L	Length of reaction zone	m
MW_i	Molecular weight of species i	kg $kmol^{-1}$
$\dot{m}_i$	Mass flow rate of species i	kg s^{-1}
m_e	Electron mass	kg
m_{final}	Final mass	kg
$m_{initial}$	Initial mass	kg

n_e	Electron density	m^{-3}
N	Avogadro's constant	mol^{-1}
N_N	Nitrogen doping concentration	m^{-3}
N_{Al}	Aluminium doping concentration	m^{-3}
P	Pressure	Pa
P_{abs}	Absorbed power	W
P_f	Forwarded power	W
P_{MW}	Microwave power	W
P_r	Reflected power	W
P_T	Total power	W
Q	Volumetric flow rate	$m^3\ s^{-1}$
Q_i	Volumetric flow rate of gas i	$m^3\ s^{-1}$
R	Ideal gas constant	$Pa\ m^3\ K^{-1}\ mol^{-1}$
$\dot{R}_{SiC}$	Rate of SiC production	$kg\ s^{-1}$
r	Particle radius	m
T	Temperature	K
T_e	Electron temperature	K
T_g	Gas temperature	K
T_H	Heavy particle temperature	K
t	Time	s
t_r	Residence time	s

v	Electron-neutral collision frequency	s^{-1}
V	Volume	m^3
Y	Yield	%
z	Charge acting on bound electron	C
Δm	Mass difference	kg
δ_s	Skin sheath thickness	m
ε_o	Vacuum permittivity	$F\ m^{-1}$
λ	Wavelength	m
λ_{crit}	Maximum wavelength	m
ρ	Density	$kg\ m^{-3}$
ω	Angular frequency	Hz
ω_e	Electron plasma frequency	Hz

Publications in journals and conference proceedings

The following articles and conference papers were produced during this research.

Journal articles

J.H. van Laar, J.F.M. Slabber, J.P. Meyer, I.J. van der Walt, G.J. Puts and P.L. Crouse, Microwave-Plasma Synthesis of Nano-sized Silicon Carbide at Atmospheric Pressure, Ceramics International, Volume 41, Issue 3, Part B, April 2015, Pages 4326–4333.

Conference posters

J.H. van Laar, J.F.M. Slabber, J.P. Meyer, I.J. van der Walt, G.J. Puts and P.L. Crouse, Microwave-Plasma Synthesis of Nano-sized Silicon Carbide at Atmospheric Pressure, *The 4th International Roundtable on Thermal Plasmas, for Industrial Applications*, Marrakech, Morocco, March 2014.

Acronyms and abbreviations

ANOVA	analysis of variance
APPJ	atmospheric pressure plasma jet
CCP	capacitively coupled plasma
CVD	chemical vapour deposition
DC	direct current
DBD	dielectric barrier discharge
DoE	design of experiment
HTCVD	high-temperature chemical vapour deposition
HTGR	high-temperature gas-cooled reactor
ICP	inductively coupled plasma
LTE	local thermodynamic equilibrium
LWR	light-water reactor
MTS	methyltrichlorosilane (CH_3SiCl_3)
PLD	pulsed laser deposition
RF	radio frequency
RSM	response surface methodology
SCCM	standard cubic centimetres per minute
SEM	scanning electron microscope/microscopy
TEM	transmission electron microscope/microscopy
TMS	tetramethylsilane
XRD	X-ray diffraction

Table of Contents

List of Figures

List of Tables

CHAPTER 1
Introduction

1.1 Background

The favourable physical and mechanical properties of silicon carbide (SiC) allow application across many areas, including high-power, high-frequency electronics and high-temperature technologies. Properties of interest include low bulk density, high strength, high thermal conductivity and refractive index, a wide bandgap and high-temperature semi-conductivity (Harris, 1995; Saddow & Agarwal, 2004).

The use of SiC in the nuclear industry, however, is gaining increased attention as a nuclear ceramic, due to its excellent mechanical properties and dimensional stability under irradiation and at high temperatures (Katoh *et al*., 2012). Whereas conventional carbide ceramics exhibit certain drawbacks, such as low ductility and high brittleness, nanopowders can easily overcome these shortcomings. With regard to nuclear applications, the use of SiC nanopowders also permit fast recovery of irradiation-induced defects (Leconte *et al*., 2008). SiC has been considered as a potential structural material for fission reactors, specifically light-water reactors (LWRs) and high-temperature gas-cooled reactors (HTGRs). SiC composites have been proposed as fuel cladding and fuel channel boxes in LWRs as a direct replacement for zirconium alloy-based cladding (Katoh *et al.*, 2012).

1.2 Problem statement

SiC nanoparticles have been shown to exhibit properties that differ substantially from that of the bulk material, encouraging the development of new areas of application. Many different synthesis methods for the creation of SiC nanoparticles have been studied. These include carbothermic reduction (Dhage *et al.*, 2009), pulsed laser deposition (Chrisey & Hubler, 1994), sol-gel processes (Li *et al*., 2000), microwave heating (Moshtaghioun Poyato *et al*., 2012; Satapathy *et al*., 2005), as well as different plasma techniques such as

inductive radio frequency (RF) (Károly *et al*., 2011; Ko *et al*., 2012; Sachdev & Scheid, 2001), direct current (DC) thermal (Kim & Lee, 2003) and low-pressure microwave plasmas (Lin *et al*., 2008). Only a few experiments have been reported on the microwave plasma synthesis of SiC nanoparticles under atmospheric pressure (Vennekamp *et al*., 2011). Operation at this pressure allows for the development of low-cost, less energy-intensive methods and smaller equipment footprints.

1.3 Objective

It is well known that, given the right conditions, methyltrichlorosilane (CH_3SiCl_3 or MTS) decomposes to form SiC. The particle growth kinetics and mechanisms of this reaction have been reported in the literature through chemical vapour deposition (Papasouliotis & Sotirchos, 2011; Sone *et al*., 2000) and pyrolysis investigations (Mousavipour *et al*., 2004). In this work, the synthesis of SiC nanoparticles from MTS, using a microwave-induced plasma operating at atmospheric pressure, is reported.

1.4 Experimental scope

MTS was used as precursor due to the benefit of having a stoichiometric silicon-to-carbon elemental ratio, and the relative ease of the procedure by which MTS can be fed into the system due to its naturally occurring liquid phase and high volatility. Hydrogen served as an added reductant for the conversion reaction. The process parameters studied were the H_2:MTS molar ratio and the total enthalpy while operating at atmospheric pressure in an argon/hydrogen environment. Argon served as the MTS carrier gas.

1.5 Overview

The three chapters indicated below will highlight the relevant literature. Chapter 2 is a brief overview of the fundamentals of plasma physics and various plasma technologies used in the production of new materials. Chapter 3 discusses the properties and characteristics of bulk and nano-SiC, and expands on several synthesis methods. Chapter 4 is a more focused discussion of the current plasma-assisted methods for the production of SiC nanoparticles, specifically microwave plasma methods.

Chapter 5 discusses the experimental procedure and equipment used for the study. This is followed by the results and discussion section in Chapter 6, where the various findings and their interpretations are reported. Chapter 7 will give a brief summary of the results and recommendations that were established during the preceding sections of the report.

CHAPTER 2

Plasma technology: A review

2.1 Introduction

The goal of this chapter is to familiarise the reader with the fundamental aspects of plasma physics, as well as to introduce various plasma technologies based on their operating conditions and frequencies. Sections 2.2 and 2.3 will briefly explain basic plasma concepts and terminology used in the industry, followed by the classification of plasmas according to their energy supply and operating parameters in sections 2.4 to 2.5. Section 2.6 will attempt to focus the discussion on microwave-induced plasmas and their generation.

2.2 Introduction to plasma

Plasmas are generally seen as the fourth state of matter and constitute more than 99% of the universe. A plasma is often described as an ionised gas due to its composition of electrons, ions and neutral atoms in fundamental and excited states. Plasmas are chemically active, electrically conductive and can occur at either low or high temperatures, known as cold or thermal plasmas respectively. This wide temperature range enables numerous plasma applications, which include materials processing, chemical synthesis, thermonuclear synthesis, waste management and surface treatments (Tendero *et al*., 2006). A few basics and fundamentals are discussed, followed by a brief summary of the different kinds of plasmas, including properties, working conditions and applications.

2.3 Plasma generation

Plasmas are generated by supplying energy to a neutral gas. When electrons or photons with sufficient energy collide with neutral atoms and molecules, charge carriers (electrons and ions) are formed through electron-impact ionisation or photo-ionisation. Energy can be supplied in various ways, but the

dominant processes involve thermal, electric or electromagnetic radiation. The most common methods used for generating and sustaining low-temperature plasmas in the laboratory involve the application of electric fields to a neutral gas. The electric field accelerates the gas electrons and this energy is then transmitted to the neutral species by collisions with atoms and molecules. This leads to a chain reaction of elastic and inelastic collisions that is eventually balanced by charge carrier losses, and this process results in a steady-state plasma (Conrads & Schmidt, 2000).

2.4 Plasma classification

The properties of plasma vary with electron density and temperature. These parameters change, based on the type of energy supply and the amount of energy transferred to the plasma. Figure 1 shows the different categories based on the abovementioned parameters.

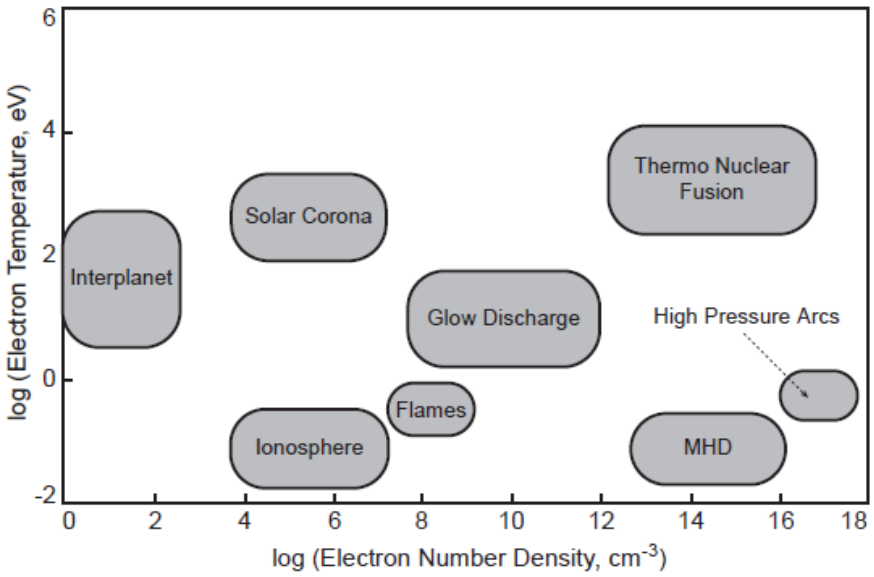

Figure 1: Classification of plasmas (Fridman, 2008:3)

Using this classification, a distinction is made between the following:

- Local thermodynamic equilibrium (LTE) plasmas, also known as thermal plasmas
- Non-local thermodynamic equilibrium (non-LTE) plasmas

2.4.1 LTE plasmas

A plasma is considered to be in LTE (thermal) when the electron temperatures are close to the heavier particle temperatures. The temperature difference between electrons and heavier particles is proportional to the square of the ratio of the electric field (E) to the pressure (P):

$$\Delta T \propto \left(\frac{E}{P}\right)^2 \tag{2.1}$$

Only in the case of small values of E/P do the temperatures of electrons and heavier particles approach each other (Fridman, 2008:4). LTE also requires chemical reactions to be governed by collisions only and not by radiative processes, that collision phenomena have to be micro-reversible, and that diffusion time must be sufficient for particles to reach equilibrium (Tendero *et al.*, 2006).

According to Griem (1963), for LTE the collision rate should be at least ten times larger than the radiative rate. Thus, for optically thin homogeneous plasmas:

$$n_e = 9.2 \times 10^{17} z^7 \left(\frac{kT}{E_H^Z}\right)^{\frac{1}{2}} \left(\frac{E_2 - E_1}{E_H^Z}\right)^3 \tag{2.2}$$

where:

- z is the charge acting on the bound electron
- $E_2 - E_1$ is the energy gap between the ground state and excited level
- E_H = 13.58 eV is the ionisation energy of the hydrogen atom

The abovementioned rules for LTE are very restricting; therefore most plasmas deviate from LTE, especially in the laboratory.

2.4.2 Non-LTE plasmas

Numerous plasmas exist far from thermodynamic equilibrium (non-thermal) and are characterised by multiple temperatures related to different plasma particles. This can also be described as a departure from Boltzmann distribution patterns for the density of excited atoms. It is, however, the electron temperature, in particular, that often differs significantly from that of heavier particles (T_e >> T_H). With regard to the huge mass difference between electrons and heavier particles, T_g is determined by T_H (Tendero *et al.*, 2006). In many non-thermal plasma systems, $kT_e \approx$ 1 eV (about 10 000 K), whereas T_g is close to room temperature (Fridman, 2008:5).

Non-thermal plasmas are usually generated at low pressures or low power levels. Thermal plasmas are usually more powerful, whereas non-thermal plasmas are more selective. These characteristics affect the engineering aspects and application areas of these two types of plasmas.

2.5 Atmospheric pressure plasmas

Plasmas that operate at low pressures (10^{-4}–10^{-2} kPa) are non-thermal. The heavy-particle temperatures are much lower than those of the electrons, and the inelastic collisions between electrons and heavy particles are dominated by excitation or ionisation, which does not affect the heavy-particle temperatures. As pressure increases, however, collisions intensify, which induces plasma chemistry and the heating of the heavy particles. The difference between T_e and T_H thus decreases, pushing the plasma towards LTE. The property gradients in the plasma, however, restrict the particles from reaching complete equilibrium (Tendero *et al.*, 2006).

Excitation frequencies are very important, as they influence the behaviour of the electrons and ions, and the different plasma sources can be classified according to the excitation mode (Tendero *et al.*, 2006):

- Direct current (DC) discharges
- Radio frequency discharges
- Microwave discharges

In the following sections, various plasma sources will be discussed.

2.5.1 Direct current discharges

Non-thermal plasmas in DC discharges can be created in closed vessels using interior electrodes. Depending on the voltage and current in the discharge, different types of plasma may be obtained, as shown in Figure 2.

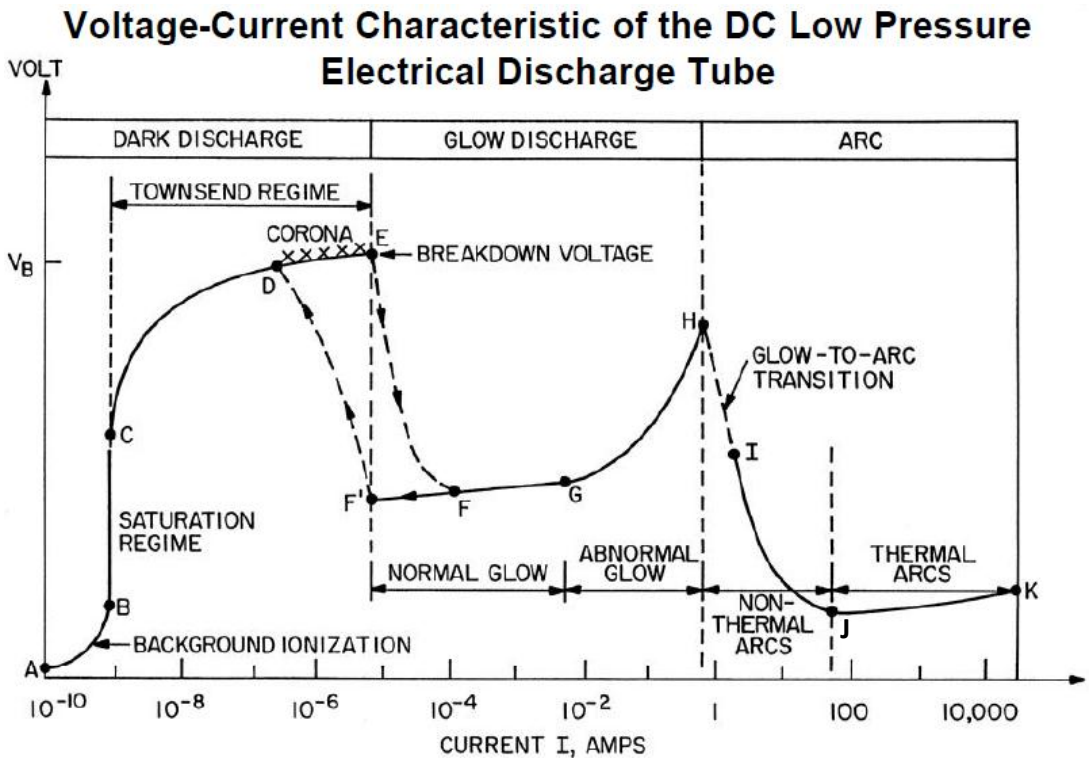

Figure 2: Different discharge regimes for current vs voltage curve

At low currents (A–B), the electric field is not strong enough to generate a self-sustained plasma discharge. Only naturally free electrons become ionised by background radiation that originates from cosmic rays, radioactive minerals or other sources (Payling, 2013). When the potential difference is increased further, the current becomes saturated. In this saturation region (B–C), the current remains constant while the voltage is increased. The gas becomes more ionised due to a constant increase in electric field strength, thus energising more electrons.

Beyond point C, the current rises exponentially until it reaches point E. This region is known as the Townsend regime. The electric field is now high enough for the initial electrons present in the gas to acquire sufficient energy to ionise a neutral atom, thus creating more charged particles (Fridman, 2008: 177). At point D, a corona discharge is generated due to a strong electric field present at the tip of the electrodes. This discharge can often be luminous, resulting in an incorrect classification as a glow discharge.

The corona discharge region is more strongly influenced by the electric field around the electrodes than the electric potential across the electrodes. Electrical breakdown finally occurs when the ions reaching the cathode have sufficient energy to generate secondary electrons that help to self-sustain the discharge. This results in the initial generation of the glow discharge. The breakdown voltage for any particular gas is determined using Paschen's Law (Paschen, 1889). The entire region (A–E) is termed a dark discharge because, except for corona discharges and the breakdown itself, the discharge remains invisible to the eye (Payling, 2013).

As the current is increased further, the electron energy and number density become high enough to generate excited gas atoms through collisions. These atoms eventually relax to their ground state by the emission of photons, resulting in a luminous glow. The glow discharge regime consists of two sub-

regimes, namely normal glow (F–G) and abnormal glow (G–H). Normal glow is characterised by a constant voltage and a continuous increase in current over several magnitudes. This is accompanied by an increase in the diameter of the discharge.

When the discharge covers the entire surface of the cathode, the only way in which the total current can increase further is to increase the current density, which requires more energy. This, in turn, applies more voltage, and the system moves away from the Paschen minimum (Paschen, 1889). This regime (G–H) is named the abnormal glow regime and is characterised by a significant increase in voltage with an increasing current. The abnormal glow discharge differs from the normal discharge only in brightness; the abnormal glow being brighter. The average ion energy of particles bombarding the cathode surface also increases due to the increase in voltage and cathode current density. This bombardment ultimately heats the cathode and causes thermionic emission. At this point, when the cathode is hot enough to emit electrons thermionically, the discharge changes to an arc regime (H–I) (Payling, 2013).

The arc regime (I–K) is one where the discharge voltage decreases with an increasing current until large currents are achieved at point J. The voltage again increases slowly with the increasing current (Payling, 2013).

2.5.1.1 The glow discharge

The glow discharge is the best-known type of non-thermal discharge and is widely used in plasma chemistry. The term “glow” indicates the presence of luminosity in contrast to the dark discharge. The glow discharge is usually defined as a self-sustained DC discharge that emits electrons as a result of secondary emission mostly induced by positive ions (Fridman, 2008: 175). The simplest configuration consists of two parallel electrode plates, a cathode

and an anode, at different electrical potentials. Once the glow discharge is established, the potential varies throughout the plasma, with certain regions having a higher potential than others. The electric field is usually stronger in the vicinity of the cathode and the anode. As shown in Figure 3, three major regions can be distinguished in the discharge: the cathode region, the glow regions and the anode region.

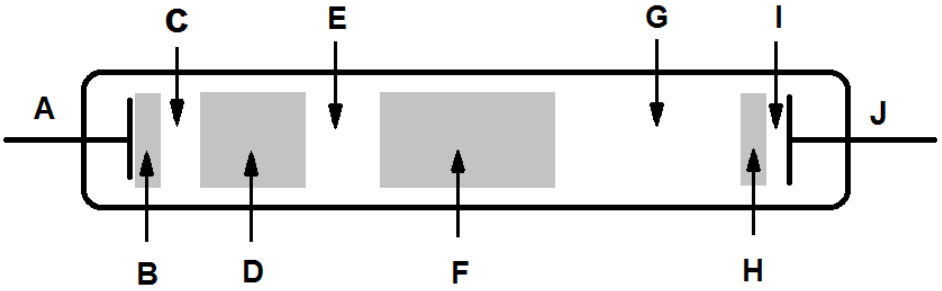

Figure 3: Glow discharge regions

Along the discharge tube, a sequence of dark and luminous layers appears. The sizes of these layers are proportional to the electron mean free path, and hence inversely proportional to pressure. It is therefore easier to observe these patterns at lower pressures. Special names were given to each layer, mainly due to the differing characteristics. Immediately next to the cathode (A) is a dark layer called the Aston dark space (B). Then there is a thin layer named the cathode glow (C), immediately followed by the cathode dark space (D). This is followed by the negative glow (E), which is clearly separated from the dark cathode space. The negative glow becomes less bright towards the anode and enters the Faraday dark space (F). This is followed by the positive column (G), which is also bright (although less than that of the negative glow), long and uniform. Closer to the anode, the positive column becomes the anode dark space (H) and finally enters the region of anode glow (I) next to the anode (J).

2.5.1.2 Arc plasma torches

An arc plasma torch consists of the following components:

- A cathode where electrons are emitted
- A plasma gas injection system
- A nozzle to confine the plasma

As shown in Figure 4, two types of arc torches are currently used, namely the non-transferred arc and the transferred arc. In non-transferred arc torches, the nozzle acts as the positively charged anode. For the transferred arc torch, however, the treated material acts as the anode and the nozzle merely serves as floating potential (Tendero *et al.*, 2006).

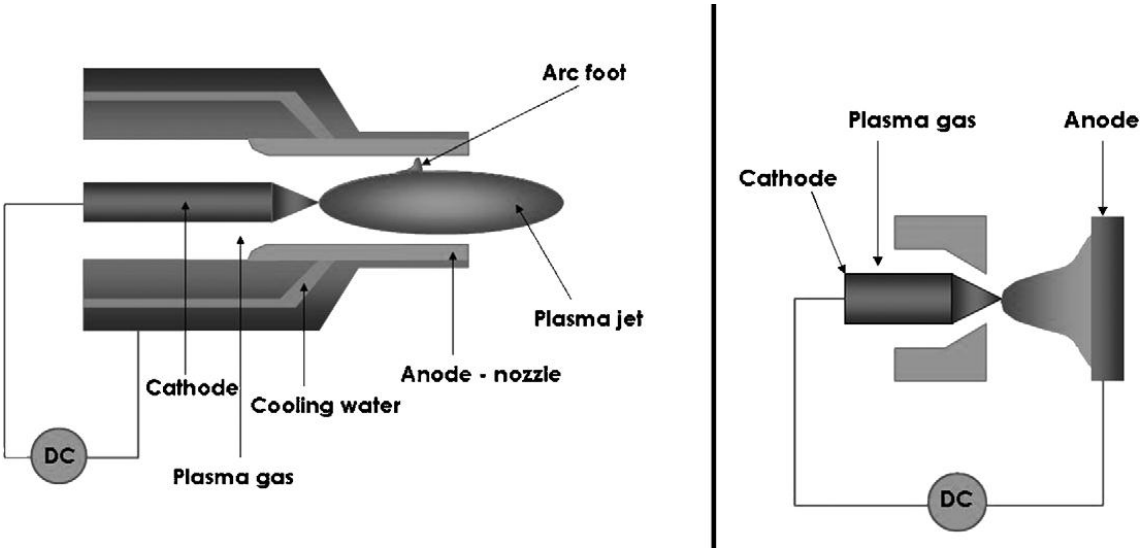

Figure 4: A non-transferred arc (left) and a transferred arc (right) (Tendero *et al.*, 2006)

An arc is ignited between the anode and the cathode, and the gas becomes ionised. Plasma temperatures may reach up to 15 000 K, which allows for high-temperature applications of the arc plasma. Gas velocities vary between 600 and 2 300 m/s and the particles are usually injected radially (Fauchais,

2004). Conventionally, the cathode is made of thoriated tungsten and the anode nozzle is made of high-purity copper, often with sintered tungsten. The arc column develops from the cathode tip and attaches to the anode. The attachment to the anode continuously fluctuates in length and position due to movements induced by the drag force of the gas flowing to the colder boundary layer and magneto-hydrodynamic forces induced by the plasma arc (Fauchais, 2004). Some studies are being undertaken to improve the nozzle design (Cao *et al*., 1997) to obtain more uniform temperature and velocity distributions.

2.5.1.3 Corona discharge

A corona is a weak luminous discharge appearing at atmospheric pressure at points where the electric field is sufficiently large, such as sharp points, edges or thin wires. Charged particles are dragged by the weak electric fields from one electrode to another to close the electric circuit (Fridman, 2008: 233), as shown in Figure 5.

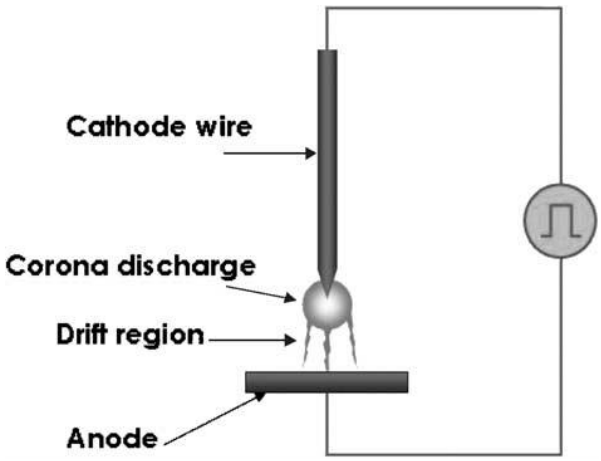

Figure 5: Corona discharge principle (Tendero *et al.*, 2006)

Applications of continuous coronas are limited by their low current and power. It is possible to increase corona power by using pulse-periodic voltages (the DC power supply is pulsed). When a highly negative voltage is applied, a negative corona is discharged. Positive ions are accelerated, and secondary electrons are emitted. These electrons undergo inelastic collisions with

heavier particles, and this process induces the formation of chemically reactive species. When the pulse ends, the corona is extinguished before it becomes too conductive, and in so doing, the transition towards spark is avoided (Tendero *et al.* 2006; Fridman, 2008: 234–235).

2.5.1.4 Dielectric barrier discharge

The dielectric barrier discharges (DBDs), also known as silent discharges, consist of two parallel plates serving as electrodes (Figure 6). At least one of these plates is covered by a dielectric layer. The electrodes are separated by a small gap, usually limited to a few millimetres, to ensure stable operation (Tendero *et al.*, 2006). The plasma is ignited by either a pulsed or sinusoidal power source operating at frequencies of 0.05 to 500 kHz (Fridman, 2008: 237–239). The discharge can be either filamentary (Massines & Gouda, 1998) or a glow (Yokoyama *et al*., 1990), depending on gas composition and voltage. DBDs cannot operate by using DC voltages, as the capacitive coupling of the dielectric layer requires an alternating electric field (Kogelschatz, 2000). Alternatively, a cylindrical configuration can be used, which is also shown in Figure 6.

The most important characteristic of a DBD is the fact that non-LTE plasma conditions can easily be obtained at atmospheric pressure for different gases without the need for sophisticated pulse power supplies. DBDs are also extremely flexible with regard to geometrical shape, operating medium and operating parameters (Kogelschatz, 2000).

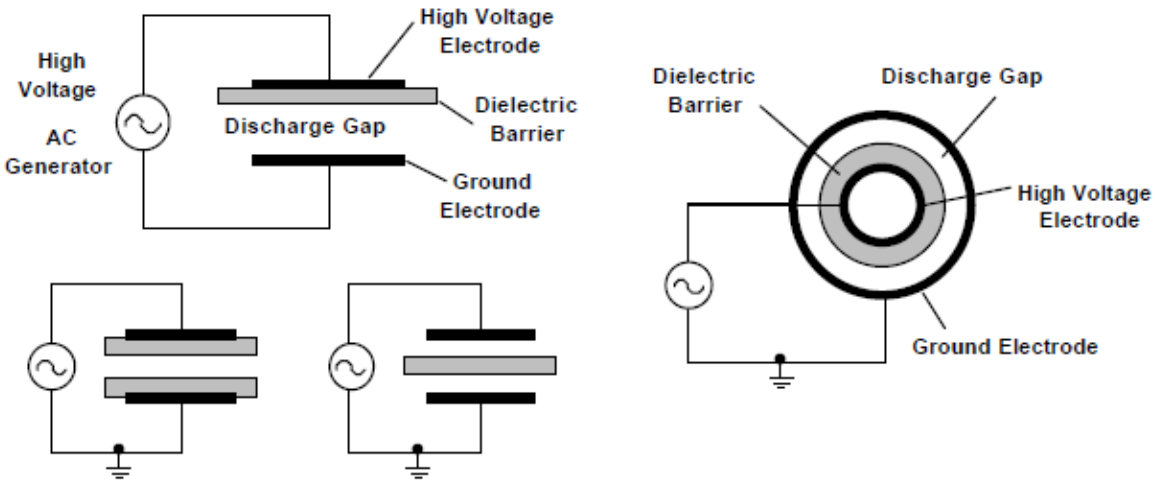

Figure 6: DBD configurations (Kogelschatz *et al*., 1997)

Historically, DBDs have been used for ozone generation, and the first experimental investigations were reported by W Siemens (Kogelschatz, 2003). Other applications include UV sources and excimer lamps, polymer treatment, pollution control, medical applications and use in CO_2 lasers (Kogelschatz, 2000; Fridman, 2008; Kogelschatz, 2003). Current uses being investigated include a combination of DBDs and special catalytic substances to enhance the selectivity of plasma chemical reactions (Yao *et al*., 2009).

2.5.2 Radio frequency discharges

Plasmas can be generated at high power levels and atmospheric pressure through the use of RF discharges. Despite the increased cost of this method, different types of RF discharges are gaining increasing popularity due to the absence of any direct electrode-plasma contact. In fact, in many of these discharge systems there are no electrodes at all, and therefore no electrode-related problems (Fridman & Kennedy, 2004: 594). The RF electric field interactions with the plasma can be either inductive or capacitive.

2.5.2.1 Inductively coupled RF discharges

One of the older known forms of plasma generation, the inductively coupled plasma (ICP) is excited and maintained by an RF-fed helical coil. The principle of the ICP generation is illustrated in Figure 7. High-frequency electric current is passed through a solenoid coil, where a magnetic field is induced along the axis of the discharge tube. The resulting electric field accelerates the electrons and thus maintains the plasma (Tendero *et al.*, 2006). ICPs can be very powerful and are capable of generating and maintaining plasmas at atmospheric pressures and higher.

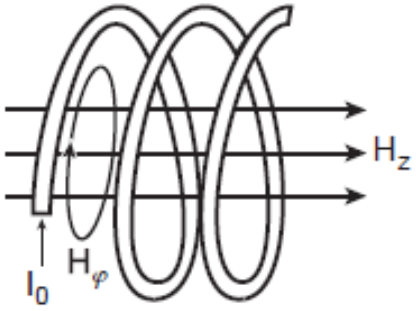

Figure 7: Generation principle of ICP (Fridman, 2008: 209)

Different variations of this principle include ICP torches and the IST system (named after the IST Society), which is a DBD adaptation (Tendero *et al.*, 2006).

2.5.2.2 Capacitively coupled discharges

Capacitively coupled plasmas (CCPs) generate higher values for the electric fields than ICPs do. As in a capacitor, the electric field is now the primary effect. These higher electric field values make it possible to generate non-LTE plasmas that are used in material treatment such as electronics (Fridman & Kennedy, 2004: 607). Some variations include the atmospheric pressure plasma jet (APPJ) (Schutze *et al.*, 1998), the cold plasma torch (Koinuma *et al.*, 1992) and microplasmas (Tendero *et al.*, 2006).

2.5.3 Microwave discharges

Microwave systems are electrode-less and the same principle applies to all variations. Microwaves are guided along the system, through some form of metallic waveguide, and transmit energy directly to the plasma gas electrons. Whereas RF discharges operate with wavelengths of approximately 22 m, microwave plasmas are sustained by electromagnetic waves in the centimetre range, which is comparable to the size of the physical system (Tendero *et al.*, 2006). This form of plasma generation will be discussed further in the following sections.

2.6 Microwave-induced plasmas

Microwave generators, in particular magnetrons operating in the gigahertz frequency range and with a power of 1 to 2 kW, are able to maintain LTE microwave discharges at high pressures (typically atmospheric). Various possibilities exist through which the electromagnetic energy in the discharges can be coupled with the plasma, the most typical of which is through the use of waveguides, shown in Figure 8. Plasma is ignited and maintained inside a tube that crosses the rectangular waveguide and is transparent to electromagnetic waves, usually quartz (Fridman, 2008: 211).

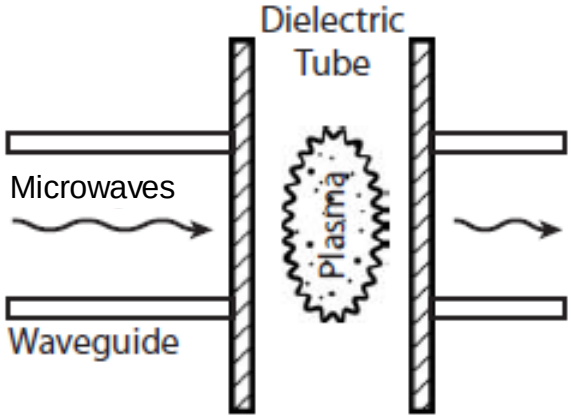

Figure 8: Microwave plasma in a waveguide (Fridman, 2008: 211)

Within this waveguide, different modes of electromagnetic wave propagation can be used to initiate and maintain the microwave discharges, the most common being H_{01} mode in rectangular waveguides, illustrated in Figure 9. In this mode, the electric field moves parallel to the narrow walls of the waveguide and its maximum, E_{max}, is related to microwave power, $P_{MW,}$ through Equation 2.3:

$$E_{max}^2 = \frac{1.51P}{a_w b_w}\left[1 - \left(\frac{\lambda}{\lambda_{crit}}\right)^2\right]^{-\frac{1}{2}} \quad (2.3)$$

Where λ_{crit} is the maximum wavelength when propagation is still possible ($\lambda_{crit} = 2a_w$). In this case, the electric field has a maximum in the centre of the discharge tube, making this mode of plasma generation extremely convenient (Fridman, 2008: 211–212).

The waveguide dimensions are usually related to the microwave frequency: in the case of f = 2.5 GHz (λ = 12 cm), the wider waveguide wall should be longer than 6 cm (normally 7.2 cm). The narrower waveguide wall is typically 3.4 cm long, and the quartz tube diameter is about 2 cm. When the microwave power at atmospheric pressure spans the range of 1 to 2 kW, the molecular gas temperatures vary between 4 000 and 5 000 K (Fridman & Kennedy, 2004: 610–611).

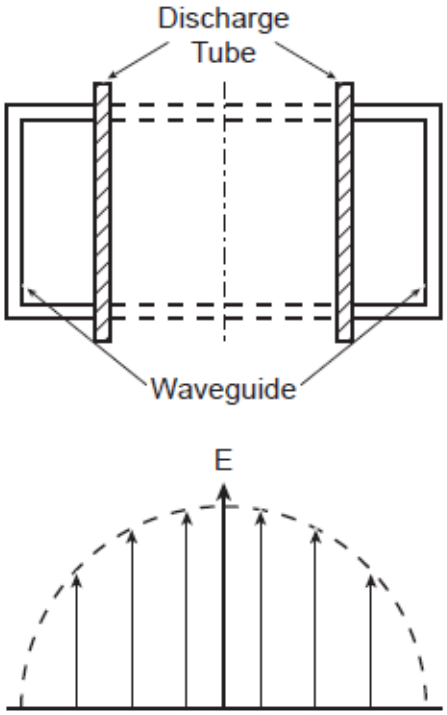

Figure 9: H_{01} mode electric field distribution (bottom) in a rectangular waveguide cross-section (top) (Fridman, 2008: 212)

Any interaction between the electromagnetic wave and the plasma results in both the dissipation and reflection of the wave. Approximately half of the incident microwave power is dissipated in the plasma, one quarter is transmitted, and another quarter is reflected. To increase the coupling effectiveness, the transmitted wave can be reflected back, resulting in the formation of a standing wave. Coupling techniques like this one help to increase the fraction of energy absorbed in the plasma by 90 to 95% (Fridman & Kennedy, 2004: 612).

2.6.1 Power absorption

The equation used for power absorption in high-frequency discharges (Conrads & Schmidt, 2000), per unit volume, is given as:

$$\frac{P_{abs}}{V} = \frac{1}{2} n_e \frac{e^2}{m_e v} \frac{v^2}{v^2+\omega^2} E_o^2 \tag{2.4}$$

This relation is highly dependent on the electron-neutral collision frequency (gas pressure and composition). Reflected electromagnetic waves will be those with frequencies below the electron plasma frequency, given by:

$$\omega_e = \left(\frac{e_o^2 n_e}{\varepsilon_o m_e}\right)^{\frac{1}{2}} \tag{2.5}$$

The electron density, n_e, that corresponds to this frequency is known as the cut-off density (Conrads & Schmidt, 2000). The most commonly used frequency in microwave systems is f = 2.45 GHz, and at this frequency the corresponding cut-off density of the electrons is approximately 10^{11} cm^{-3}. At this point, the skin effect allows penetration of the wave into the plasma to a certain extent. P_{abs} is limited to the thickness of the skin sheath, δ_s, and in the case of $v >> \omega$, this skin depth is given by:

$$\delta_s = \sqrt{2c}\left(\frac{\varepsilon_o m_e v}{e^2 n_e \omega}\right)^{\frac{1}{2}} \tag{2.6}$$

Power absorption inside the skin sheath is transferred into the plasma region through waves below the cut-off frequency (Conrads & Schmidt, 2000).

2.6.2 Operation and configurations

Microwave systems all follow the same principle, i.e. microwaves are guided along a system and transmit energy directly to the gas electrons. As the electrons gain energy, they start undergoing elastic collisions with heavier particles. The higher mass of the heavy particles allows them to remain static, and therefore allows the electrons to gain kinetic energy with each collision until they have enough energy to initiate inelastic excitation or even ionisation

collisions. Eventually the gas becomes partially ionised, which leads to plasma formation (Tendero *et al.*, 2006).

Most microwave plasma systems consist of the same components:

- Microwave power supply
- Ignition system
- Gas injection
- Other equipment, e.g. waveguide, tuning systems (Tendero *et al.*, 2006)

Other subsystems include an applicator, which optimises energy transfer and minimises reflected power, and the circulator, which protects the power supply from reflected power (Conrads & Schmidt, 2000).

Other configurations of the microwave plasma system can be found in the literature. Examples include the microwave plasma torch (Moisan *et al*., 1994), resonant structures – such as the Beenakker cavity (Beenakker, 1976) – and the microstrip plasma (Bilgic *et al*., 2000).

2.7 Summary

In this chapter, the concepts of fundamental plasma physics and terminology were introduced, the different classifications of plasmas based on their energy supply and operating parameters were discussed, and the mechanism of microwave plasma generation was introduced.

CHAPTER 3

Silicon carbide:

Properties and synthesis

3.1 Introduction

In this chapter, the material SiC will be broadly discussed and a brief overview of its properties and characteristics will be presented, as well as various synthesis methods currently being investigated. A short history of SiC's discovery and large-scale manufacturing will be given in sections 3.2 and 3.3, followed by a discussion of its numerous crystalline forms and properties in sections 3.4 to 3.7. The chapter is concluded with a brief overview of various synthesis methods of SiC, including microwave plasma, in section 3.8.

3.2 History

Jöns Jacob Berzelius is best known for the discovery of silicon (Si). He was most likely the first person to synthesise silicon carbide (SiC). In 1824, he published a paper in which he reported that he suspected that a chemical bond existed between silicon (Si) and carbon (C) in one of the samples he produced (Saddow & Agarwal, 2004: 4–5).

Years later, Edward Goodrich Acheson, while trying to produce minerals that would serve as substitutes for diamonds, discovered SiC by mixing coke and silica in a furnace. He found a crystalline product characterised by extreme hardness, refractability and infusibility, which was shown to be a compound of carbon and silicon. Acheson called his product "carborundum" and gave it the correct formula: SiC (Saddow & Agarwal, 2004: 5–6). In 1892, Henri Moissan found natural SiC in the Canyon Diablo meteorite in Arizona, USA, which is the origin of the mineral name for silicon carbide: moissanite (Can, 2004).

On 28 February 1893, Acheson patented a method for making carborundum on an industrial scale, now known as the Acheson process. This process is still used today and involves the reaction between high-purity quartz (99.5%

SiO_2) and petroleum coke in an electrically heated resistance furnace (Can, 2004).

In 1955, another crystal growth invention was made by JA Lely. He provided an environment for the growth of crystals similar to that of the Acheson process. With Lely's method, the crystal purity and properties could, to some extent, be controlled, which led to renewed interest in SiC (Saddow & Agarwal, 2004: 6).

3.3 Acheson process

Nowadays, most of the silicon carbide powder is manufactured using the Acheson process. The resultant powder is characterised by a large particle size and consists of mostly alpha silicon carbide (α-SiC). The reaction used during the Acheson process is shown in Equation 3.1:

$$SiO_2 + 3C \rightarrow SiC + 2CO \qquad (3.1)$$

The temperatures used are between 1 600 °C and 2 500 °C, and the process takes place in furnaces up to 25 m long, 4 m wide and 4 m high. It produces silicon carbide crystals, which are then milled and purified to obtain a commercial-grade silicon carbide powder (Can, 2004). This powder can undergo different sintering mechanisms to produce different silicon carbide materials (Smith, 1991). The Acheson process sometimes also includes sawdust and salt in lesser amounts, together with the coke and silica. The sawdust creates channels that help impurities escape and the salt creates free chorine, which reacts with metal impurities that become volatile (Saddow & Agarwal, 2004: 5).

3.4 Crystalline forms

Silicon carbide is similar in its structure and properties to the diamond phase of graphite, with the exception that diamond, with a single species of atom, can only occur in cubic form. Silicon carbide, however, has an endless array of stacking sequences with face-centred cubic and hexagonal being the most common (Voice, 1970). In 1944, NW Thibault proposed that cubic silicon carbide be named beta SiC (β-SiC), and that the hexagonal varieties that occur be grouped as alpha SiC. There have been many objections to this nomenclature; the main reason being that it does not conform to phase diagram practice. Thibault's nomenclature, however, has proved so convenient that it has generally been accepted by crystallographers and mineralogists (Baumann, 1952).

Another widely used and more specific nomenclature for the crystalline form is given in the form XY, where X is the number of layers before the sequence repeats itself, and Y determines the resulting structure of the crystal: C for cubic, H for hexagonal, and R for rhombohedral.

Silicon carbide exhibits a two-dimensional polymorphism called polytypism. All polytypes have a hexagonal frame of SiC bilayers. The hexagonal frame should be viewed as sheets of spheres of the same radius and the radii touching, as illustrated in Figure 10. The sheets are the same for all lattice planes. However, the relative position of the plane directly above or below is shifted somewhat to fit into the “valleys” of the adjacent sheet in a close-packed arrangement. Hence, there are two inequivalent positions for the adjacent sheets. By referencing the possible positions as A, B and C, one can begin constructing polytypes by arranging the sheets in a specific repetitive order. Thus, the only cubic polytype in SiC is 3C-SiC, which has the stacking sequence ABCABC… (Saddow & Agarwal, 2004).

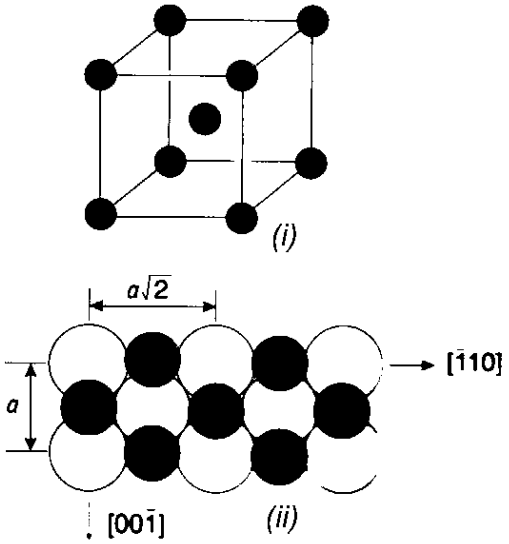

Figure 10: i) BCC unit cell and ii) stacking sequence (Hull & Bacon, 2001)

In Figure 10, the two layers of atoms are shown respectively by large white circles and smaller black circles. The two types of atoms are, however, actually the same size and the differences in diameter of the circles are only for the purpose of clarity.

The simplest hexagonal structure that can be built is 2H, shown in Figure 11, which has a stacking sequence of ABAB…

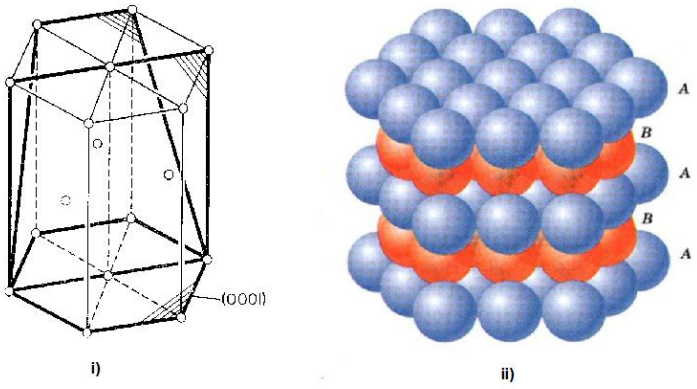

Figure 11: i) Hexagonal unit cell and ii) stacking sequence (Hull & Bacon, 2001)

The two important polytypes, 6H-SiC and 4H-SiC, have stacking sequences of ABCACBABCACB… and ABCBABCB…, respectively (Saddow & Agarwal, 2004).

3.4.1 Alpha SiC

The main source of alpha SiC is the Acheson process. Alpha SiC occurs in at least ten different crystalline forms. The first development of the alpha SiC crystalline phase occurs at 2 100 °C (Baumann, 1952).

3.4.2 Beta SiC

The formation of Beta SiC from silica-carbon mixtures always begins near 1 500 °C and is complete at or near 1 800 °C. At 2 100 °C, anisotropic areas may be observed, indicating the beginning of alpha SiC formation (Baumann, 1952).

3.5 Formation of SiC

Commercial silicon carbide is always manufactured from a mixture of silica, sand and some form of carbon low in ash. The chemical reaction is generally represented as shown in Equation 3.2:

$$SiO_2 + 3C \rightarrow SiC + 2CO \qquad (3.2)$$

The reaction begins above 1 500 °C and, under certain conditions, is complete at 1 800 °C (Baumann, 1952).

The reaction shown in Equation 3.3 has been carried out in various time-temperature experiments and is used in the manufacture of a form of siliconised silicon carbide:

$$Si + C \rightarrow SiC \quad (3.3)$$

This reaction is thermodynamically feasible even at room temperature. When using chemically pure silicon and carbon in stoichiometrical proportions, silicon carbide will not form until the melting point of silicon (1 430 °C) is reached. The reaction to form silicon carbide from silica and carbon mixtures always begins near 1 500 °C. It is a two-step reaction, the first step being the reduction of silica to silicon, and the second reaction being silicon carbide formation. The latter is almost instantaneous in most cases (Baumann, 1952).

Primary SiC formed under most conditions is always beta SiC. Beta SiC is stable up to 2 100 °C and begins to transform monotropically to alpha SiC slowly at 2 100 °C. It changes to the alpha SiC structure rapidly and completely at 2 400 °C. The percentage of beta SiC converted to alpha SiC is usually in the order of 5% (Baumann, 1952).

3.5.1 Sublimation growth

In the late 1970s, the seeded sublimation growth was made in Russia by Tairov and Tsvetkov (Harris, 1995). Unlike the Lely and Acheson processes, where the growth is conducted under uniform temperatures, Tairov and Tsvetkov introduced a seed crystal and forced material transport from the source to the seed by a thermal gradient. The growth rates increased markedly and seeds of larger diameters and lengths could be made. The produced boules could be sliced and polished and the SiC wafer was born.

The technique is almost exclusively used today to manufacture SiC wafers. As shown in Figure 12, a graphite crucible is partially filled with SiC powder and a “seed” is attached at the top of the crucible. The whole system is closed and heated up to temperatures above which SiC starts to sublime considerably. A thermal gradient is applied such that the seed is slightly colder than the

powder source. Material will thus transport from the source to the seed, where it will condense. The principal constituents during sublimation are Si, Si_2C, and SiC_2 and the ratio between them is determined by the temperature (Saddow & Agarwal, 2004).

Typical parameters that affect crystal growth rate and quality are seed temperature, source temperature, temperature gradient between seed and source, and ambient pressure (Harris, 1995).

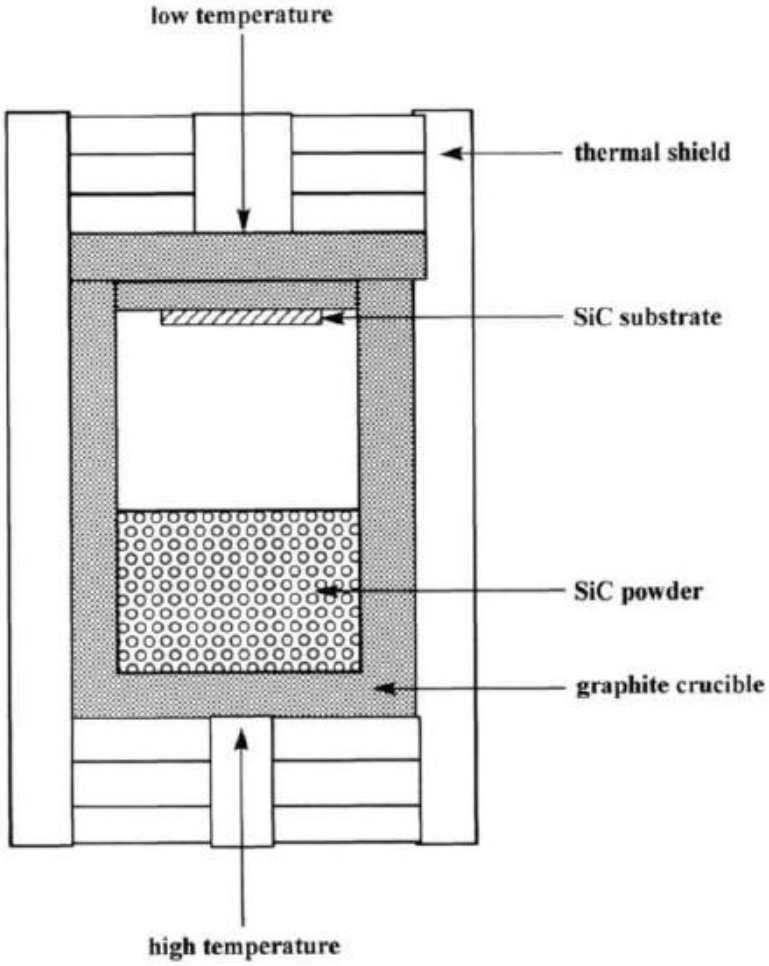

Figure 12: Graphite crucible used for seed growth of SiC (Harris, 1995)

3.5.2 High-temperature chemical vapour deposition

In 1995, a new technique called high-temperature chemical vapour deposition (HTCVD) was presented for the growth of SiC boules. The technique uses

gases instead of a powder as source material. The apparatus consists of three separate zones: an entrance zone, a sublimation zone and a growth (or condensation) zone. The gases used are mainly silane, ethylene and a helium carrier. The carrier flow is very low. A schematic representation of the HTCVD system is shown in Figure 13.

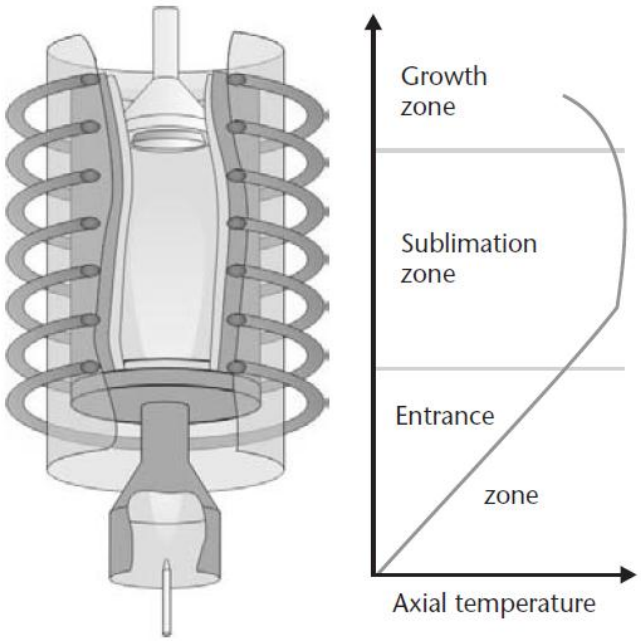

Figure 13: Schematic diagram of HTCVD (Saddow & Agarwal, 2004)

Silane and ethylene are present at very high concentrations, so that homogeneous nucleation dominates the process. As the gases enter into the hot part of the injector, the silane will decompose and form small Si liquid droplets or solid microcrystals, depending on the temperature. The ethylene will also take part in the reaction, forming microparticles of Si_xC_y.

The formed microparticles of Si_xC_y will move into the hot chamber or the sublimation zone with the aid of the inert helium carrier gas. Once in the sublimation zone, the microparticles will sublimate to form Si, Si_2C and SiC_2, as in the case of seeded sublimation growth. A thermal gradient is then applied, so that the sublimated species will condense on the seed (Saddow & Agarwal, 2004).

3.5.3 Epitaxial growth

Epitaxial growth is achieved by modifying the sublimation method. With this method, source and substrate are separated by a small gap of about 1 mm. The growth is carried out close to equilibrium in this arrangement. The substrate is thermally etched before sublimation begins. This makes it possible to grow, at low rates, thin homoepitaxial layers on 6H and 4H with residual impurity concentration. This method is used mainly for device fabrication (Saddow & Agarwal, 2004).

3.6 Physical properties

Silicon carbide is widely used as an abrasive in grinding, cutting and polishing glasses and sharpening stones. It is also used in the manufacture of porcelain, refractory brick, furnace linings and emery paper. The compound is also used in semiconductor technology (Patnaik, 2002).

3.6.1 Density

Experimental measurements place the density of SiC in the range of 3.166 to 3.249 g/cm^3, depending on the polytype. Most of these measurements were obtained using X-ray data and calculating the density using Equation 3.4:

$$\rho = \frac{4MW_{SiC}}{NV} \tag{3.4}$$

where:

- MW_{SiC} is the molecular weight of SiC
- V is the volume of the unit cell (i.e. the cube of the lattice parameter for 3C)
- N is Avogadro's constant
- 4 is the number of formula units in the cell

Table 1 gives density values for different polytypes near room temperature (Harris, 1995).

Table 1: Densities for different crystalline forms of SiC

Density ($g\,cm^{-3}$)	Polytype	Temperature (K)
3.214	2H	293
3.166	3C	300
3.21427	3C	300
3.210	3C	300
3.211	6H	300
3.24878	6H	300

3.6.2 Lattice parameters of SiC

The X-ray diffraction technique is the most commonly used method to determine the lattice parameters for SiC. Table 2 gives the values at near room temperature for different crystalline structures (Harris, 1995).

Table 2: Lattice parameters for SiC

Lattice parameter (a,c in Å)	Polytype	Temperature (K)
a = 4.3596	3C	297
a = 4.3582	3C	0
a = 3.0763	2H	300
c = 5.0480		300
a = 3.0730	4H	300
c = 10.053		
a = 3.0806	6H	297
c = 15.1173		
a = 3.080	6H	0
c = 15.1173		
a = 12.691	15R	300
α = 13°54′		
a = 17.683	21R	300
α = 9°58′		
a = 27.704	33R	300
α = 6°21′		

3.6.3 Thermal conductivity

Silicon carbide is an attractive semiconductor material with highly suitable properties for high-power, high-frequency and high-temperature applications. From the device application point of view, the thermal conductivity of SiC exceeds that of copper, beryllium oxide (BeO), aluminium oxide (Al_2O_3) and aluminium nitride (AlN). The actual value of the thermal conductivity can vary with polytype (Saddow & Agarwal, 2004). Some typical values at room temperature are given in Table 3.

Table 3: Thermal conductivity of SiC at room temperature (Harris, 1995)

Thermal conductivity, χ ($W\,cm^{-1}\,K^{-1}$)	Polytype	Comments
3.2	3C	poly-3C
3.7	4H	-
3.6	6H	$N_N = 8 \times 10^{15}\,cm^{-3}$ at 300 K
3.6	6H	$N_N = 5 \times 10^{16}\,cm^{-3}$ at 300 K
3.6	6H	$N_N = 1 \times 10^{19}\,cm^{-3}$ at 300 K
2.31	6H	$N_{Al} = 5 \times 10^{19}\,cm^{-3}$ at 300 K
4.9	6H	-

The thermal conductivity at very low temperatures (9 to 40 K) is shown in Table 4.

Table 4: Thermal conductivity of SiC between 9 and 40 K (Harris, 1995)

Temperature (K)	χ ($W\,cm^{-1}\,K^{-1}$)		χ ($W\,cm^{-1}\,K^{-1}$)
	6H	4H	3C
9	0.7	0.12	0.23
10	0.85	0.16	0.31
12	1.41	0.27	0.52
15	2.0	0.51	0.71
20	3.6	1.08	1.59
25	5.0	1.70	2.03
30	6.3	2.6	3.4
35	8.0	3.4	4.6
40	10.05	4.3	5.02

The values of thermal conductivity typically follow a trend in the form of Equation 3.5 (Harris, 1995).

$$k_T = AT^{-C} \tag{3.5}$$

where:

- k_T is the thermal conductivity
- A and C are constants

3.6.4 Review

Descriptions of the physical properties of bulk SiC can easily be found in the literature (Harris, 1995; Saddow & Agarwal, 2004; Yaws, 2008; Zinkle & Snead, 1998). The various crystalline forms, however, differ in their physical properties by varying degrees, depending on the specific polytype. These values are scattered in the literature, but are easily obtained in literature reviews (Andrievski, 2009; Bechstedt *et al*., 1997; Izhevskyi *et al*., 2000), and are summarised in Table 5.

Table 5: Physical properties of SiC polytypes (Andrievski, 2009)

Property	Polytype			
	3C (β -SiC)	2H (α -SiC)	4H (α -SiC)	6H (α -SiC)
Hexagonality (%)	0	100	50	33
Stacking order	ABC	AB	ABCB	ABCACB
Lattice constant a (nm)	0.43589 to 0.43596	0.30753 to 0.3081	0.3070 to 0.3081	0.3073 to 0.3081
ρ (g/cm^3)	3.215	3.219	3.215	3.212

3.7 Defects

Two major defects – which have become of great concern to device researchers and create significant problems and debate – are highlighted below.

3.7.1 Micropipes

Three main processes have been shown to lead to the formation of micropipes, the first being the bunching together of numerous screw dislocations to form a single large screw dislocation. At this point, it becomes energetically favourable to create a hollow core in the centre of the structure. The second and third modes of micropipe formation are through vacancy condensation at a helical dislocation and through system contamination, where particles are trapped in the growing crystal (Saddow & Agarwal, 2004).

3.7.2 Stacking faults

When stacking sequences are disturbed, it leads to stacking faults, as shown in Figure 14. These faults could cause the degradation of bipolar devices (traditional power devices because of their capability to provide high currents and blocking voltages) (Saddow & Agarwal, 2004). Ongoing work is being done to reduce defects in SiC material. One of the more interesting concepts is the reduction of defects through epitaxial growth on porous SiC substrates (Saddow & Agarwal, 2004).

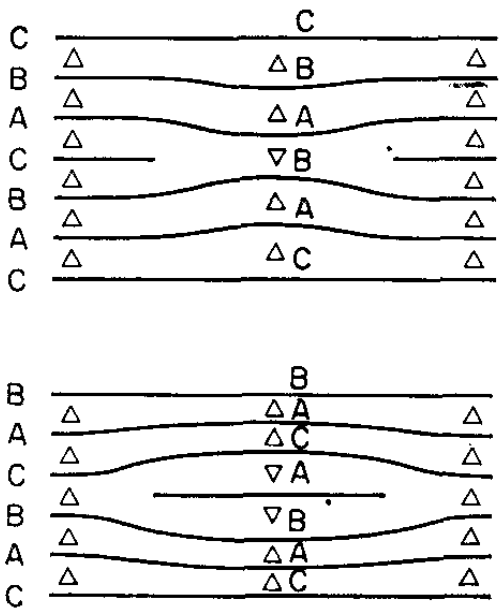

Figure 14: Stacking faults (Hull & Bacon, 2001)

3.8 Silicon carbide nanoparticles

Silicon carbide nanomaterials, such as nanowires, nanorods and nanotubes, have recently received considerable attention, because of their attractive optical, electrical, mechanical and thermal properties. Nano-SiC is also being studied for other applications as a catalyst, sorbent and membrane support. These applications can be attributed to its properties of particle strength, abrasion resistance and high thermal conductivity. Various processes have been developed in order to prepare nano-SiC (Ahmed & El-Sheikh, 2009), which are discussed in the following sections.

3.8.1 Thermal plasma technology

Plasma spraying is part of thermal spraying, a group of processes in which finely divided metallic and non-metallic materials are deposited in a molten or semi-molten state on a prepared substrate. The thermal plasma heat source (DC or RF discharges), with temperatures over 8 000 K at atmospheric pressure, allows for the melting of any material.

Powdered materials are injected in the plasma (RF discharges) or the plasma jet (DC arcs), where particles are formed, accelerated and melted, or partially melted, before they flatten and solidify onto the substrate (forming lamellae or splats) (Fauchais, 2004). Figure 15 represents the basic concepts behind the technology.

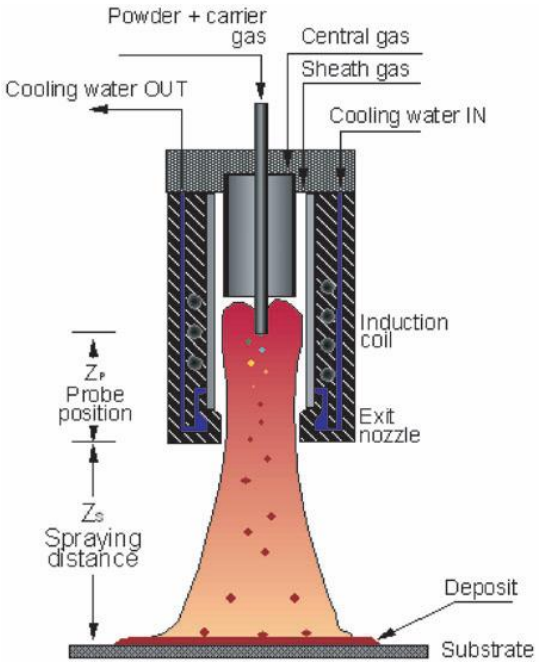

Figure 15: Plasma spray technology (Fauchais, 2004)

A group of researchers at the University of Alabama have shown that, if using SiO_2 and CH_4 as starting materials, SiC can be synthesised by plasma spraying. This results in SiC powders with average sizes of less than 100 nm, along with fibre-like microstructures (Tong & Reddy, 2006). A schematic representation of the thermal plasma reactor is shown in Figure 16.

The SiC is formed through the reaction shown in Equation 3.6:

$$SiO_2 + CH_4 \rightarrow SiC + 2H_2O \qquad (3.6)$$

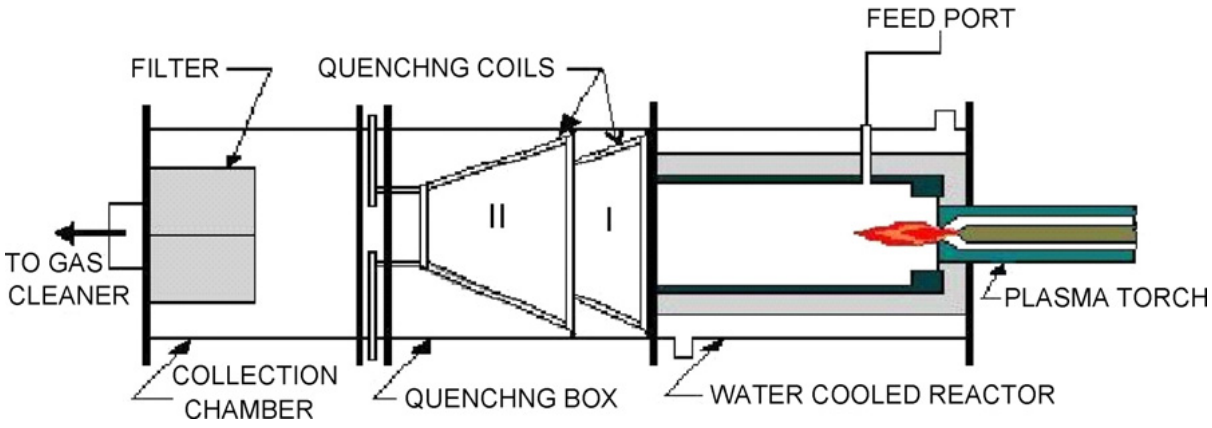

Figure 16: Schematic representation of thermal plasma reactor (Tong & Reddy, 2006)

3.8.1.1 Arc plasma

Ishizaki *et al*. (1989) report a direct method for the production of ultrafine carbide and nitride powders using the arc plasma method and methane for the precursor of the carbides. They produced SiC, titanium carbide (TiC) and tungsten carbide (WC) powders with particle sizes ranging from 20 to 40 nm (Ishizaki *et al.*, 1989). The SiC they produced is shown in Figure 17.

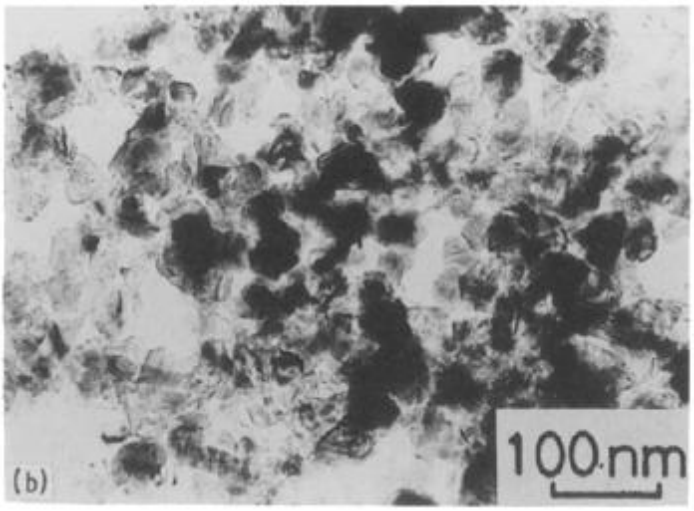

Figure 17: SiC nanopowders produced through the arc plasma method (Ishizaki *et al.*, 1989)

Inoue *et al*. (1989) also produced ultrafine SiC powders using arc plasma irradiation, with methane and silicon as precursors. SiC particles with sizes between 20 and 40 nm were produced (Inoue *et al.*, 1989). Using silica and methane (CH_4), Taylor and Pirzada (1992) produced ultrafine SiC powders using a non-transferred arc thermal plasma reactor. A mathematical model was proposed and they compared the results with theoretical calculations.

3.8.1.2 Inductively coupled plasmas

ICPs have also been shown to be capable of producing SiC nanopowders. Hollabaugh *et al*. (1983) developed an RF plasma system that overcame a common problem concerning the melting of quartz tubes. This system made use of an induction coil and was then used to produce ultrafine and ultrapure SiC powders. Sizes ranged between 10 and 20 nm and the particles are shown in Figure 18.

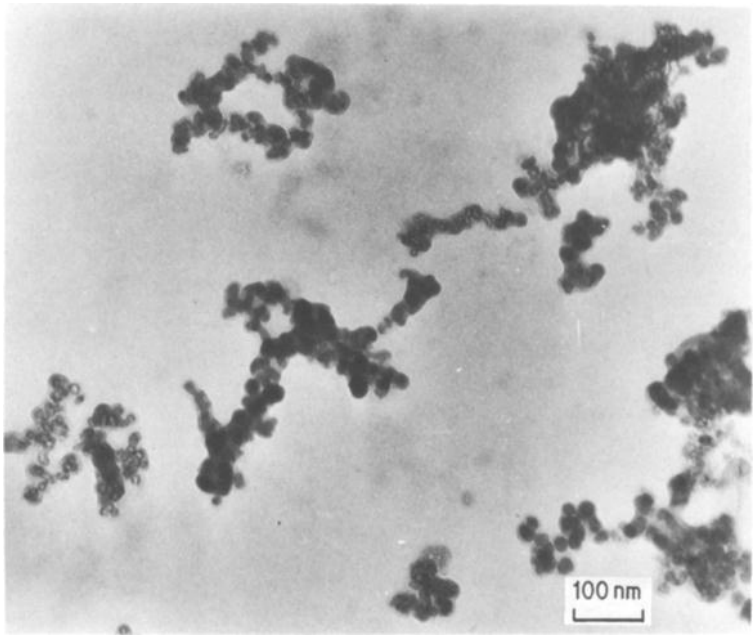

Figure 18: SiC nanoparticles produced through an RF inductively coupled plasma system (Hollabaugh *et al.*, 1983)

Guo *et al*. (1997) published a study on the formation of ultrafine SiC powders through the reaction of elemental silicon and methane in an induction plasma. The resulting powder was composed of a mixture of α- and β-SiC, with sizes ranging from 40 to 60 nm. It was also found that the plasma gas composition had an influence on the proportions of α- and β-SiC (Guo *et al.*, 1997). A transmission electron microscope (TEM) micrograph of their results is shown in Figure 19.

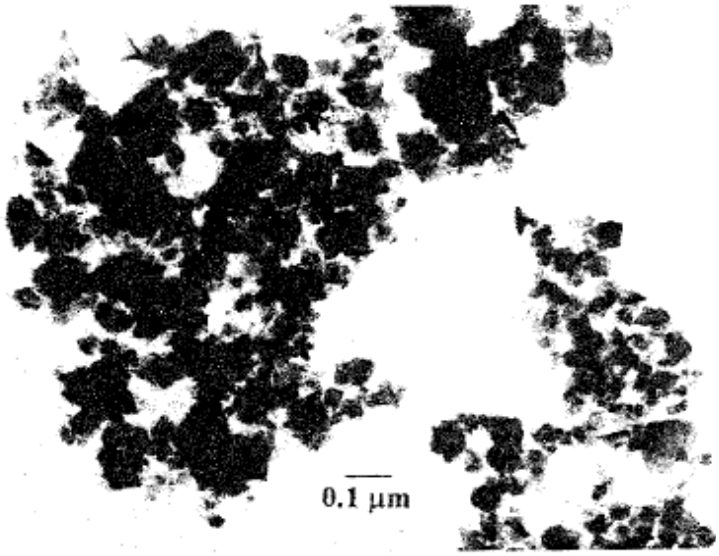

Figure 19: A TEM micrograph of ultrafine SiC produced in an induction plasma (Guo *et al.*, 1997)

Leconte *et al.* (2008) demonstrated how the use of ICPs allows for the production of large amounts of SiC nanopowders from cheap coarse (bulk) SiC powders. In their paper, they addressed the effects of process pressure, the plasma gas composition, and the precursor nature on the SiC structure. They found that, regardless of the precursor structure (α- or β-SiC), the resulting nanoparticles obtained a cubic crystalline form with sizes ranging from 20 to 40 nm (Leconte *et al.*, 2008). Scanning electron microscope (SEM) micrographs of their results are shown in Figure 20.

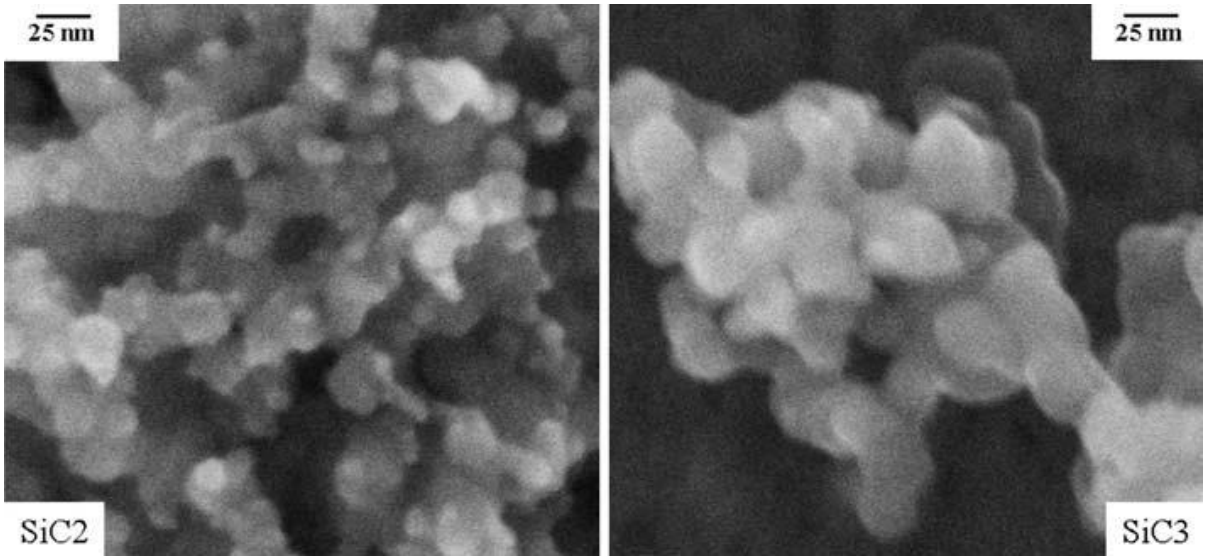

Figure 20: SEM micrographs of SiC nanoparticles produced through ICPs (Leconte *et al.*, 2008)

More recently, Ko *et al.* (2012) used other organic precursors in RF inductively coupled plasmas (tetraethylorthosilicate, hexamethyldisilazane and vinyltrimethoxy silane) to synthesise SiC nanopowders that lie between 30 and 100 nm. Both α- and β-SiC were produced, and the resulting nanopowder is shown in Figure 21.

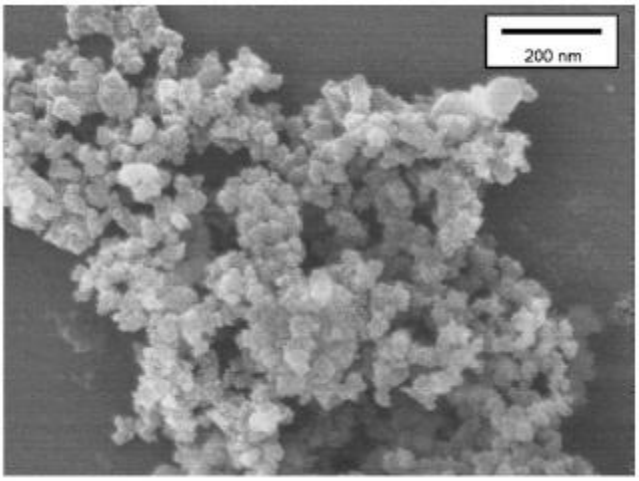

Figure 21: SiC nanopwders produced through RF ICP using organic precursors (Ko *et al.*, 2012)

3.8.1.3 Direct current plasma system

Nano-sized SiC powders have been prepared using direct current plasma systems. Oh *et al*. (2002) produced SiC using a DC plasma torch and silicon tetrachloride ($SiCl_4$) with methane. The resulting powder was dominated by β-SiC, with small amounts of α-SiC and free carbon. The average size of the powder synthesised was estimated to be less than 100 nm and uniform in distribution (Oh *et al.*, 2002). Figure 22 shows TEM photographs of the nanoparticles.

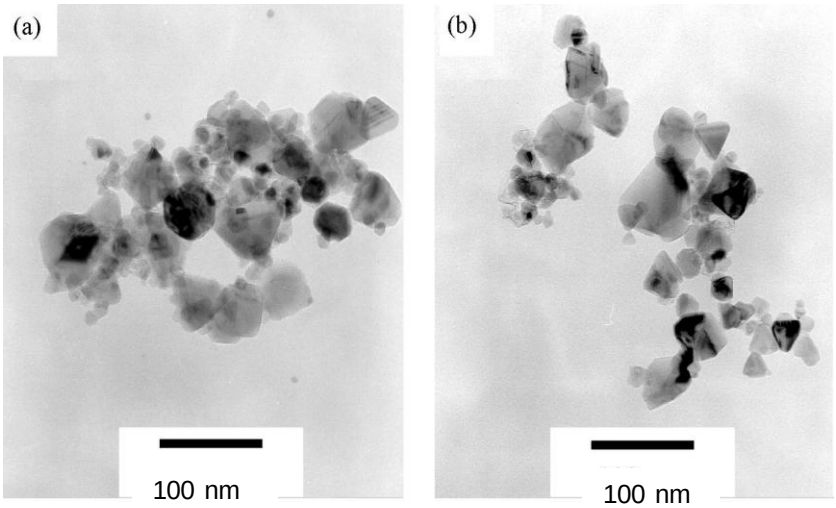

Figure 22: TEM photographs of SiC collected at different positions and produced through a DC plasma system (Oh *et al.*, 2002)

A few years earlier, Zhu *et al*. (1993) published a paper on the synthesis of ultrafine SiC nanopowders using a DC plasma reactor. Using a 15 kW plasma reactor and either $SiCl_4$ or methyltrichlorosilane (CH_3SiCl_3) as precursor, they produced particles with sizes of 15 to 60 nm (Zhu *et al.*, 1993).

3.8.2 Pulsed laser deposition

Pulsed laser deposition (PLD) is a thin film deposition technique where a pulsed laser beam is focused onto a material that is to be deposited. When the laser pulse strikes the target, the material is vaporised (in a plasma plume)

and deposits as a thin film on a substrate. The process occurs inside a vacuum chamber or in the presence of a background gas, such as oxygen, which is commonly used when depositing oxides.

The physical process of PLD is quite complex. When the laser pulse is absorbed by the target, energy is converted towards electron excitation and then into thermal, chemical and mechanical energy, resulting in evaporation and plasma formation. The surrounding vacuum is then filled with the expanding material, which contains many atomic species, including atoms, molecules, electrons, ions and molten globules, before depositing on the substrate (Chrisey & Hubler, 1994). A schematic diagram of the process is shown in Figure 23.

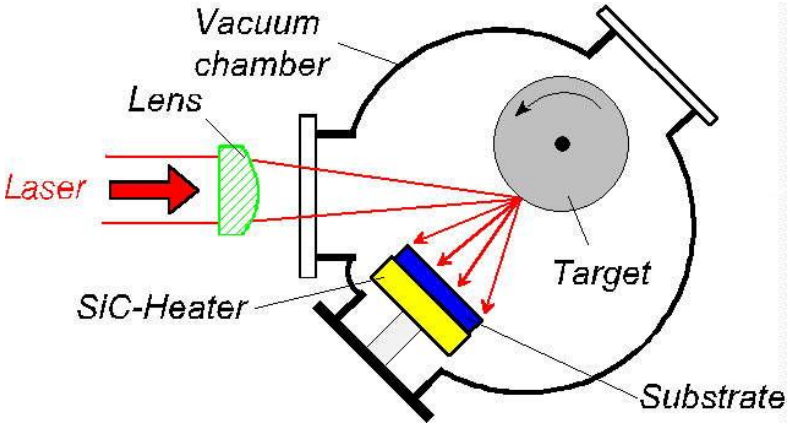

Figure 23: Pulsed laser deposition (Physandtech, 2001)

Antsiferov *et al*. (1998) produced ultrafine β-SiC powders using this process with a CO_2 laser beam and pressed mixtures of powders of silicon and graphite obtained through the mechanical crushing of the initial substances.

Kamlag *et al*. (2001) formed cubic SiC nanocrystals by laser-assisted chemical vapour deposition. A CO_2 laser beam was used, along with silane (SiH_4) and acetylene (C_2H_2) as precursors, and the resulting particle sizes were estimated to be approximately 12 nm (Kamlag *et al.*, 2001). TEM images of the resulting particles are shown in Figure 24.

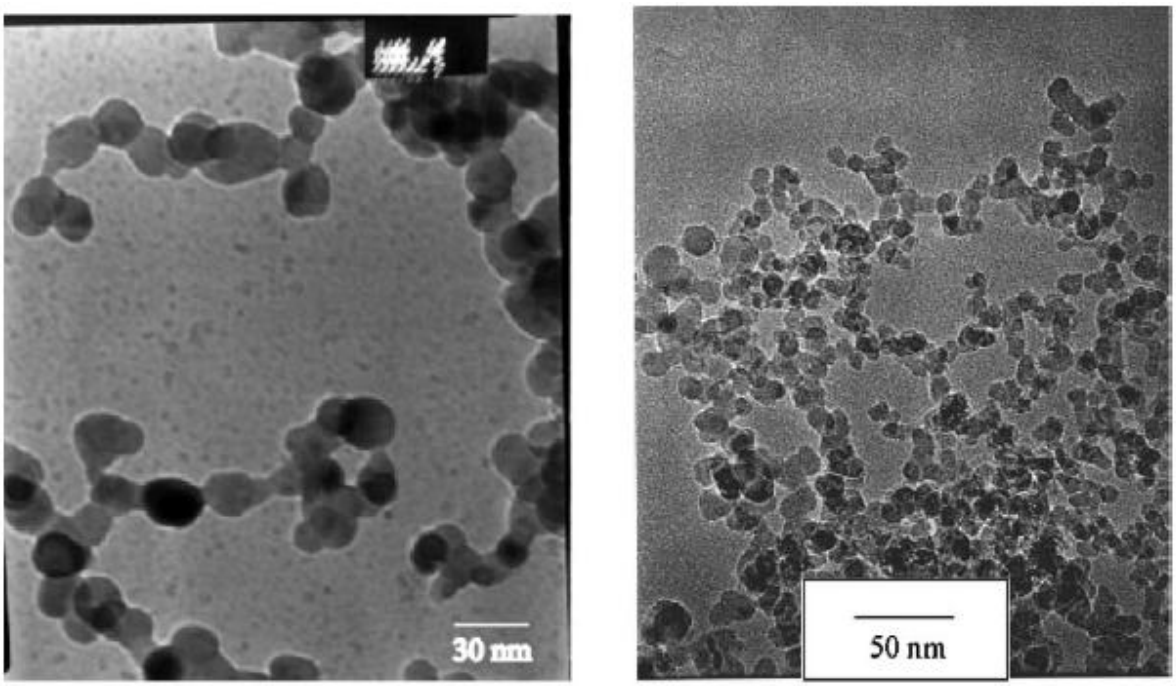

Figure 24: TEM image of SiC nanoparticles produced through PLD (Kamlag *et al.*, 2001)

Zhang *et al*. (2009) also demonstrated, through PLD, the synthesis of various types of nanostructured SiC materials – such as nanoholes, nanosprouts, nanowires and nanoneedles – by controlling the substrate temperature and material (Zhang *et al.*, 2009). SEM images of their results are shown in Figure 25.

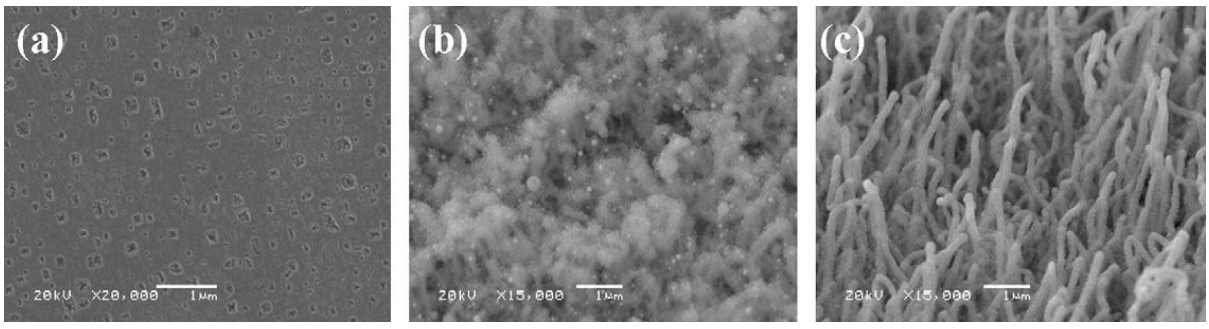

Figure 25: SEM images of nanostructured SiC materials through PLD (Zhang *et al.*, 2009)

3.8.3 Chemical vapour deposition

Amorphous fine silicon carbide powders have been prepared by Kavecky *et al*. (2000) by using chemical vapour deposition (CVD). The reaction mixture consisted of SiH_4 and C_2H_2 in a vertical tubular flow reactor operating between 900 and 1 250 °C. Ultrafine SiC powders were produced, with sizes ranging from 0.1 to 0.2 µm and agglomerate sizes below 0.3 µm (Kavecky *et al.*, 2000). Micrographs of the resulting powders are shown in Figure 26.

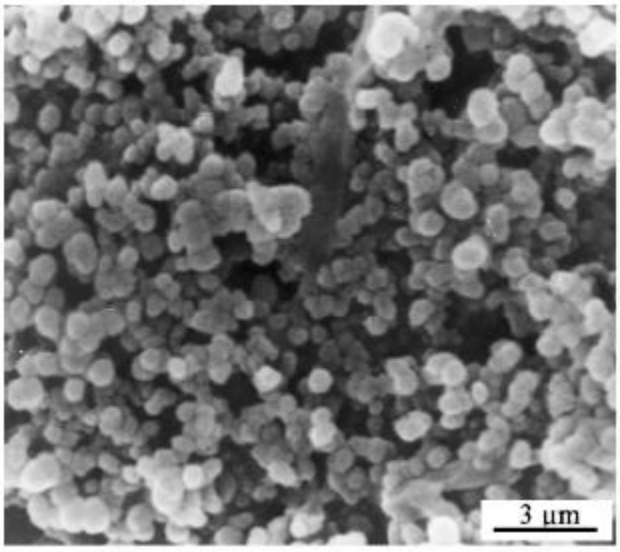

Figure 26: Micrograph of SiC obtained through CVD (Kavecky *et al.*, 2000)

SiC nanopowders were prepared by CVD at 850 °C and 900 °C from liquid carbosilanes by Li *et al*. (2007). Particle sizes ranged between 50 and 70 nm and are shown in Figure 27.

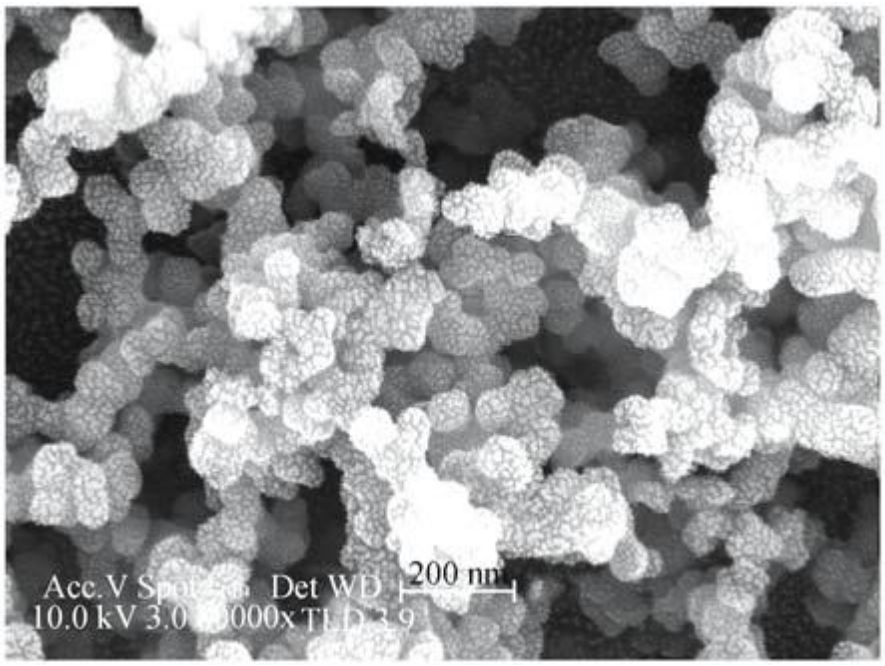

Figure 27: SEM micrograph of SiC nanoparticles through CVD of liquid carbosilanes (Li *et al.*, 2007)

3.8.4 Microwave synthesis

Fine, monophasic SiC can be produced through the direct solid-state reaction of its constituents (Si and C) in a microwave field. Satapathy *et al.* (2005) used a 2.45 GHz microwave field to determine the optimum parameters for the SiC phase formation. They showed that the formation of phase-pure SiC can be achieved at 1 300 °C in less than five minutes, resulting in sub-micron-sized particles, as shown in Figure 28 (Satapathy *et al.*, 2005).

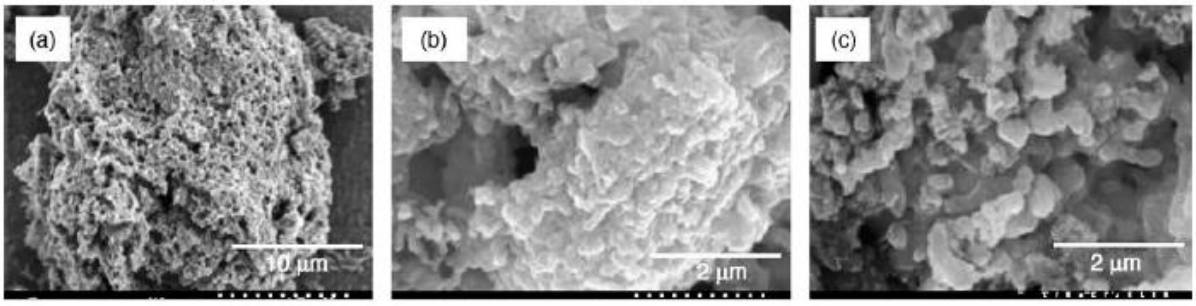

Figure 28: Scanning electron micrographs of β-SiC powders synthesised using microwave fields (Satapathy *et al.*, 2005)

Moshtaghioun *et al.* (2012) reported an improved procedure for the synthesis of SiC nanopowders using silica as precursor. The process involves carbothermic reduction under fast microwave-induced heating in a 2.45 GHz field in a nitrogen atmosphere. β-SiC was produced at 1 200 °C after five minutes of microwave exposure, resulting in particle sizes ranging from 10 to 40 nm (Moshtaghioun *et al.*, 2012). TEM micrographs of the particles are shown in Figure 29.

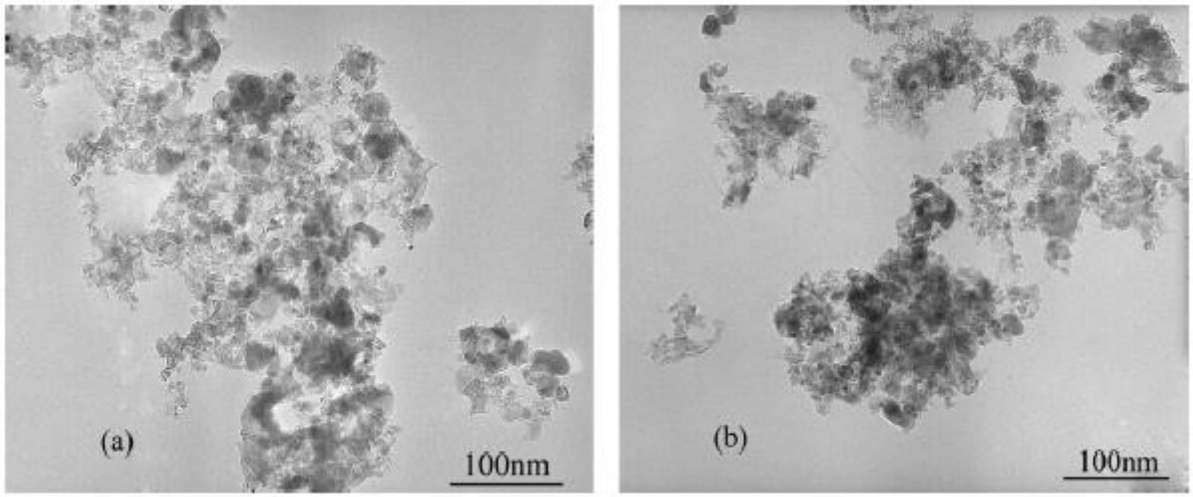

Figure 29: TEM micrographs of SiC particles produced in a microwave field (Moshtaghioun *et al.*, 2012)

3.9 Summary

In this chapter, the history, formation and properties of SiC have been discussed and a brief explanation of the nomenclature was given with regard to the numerous crystalline forms. Various synthesis methods are currently being investigated and show promising results in terms of particle sizes and rate of formation.

CHAPTER 4

Production of SiC nanoparticles through microwave plasmas

4.1 Introduction

This chapter further focuses the discussion towards the synthesis and characteristics of SiC nanoparticles, specifically through the use of microwave plasmas. In sections 4.2 and 4.3, the various stages and processes of particle formation in microwave-induced plasmas will be briefly described. The parameters that influence the particle sizes are discussed in section 4.4, followed by an overview of the phenomenon known as filament formation, common in atmospheric pressure plasmas, in section 4.5. The chapter is concluded in section 4.6 with a summary of the current literature on the formation of SiC in microwave plasmas operating at atmospheric pressure.

4.2 Microwave plasma synthesis of nanoparticles

The use of microwaves in the synthesis of nanoparticles is not an entirely new concept and has given rise to a multidisciplinary field of research and development, interconnecting different fields, such as physics, chemistry and nanotechnology. Varying applications and synthesis methods demand further knowledge on topics such as chemical engineering, thermodynamics and materials science (Szabo, 2013: 271).

The synthesis of nanoparticles using microwave technology is divided into two main groups: wet-chemical methods, where a liquid is heated using microwave radiation that induces subsequent decompositions, and a combination of gas-phase synthesis methods with microwave and plasma technology. In this chapter, the application and fundamentals of the latter in the synthesis of nanoparticles will be broadly discussed, followed by a more focused study of the application of this technology for the specific use of SiC nanoparticle synthesis.

4.3 Particle formation in microwave plasmas

The nanoparticle formation mechanism occurs in the following five steps in what is known as the reaction zone (Szabo, 2013: 277):

1) As the gaseous components enter the plasma, they are ionised and dissociated.
2) The dissociated components undergo chemical reactions and form molecules. Their electric charges enable them to accelerate through the electric field of the microwaves.
3) Homogeneous nucleation, through the collisions of molecules, form clusters.
4) Further collisions between clusters and molecules or other clusters promote their growth.
5) Due to the electric charge of the particles, further growth by coagulation is reduced.

Each step only lasts a few milliseconds and after Step 5, the particles exit the reaction zone and lose their electric charge. It is important to note that the charging of the particles is the most important growth mechanism, because it governs the interactions between the particles and the plasma (Gatti & Kortshagen, 2008). However, the charging of particles increases the complexity of the growth process when compared to that of conventional gas-phase synthesis.

Nucleation is the critical step for particle formation. Particle size is correlated with the number concentration of nuclei in the plasma, as explained by Szabo (2013: 278): “For a given amount of precursor a high number concentration of nuclei leads to small particle sizes, whereas a small number concentration of nuclei results in larger particles.”

4.4 Parameters influencing particle size

4.4.1 Precursor concentration

It is preferred that a vaporised precursor be used as starting material, mainly because the microwave plasma is a gas-phase process. Other than silane (SiH_4), few precursors are found in the gas phase. This implies that most precursors have to be evaporated outside the system before entering the reaction zone.

Changing the precursor concentration implies changing the collision frequencies between species in the plasma. In turn, it is to be expected that this parameter exerts a strong influence on number concentration, nuclei formation and therefore particle size (Szabo, 2013: 287). Previous work by other research groups shows a tendency for increased particle size with increased precursor concentration (Giesen *et al*., 2005; Janzen *et al*., 2001; Shimada *et al*., 2010).

It seems that this positive dependence of particle size on precursor concentration can be assumed to be a general rule, regardless of the final product or operating pressures.

4.4.2 Temperature and pressure

The temperature in the system can be influenced by the microwave power and the system pressure. The system pressure, in turn, can be influenced by varying the gas flow rate. According to the literature (Janzen *et al.,* 2001*;* Knipping *et al*., 2004; Shimada *et al.*, 2010), it was found that a strong link exists between microwave power (temperature) and particle size*. When the microwave power is increased, the particle size decreases.* The published results indicate that when the power was doubled, the volumes decreased by

a factor of between one and two, depending on the synthesised particles. This result is supported by the theoretical calculations done by Vennekamp *et al.* (2011). At lower power, the reactivity of the plasma results in a smaller number of nuclei. Molecules formed by the chemical reaction condense in the few nuclei, resulting in larger particles. Likewise, at higher power, more nuclei are formed, and thus smaller particle sizes are obtained (Szabo, 2013: 290–291).

When the gas flow rate is increased, the system pressure increases, as mentioned before. This also decreases the precursor concentration, resulting in additional effects influencing the particle size. This can be accounted for by also increasing the feed rate of the precursor such that its concentration remains constant. Experimental data from the literature (Fu *et al.*, 2003; Knipping *et al.*, 2004) shows *a linear increase in particle diameters with increasing pressure* for the synthesis of Si and Al_2O_3 nanoparticles. This behaviour is explained by the increased collision probability, resulting in enhanced particle growth.

4.4.3 Residence time

The residence time, t, is calculated by using an equation of states and is given by Equation 4.1.

$$t_r = \frac{1}{4}\pi d^2 L \frac{p_2}{p_1}\frac{T_1}{T_2}\frac{1}{Q_1} \tag{4.1}$$

where:

- T_2 and p_2 are the system temperature and pressure
- Q_1 is the gas flow rate
- T_1 and p_1 are the temperature and pressure at standard conditions

Table 6 provides a summary of different calculated residence times at different experimental conditions using Equation 4.1, as given by Szabo (2013: 288–289).

Table 6: Calculated residence times at different conditions (Szabo, 2013: 289)

Gas flow rate	5 L/min	7 L/min	9 L/min
Pressure	10 mbar	14 mbar	17 mbar
Microwave power (W)	Residence time, t_r		
200	2.55 ms	2.40 ms	2.36 ms
300	2.37 ms	2.24 ms	2.10 ms
500	2.14 ms	2.06 ms	1.98 ms

These results illustrate that an increase in pressure yields a decrease in particle size. This does not, however, agree with the experimental results, as discussed earlier. It is therefore an indication that the residence time is not a dominating factor in particle growth and a strong influence is not expected.

4.5 Filament formation

Argon microwave plasmas operating at high pressures (atmospheric pressure) are known to exhibit plasma filaments, as shown in Figure 30. These filaments are restricted to the discharge tube's surface and result in a less efficient coverage of the radial cross-section (Hong *et al*., 2008). Research shows that the filamentation process involves either an increase in the electron density or a decrease in the effective frequency for momentum-transfer collisions, i.e. a lower electron temperature (Cardoso *et al*., 2009). The same group showed that a strong variation in the electron temperature is required for a small change in the relative positions occupied by two filaments in the microwave cavity.

Figure 30: Filaments forming during microwave plasma operation

These filaments can be suppressed by introducing a small amount of molecular gas (e.g. N_2, O_2, CO_2 or CH_4) with the argon (Hong *et al.*, 2008).

4.6 Synthesis of SiC

The use of plasma synthesis methods for the production of nanopowders has already been proven numerous times in the past (Ishizaki *et al.,* 1989*;* Rao *et al*., 1995; Taylor & Pirzada, 1992; Young & Pfender, 1985). Currently, however, there is a lack of a commercial process for the production of such nanopowders. For the production of SiC, the Acheson process is used, which incorporates the carbothermic reduction of silicon dioxide (SiO_2). This process, however, has its shortcomings. Many different options for the production of SiC are being investigated, as indicated in the previous chapters. The use of plasmas have been widely covered (Károly *et al.*, 2011; Tong & Reddy, 2006; Zhu *et al.*, 1993), but little research has been done on microwave plasmas.

Amorphous SiC was prepared by Lin *et al.* (2008), using a microwave plasma reactor and tetramethylsilane (TMS) as precursor. The reactor operated at low precursor partial pressure (0.001–0.02 Torr) and used argon as the carrier gas (3 Torr). SiC nanoparticles with sizes between 4 and 6 nm were obtained, shown in Figure 31.

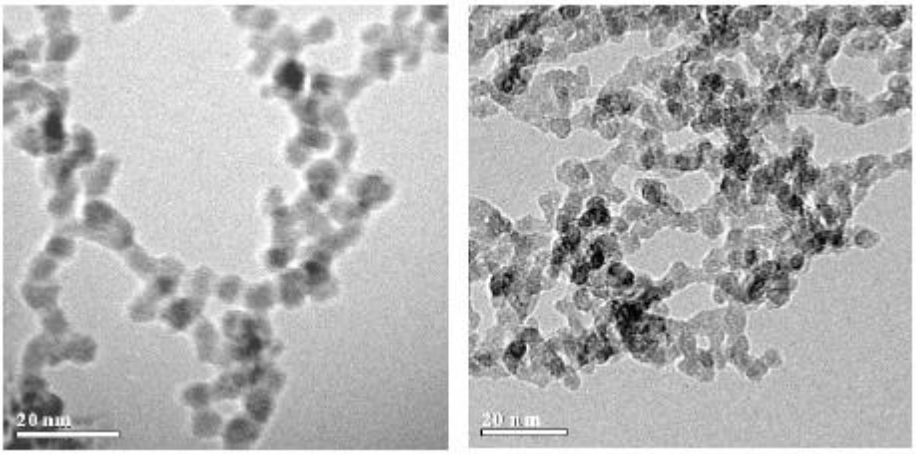

Figure 31: TEM images of SiC nanoparticles obtained by Lin *et al.* (2008)

Similar work was done by Vennekamp *et al.* (2011). They describe the formation of SiC nanopowder using an atmospheric argon microwave plasma with TMS as precursor. Particles with sizes ranging between 7 and 20 nm were produced, shown in Figure 32. They also produced growth rate equations using the theory of Ostwald ripening, showing the dependency of particle growth rate on temperature and pressure.

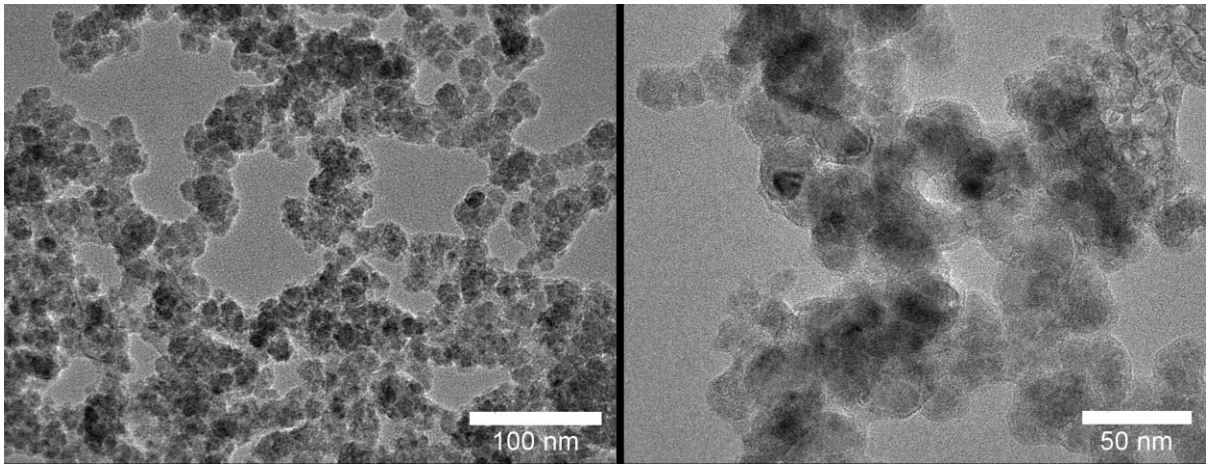

Figure 32: TEM images of SiC nanoparticles by Vennekamp *et al.* (2011)

The particle growth rate was determined to be given by Equation 4.2.

$$\frac{dr}{dt} = \frac{k_{sr} D v_m}{k_{sr} r + D} \frac{p_{SiC} - p_v}{RT} \tag{4.2}$$

where:

- k_{sr} is the rate of the surface reaction with the nanoparticle
- D is the diffusion coefficient in the gaseous plasma
- p_v is given by the Gibbs-Thompson Law
- p_{SiC} can be approximated by the precursor concentration (Vennekamp *et al.*, 2011)

Their results are shown in Figure 33. These results agree with those discussed earlier in this chapter, stating that an increase in system pressure results in an increase in particle growth rate (i.e. particle size), and that an increase in temperature results in a decrease in particle size.

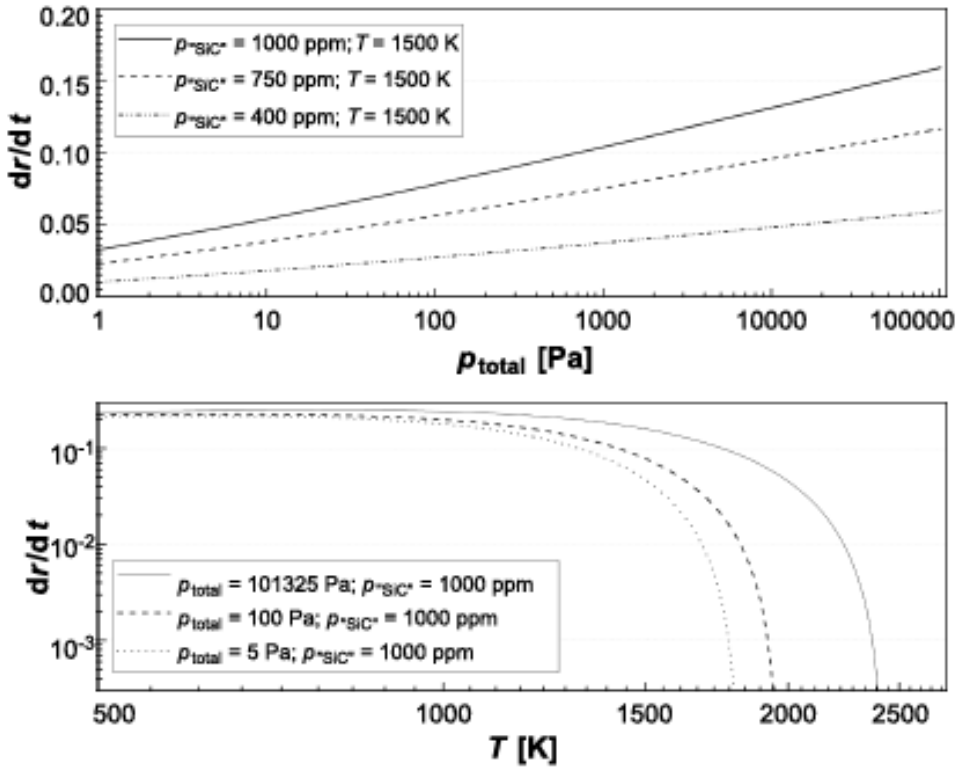

Figure 33: Visualisation of the growth rate equation determined by Vennekamp *et al.* (2011)

4.7 Summary

The literature on the synthesis of SiC in a microwave-induced plasma was summarised and the process of particle growth and the parameters that influence particle size were discussed. It was determined that an increase in system pressure results in an increase in particle size, whereas the opposite is true for temperature. It was also found that there is a scarcity in the literature regarding the synthesis of SiC nanoparticles using microwave plasmas operating at atmospheric pressure.

CHAPTER 5
Experimental setup and equipment

5.1 Introduction

In this chapter, the experimental methodology and equipment will be presented and described, as well as the methods used for the characterisation of the SiC particles. The experimental setup is divided into three sections: calibration (5.2), microwave plasma experiment (5.3) and analysis (5.4).

In the calibration section, a brief overview will be given of the necessary calibrations that were done in order to ensure an accurate mass and energy balance (enthalpies) of the methyltrichlorosilane (MTS). The section on the microwave plasma experiment will cover all work done regarding the microwave plasma. The process parameters studied were the H_2:MTS molar ratio and the total enthalpy (amount of heat content used or released in the system at constant pressure). Finally, in the analysis section, all equipment used for characterisation and analysis will be discussed.

5.2 Calibration

In order to ensure accurate measurements and results, it is necessary to obtain exact mass and energy balances. The least precise measurement for this experiment was the mass flow of MTS into the plasma environment. This problem was addressed by bubbling argon gas for fixed time intervals through the liquid MTS at different flow rates and temperatures, and calculating the MTS mass difference. From this, a mass flow rate could be determined. Some physical properties of MTS are given in Table 7 (Yaws, 2008).

Table 7: Physical properties of MTS

Property	Value	Units
Molecular weight	149.48	g/m
Boiling point	65 °C	°C
Melting point	-90 °C	°C
Specific gravity	1.270 @ 25 °C	
Vapour density	5.17 (Air = 1)	
Vapour pressure	167 @ 25°C	mm Hg

The first calibration took place at room temperature. A flask was filled with approximately 170 mL of liquid MTS. Argon was bubbled through at different flow rates, each time for exactly 10 minutes. The flask was weighed before and after each run. The different calibration runs and results are shown in Table 8.

Table 8: MTS calibration runs (unheated)

Run no.	Q_{Ar} (sccm)	$m_{initial}$ (g)	m_{final} (g)	Δm (g)	t (min)	$\dot{m}$ (g/min)
1	20	468	468	0	10	0
2	50	468	467	1	10	0.1
3	100	467	464	3	10	0.3
4	75	464	462	2	10	0.2
5	125	462	458	4	10	0.4
6	150	458	453	5	10	0.5
7	35	453	452	1	10	0.1

From these results, a calibration curve can be produced, shown in Figure 34.

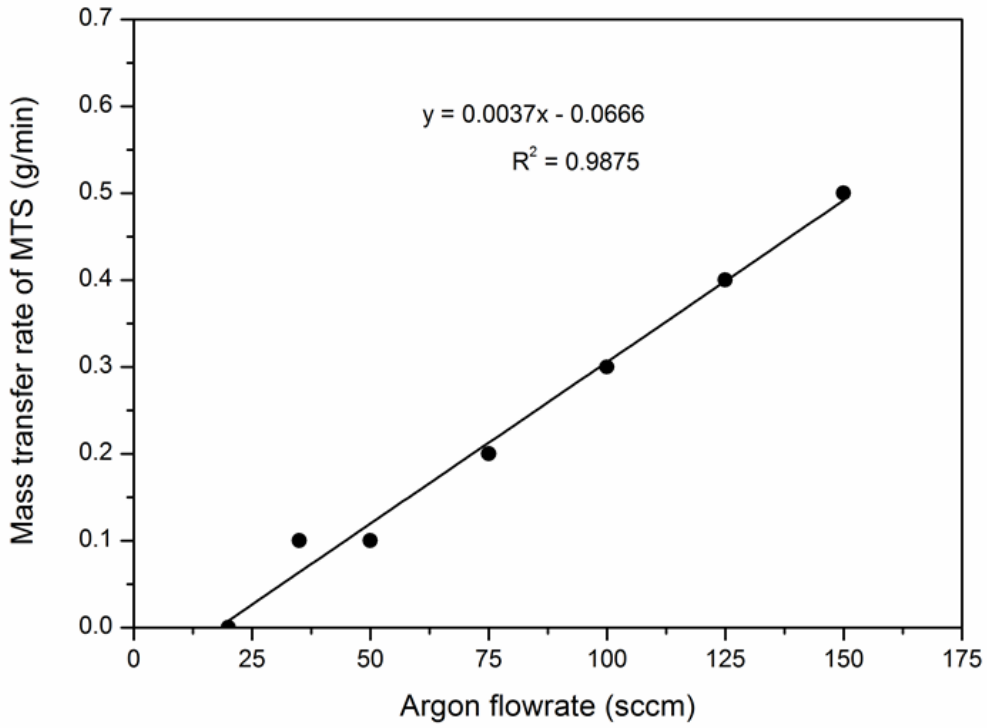

Figure 34: MTS calibration curve at room temperature

Fitting a trend line to the data points results in a straight line equation:

$$y = 0.0037x - 0.0666 \quad (5.1)$$

Using this equation, the mass transfer rate of MTS can be determined if the argon flow rate is known.

In the next procedure, the MTS in the flask was heated to approximately 40 °C, using a self-regulating trace heating cable (40 W/m). The runs were then repeated as before, and the results are shown in Table 9.

Table 9: MTS calibration runs (heated)

Run no.	Q_{Ar} (sccm)	m_{intial} (g)	m_{final} (g)	Δm (g)	Time (min)	$\dot{m}$ (g/min)
1	20	452	452	0	10	0
2	35	452	451	1	10	0.1
3	50	451	449	2	10	0.2
4	75	449	446	3	10	0.3
5	100	446	442	4	10	0.4
6	125	442	436	6	10	0.6
7	150	436	430	6	10	0.6

Plotting the results and fitting a trend line yields the calibration curve shown in Figure 35.

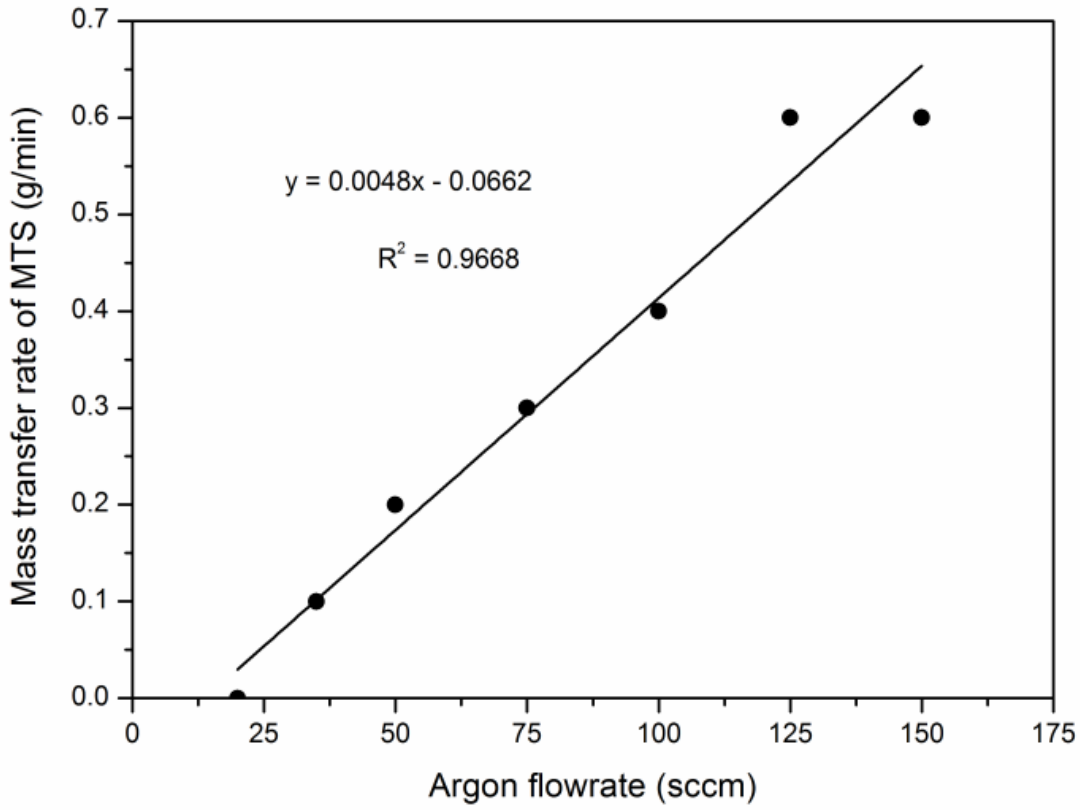

Figure 35: MTS calibration curve (heated)

Fitting a trend line to the data points results in a straight line equation:

$$y = 0.0048x - 0.0662 \quad (5.2)$$

Using this equation, the mass transfer rate of the MTS at 40 °C can be determined if the argon flow rate is known.

When this procedure was repeated with the argon being replaced with hydrogen, a similar calibration curve was obtained at room temperature. The results are shown in Table 10.

Table 10: MTS calibration using hydrogen

Run no.	Q_{H_2} (sccm)	$m_{Initial}$ (g)	m_{final} (g)	Δm (g)	Time (min)	$\dot{m}$ (g/min)
4	100	235.7	234.1	1.6	10	0.16
5	50	234.1	233.4	0.7	10	0.07
6	80	233.4	232.3	1.1	10	0.11
8	20	233	232.5	0.5	10	0.05
9	10	232.5	232.2	0.3	10	0.03
10	150	232.2	229.8	2.4	10	0.24

Plotting the data points, the calibration curve is obtained and shown in Figure 36.

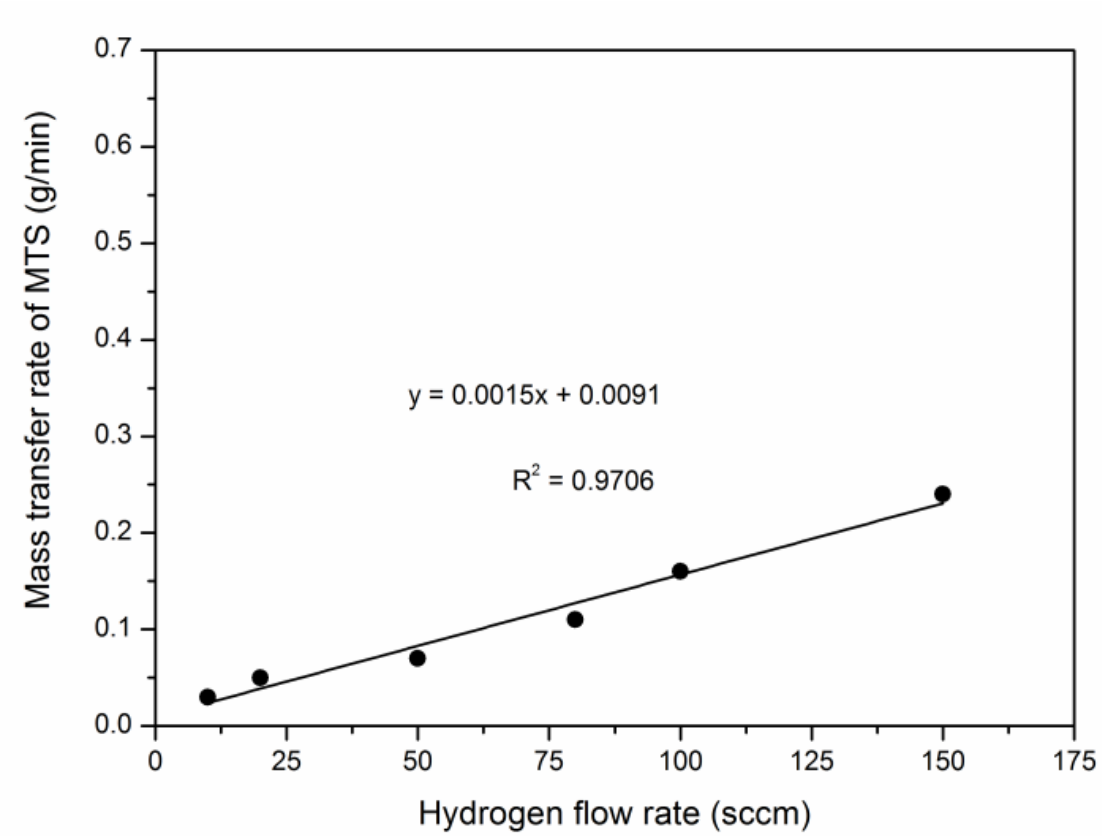

Figure 36: MTS calibration curve using hydrogen

5.3 Microwave plasma experiment

5.3.1 Equipment/apparatus

A commercial microwave source from Electronic GmbH & Co., Germany, model PGEN2450/1.5-1.5KW2AIW, was used. More information is given in Table 11.

Table 11: Microwave source information

Property	Value
Voltage	3x400V / N / PE
Frequency	50 Hz
Current	< 6A

The equipment consists of a 1 500 W power supply with a MOS-FET amplifier, microwave generator operating at 2.45 GHz, a water-cooled magnetron head, a stub tuner, a waveguide and a sliding short, as shown in Figure 37.

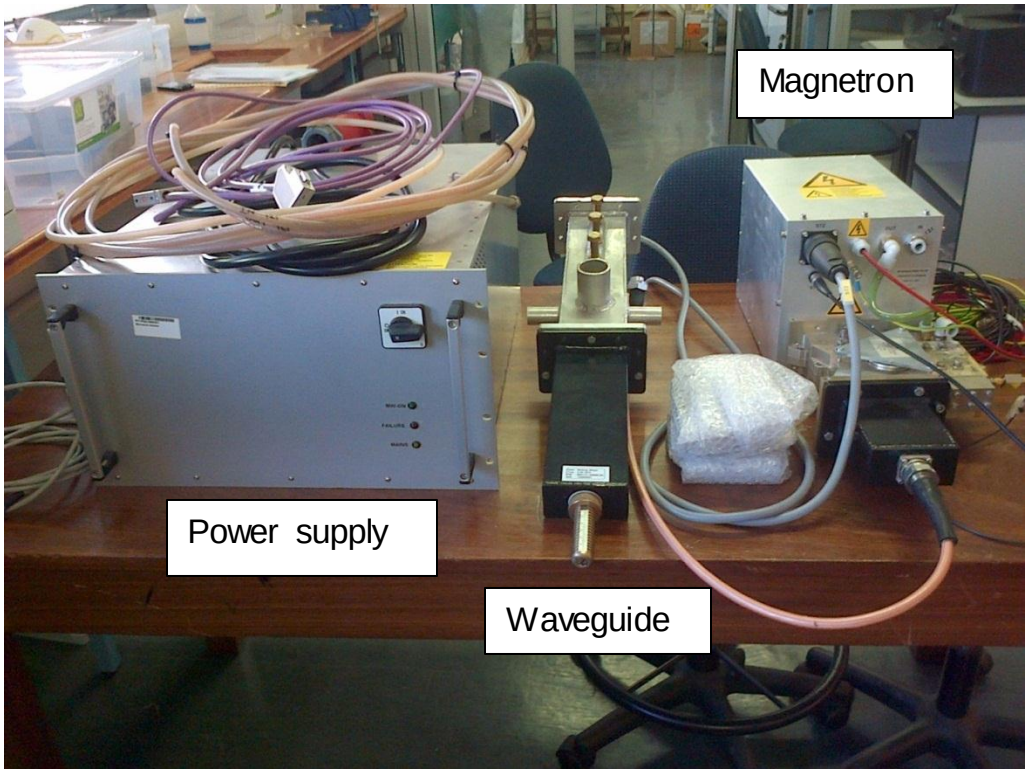

Figure 37: Microwave equipment

The plasma is generated and maintained in quartz tubes. The tubes are positioned through the middle of, and perpendicular to the waveguide after the stub tuner, shown in Figure 38 and Figure 39. The quartz tube has an internal diameter of 2 cm and a length of 30 cm. In- and outlets at the top and bottom of the quartz tube allow for the flow of gas through the plasma.

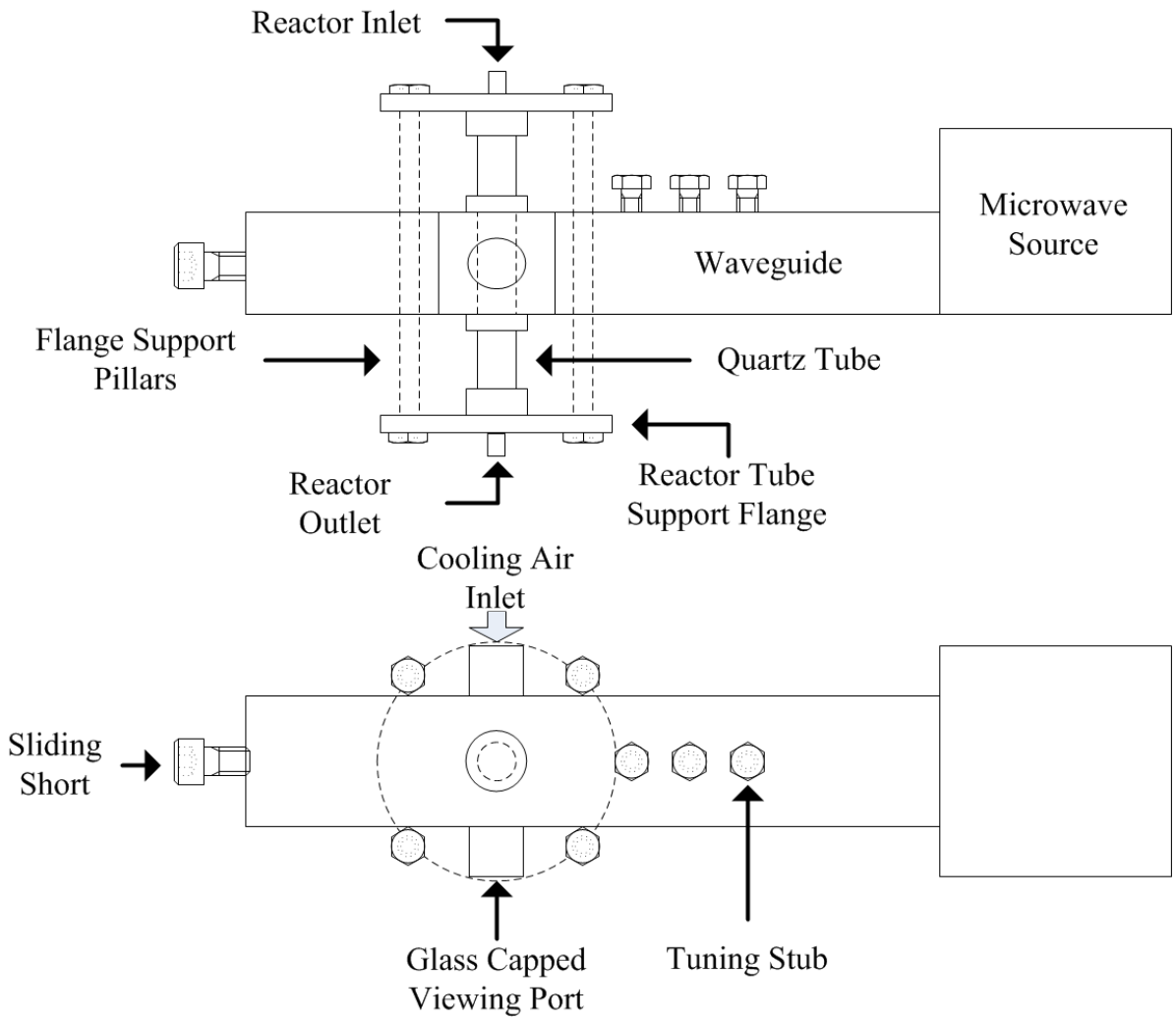

Figure 38: Physical design of the microwave plasma setup

Argon and hydrogen flow rates were controlled using calibrated Aalborg rotameters. The argon plasma was initiated under vacuum ($2x10^{-3}$ mbar), using an Alcatel 2010I duel stage rotary vane pump. A sodium hydroxide (NaOH) scrubber was used to scrub hydrogen chloride (HCl) from the exhaust gas stream. All connections were secured using Swagelok® fittings. Air cooling was implemented through the use of a leaf blower, allowing up to 3 m^3/min air to flow across the outer surface of the quartz tube.

Figure 39: Position of quartz tube

5.3.2 Design of experiment

The experimental design is shown in Table 12. Values were selected to cover as wide an experimental parameter range as possible within the capability of the system.

Table 12: Design of experiment (DoE)

Exp. number	Q_{Ar} (sccm)	$\dot{m}_{MTS}$ (g/min)	H_2:MTS ratio (mol:mol)	P_{MW}(W)
1	150	0.044	4.0	400
2	150	0.044	7.4	570
3	150	0.026	9.3	560
4	150	0.044	7.4	1300
5	150	0.044	4.0	1500
6	150	0.044	1.3	1300
7	150	0.044	0.0	870
8	150	0.044	1.3	570
9	150	0.044	4.0	950
10	150	0.044	4.0	950
11	150	0.044	4.0	950
12	150	0.044	4.0	1500

The resulting central composite design of the experiment is shown in Figure 40.

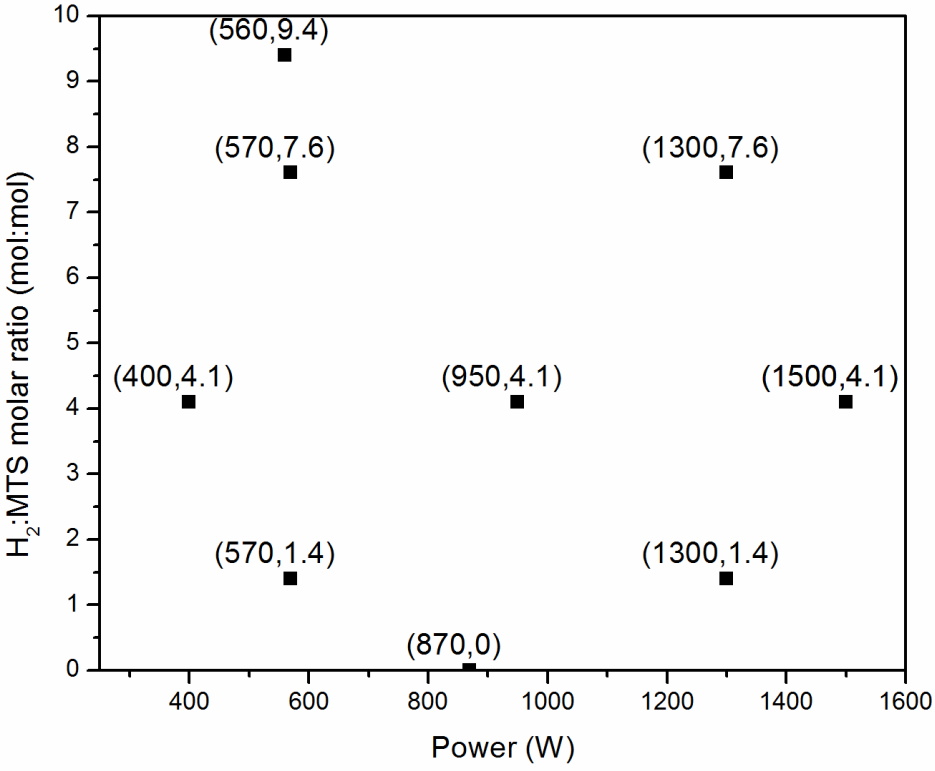

Figure 40: Power and H_2:MTS ratios of DoE

5.3.3 Method/procedure

A schematic diagram of the experimental setup is shown in Figure 41.

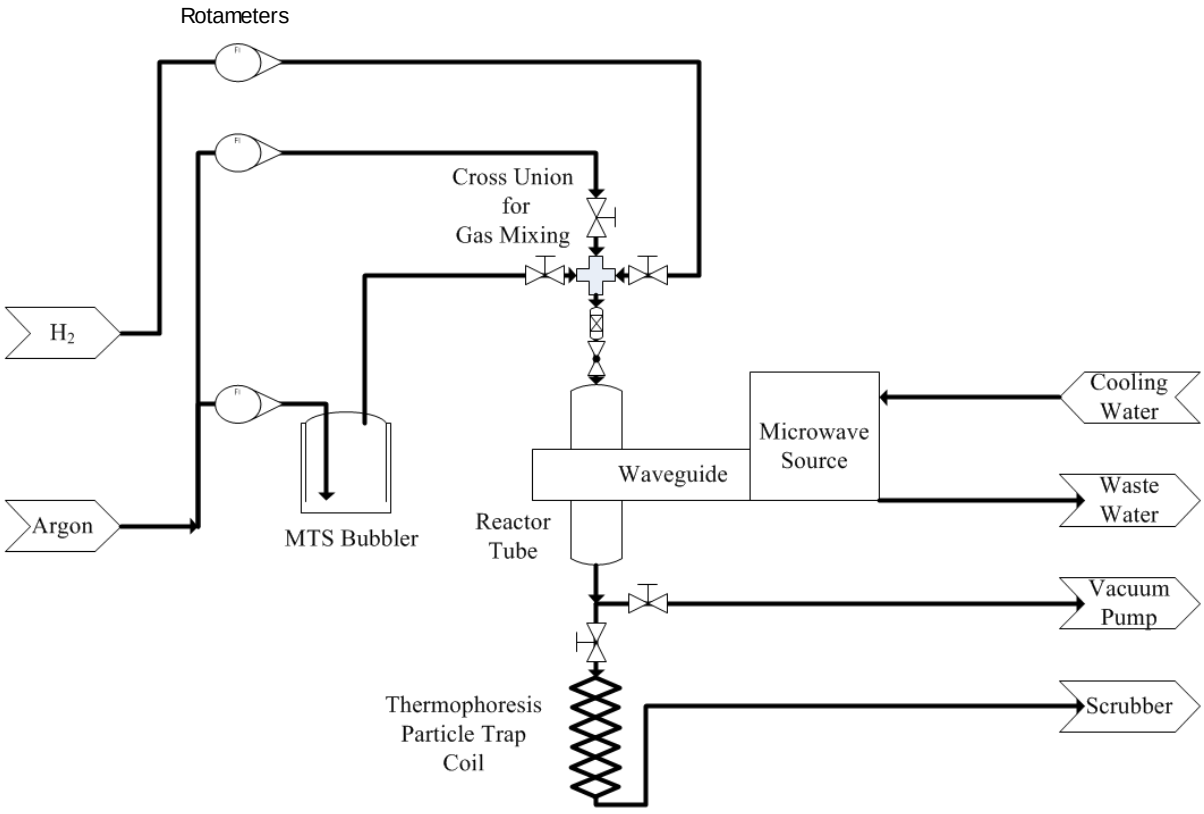

Figure 41: Schematic diagram of complete experimental setup

For each experiment, the following procedure was used in order to initiate the plasma:

Argon gas was flooded through the system at 150 standard cubic centimetres per minute (sccm), during which the vacuum pump was started in order to maintain a vacuum in the quartz tube. The magnetron was started at the desired power and a stable argon plasma was obtained, shown in Figure 42. At this point, the vacuum pump was switched off and the system was allowed to gradually reach atmospheric pressure by flowing through the NaOH scrubber and into the atmosphere. Once a stable atmospheric pressure plasma was obtained, hydrogen was allowed to flow through the system in

order to obtain the desired H_2:MTS molar ratio. The plasma was then observed for up to three minutes, after which the magnetron was switched off and the rotameters were closed.

Figure 42: Argon plasma under vacuum

Depending on the hydrogen ratio, stable plasmas could be maintained at power inputs between 200 and 1 500 W. High hydrogen concentrations were observed to starve and extinguish the plasma. High MTS content resulted in a “dusty” plasma (Shukla & Mamun, 2002). The exit gas from the reactor was passed through a coiled 1/4" copper thermophoresis tube, cooled by immersing the tube in an ice bath to collect any exiting product particles, then passing the exit gas through a NaOH scrubber to remove HCl before releasing the stream into an extraction system.

Nanoparticles agglomerated and accumulated on the inner walls of the copper coil and the quartz tube and were collected after runs by removing the coil and quartz tube and flushing it with distilled water. The water was then evaporated in a drying oven at 50 °C and the SiC nanoparticles were collected.

5.4 Analysis

Particle analyses were performed using available resources. Particle size distribution was determined by placing the SiC samples in a sonification bath for five minutes, after which the samples were placed in a ZEN 3600 Malvern Zetasizer Nano System, shown in Figure 43.

Figure 43: Sonification bath (left) and Zetasizer (right)

SEM was performed on the particles with a high-resolution (6 Å) JEOL 6000 SEM system, and TEM was performed using the Phillips 301 TEM system. Emission spectrographs were taken with an Ocean Optics HR 4000 high-resolution spectrometer, shown in Figure 44.

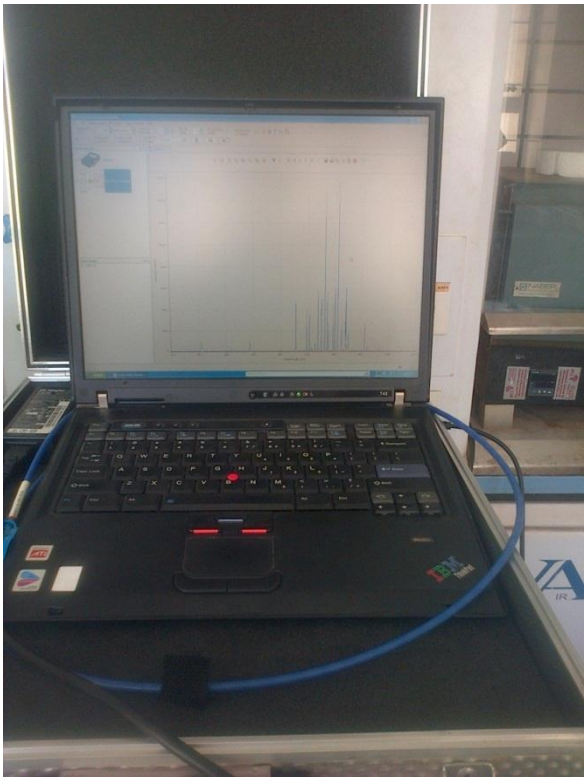

Figure 44: Ocean Optics spectrometer

5.5 Summary

The experimental methodology, equipment and setup were described and supported through the use of schematic diagrams and photos of the equipment used. The experimental design followed a central composite design, and each step of the experimental run was described systematically. The mass flow rate of MTS was calibrated and the results reported.

CHAPTER 6
Results and discussion

6.1 Introduction

This chapter presents the results of the experimental investigation into the conversion of MTS to SiC in a microwave plasma environment operating at atmospheric pressure. The results are discussed as they are presented. Section 6.2 offers the results of the mass and energy balances for each component entering the system. This includes the rate of formation of SiC and the yield. In section 6.3, the thermodynamic simulations are given and discussed with regard to optimum conversion temperature. Scanning and transmission electron microscopy results are given in section 6.4, along with particle size distribution and X-ray diffraction results. Statistical analyses on the particle size results are presented and interpreted in sections 6.5 and 6.6. Finally, the emission spectrography results are discussed in section 6.7.

6.2 Mass and energy balance

In order to determine the yield and conversion, it becomes necessary to determine the overall mass balance, which can then be compared with the actual results of the experiment. The resulting mass balance is given in Table 13. Gas flow rates, denoted by Q_i, are given in standard cubic centimetres per minute. The total forwarded power, P_f, is determined through:

$$\boldsymbol{P_f = P_T - P_r} \tag{6.1}$$

where P_r is the reflected power and P_T is the total power. Enthalpy, H_{TOT}, is determined through:

$$H_{TOT} = \frac{P_f}{\dot{m}_{TOT}} \tag{6.2}$$

where $\dot{m}_{\mathrm{TOT}}$ is the total mass flow rate. Note that the enthalpy value given is the system enthalpy, which applies to all the components (argon, hydrogen and MTS) combined.

Table 13: Mass and energy balance

Exp. number	Q_{Ar} (sccm)	Q_{H_2} (sccm)	$Q_{Ar/MTS}$ (sccm)	P_T (W)	P_r (W)	$\dot{m}_{MTS}$ (g/min)	H_2:MTS (mol:mol)	$\dot{m}_{TOT}$ (kg/s)	H_{TOT} (MJ/kg)
1	150	30	30	400	0	0.044	4.1	0.0000057	70.5
2	150	55	30	570	0	0.044	7.6	0.0000057	99.8
3	150	40	25	560	0	0.026	9.4	0.0000052	106.8
4	150	55	30	1300	200	0.044	7.6	0.0000057	192.6
5	150	30	30	1500	400	0.044	4.1	0.0000057	193.8
6	150	10	30	1300	400	0.044	1.4	0.0000056	159.3
7	150	0	30	870	300	0.044	0.0	0.0000056	101.1
8	150	10	30	570	0	0.044	1.4	0.0000056	100.9
9	150	30	30	950	100	0.044	4.1	0.0000057	149.7
10	150	30	30	950	100	0.044	4.1	0.0000057	149.7
11	150	30	30	950	100	0.044	4.1	0.0000057	149.7
12	150	30	30	1500	300	0.044	4.1	0.0000057	211.4

Experiment no. 3 yielded no results due the constant “starving” of the plasma at these high hydrogen ratios. The resulting experimental points are shown in Figure 45.

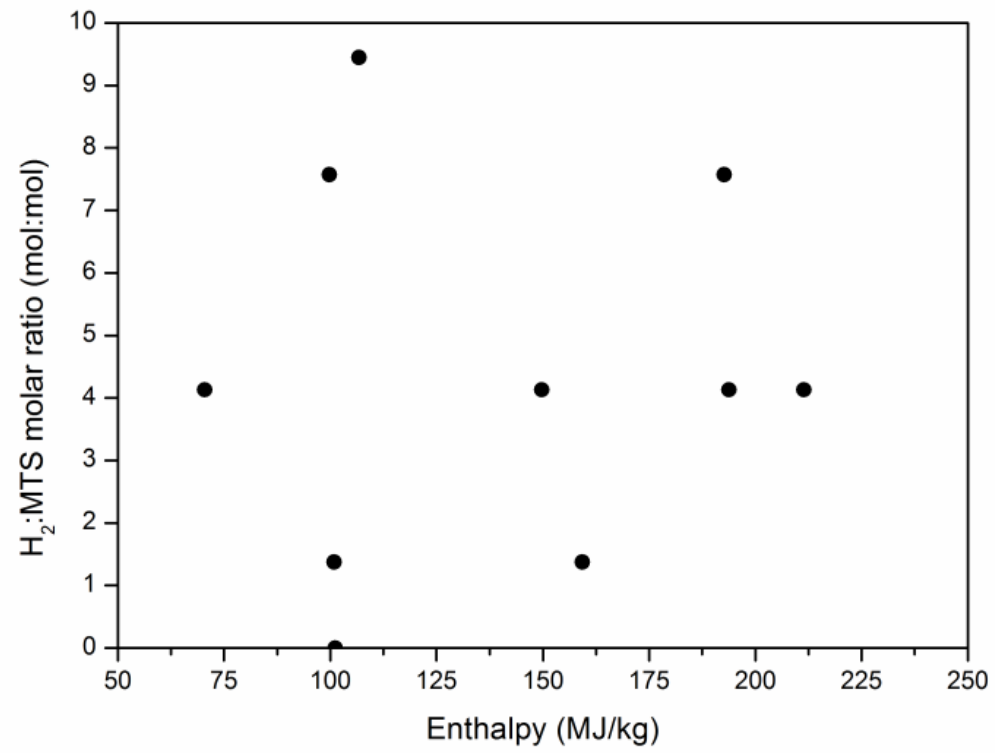

Figure 45: Experimental points

The deposited yield is determined with Table 13 and shown in Table 14. The initial mass of the quartz tube, m_i, was subtracted from the final mass after each experiment, m_f, and the resulting rate of SiC production was determined through Equation 6.3:

$$\dot{R}_{SiC} = \frac{m_f - m_i}{t} \tag{6.3}$$

The resulting yield, Y, was calculated by:

$$Y = \left(\frac{\dot{R}_{SiC}}{\dot{m}_{MTS}}\right)\left(\frac{MM_{SiC}}{MM_{MTS}}\right)100 \tag{6.4}$$

These values are, however, subject to scrutiny, as some of the SiC particles were lost through the system. Also, the powders collected on the quartz tubes can be composed of other materials beside SiC.

Table 14: Yield calculations and results

Exp. number	Time, t (s)	Tube, m_i (g)	Tube, m_f (g)	$\dot{R}_{SiC}$ (g/min)	Y %
1	18	93.011	93.018	0.023	14
2	20	71.388	71.389	0.003	2
3	0	-	-	-	-
4	70	92.543	92.567	0.020	12
5	180	92.479	92.597	0.039	24
6	180	92.537	92.587	0.017	10
7	180	93.022	93.050	0.009	6
8	180	92.953	93.066	0.037	23
9	180	92.748	92.794	0.015	9
10	148	93.011	93.047	0.015	9
11	180	71.330	71.390	0.020	12
12	180	92.600	92.637	0.012	7

Using Design Expert® 9, the results were analysed through the application of response surface methodology (RSM) and a 2D contour plot, shown in Figure 46, was produced. The fit was obtained by using a quadratic model incorporating a cross-term. This surface plot infers an optimum area for conversion along a line from an H_2:MTS ratio of 1.7 (from the far left) to 5.1 (to the far right).

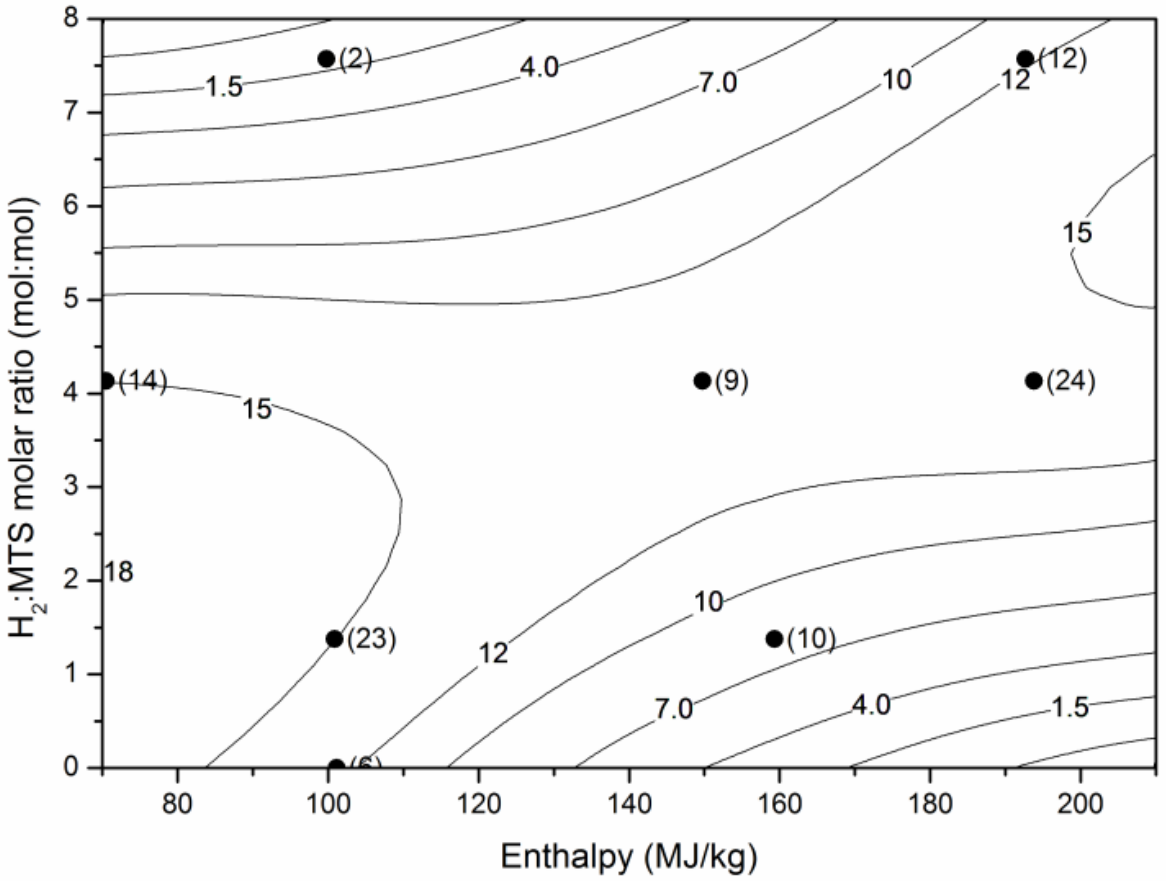

Figure 46: Surface contour plot of yield results

6.3 Thermodynamic simulations

The equilibrium thermodynamics and formation mechanisms of this reaction have been reported in the literature (Deng *et al*., 2009). The optimum conditions for the formation of β-SiC were confirmed using the thermodynamics package TERRA (Trusov, 2006). The results are plotted in Figure 47 and Figure 48.

The enthalpy required to convert MTS into SiC is given in Figure 48, under equilibrium thermal conditions. The experimental specific enthalpy values listed in Table 13 are significantly lower than the thermal values of Figure 48, suggesting that the non-equilibrium nature of the plasma plays a significant role in the MTS decomposition process.

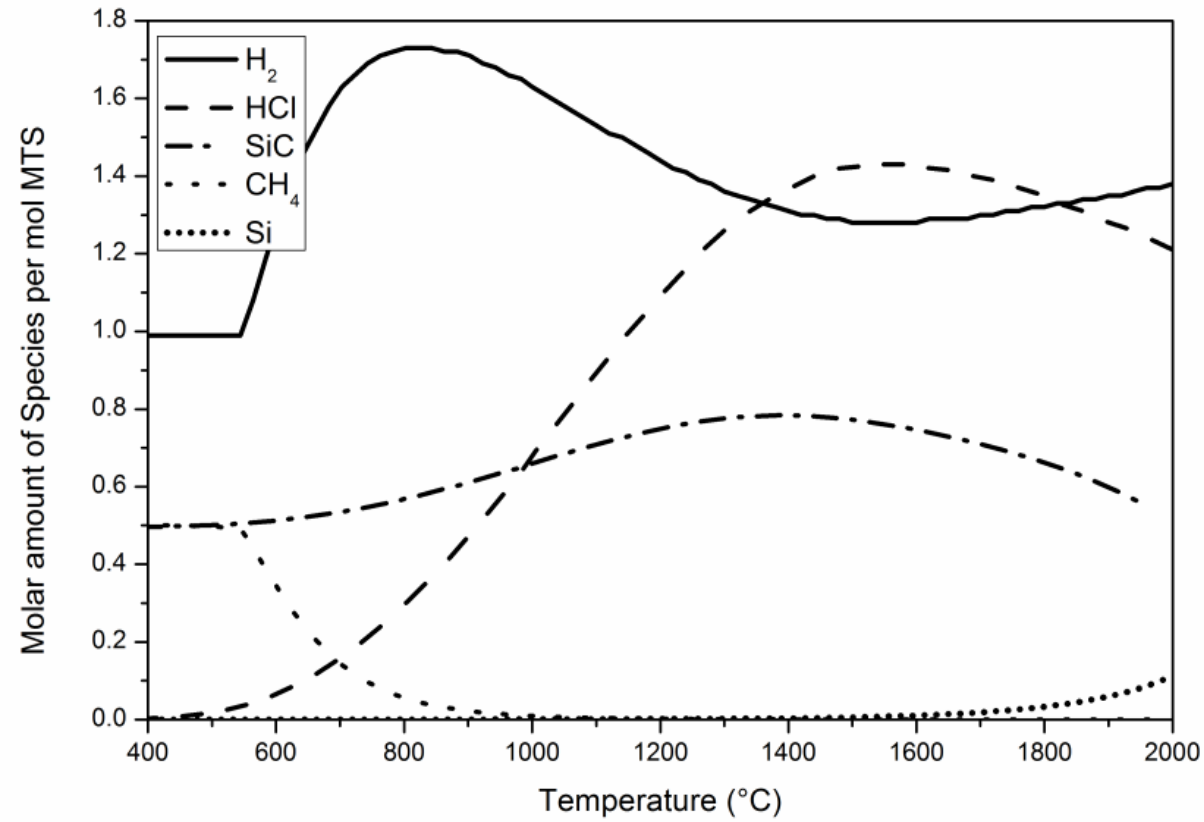

Figure 47: Conversion of MTS at different temperatures

At temperatures of approximately 1 400 K and above (Figure 47), optimum yield for β-SiC formation is obtained. Microwave plasmas can operate anywhere within the region of 1 500 to 10 000 K (Tendero *et al.*, 2006). Exact control of the gas temperature was not attempted or measured during this experiment due to the complicated nature of such a measurement.

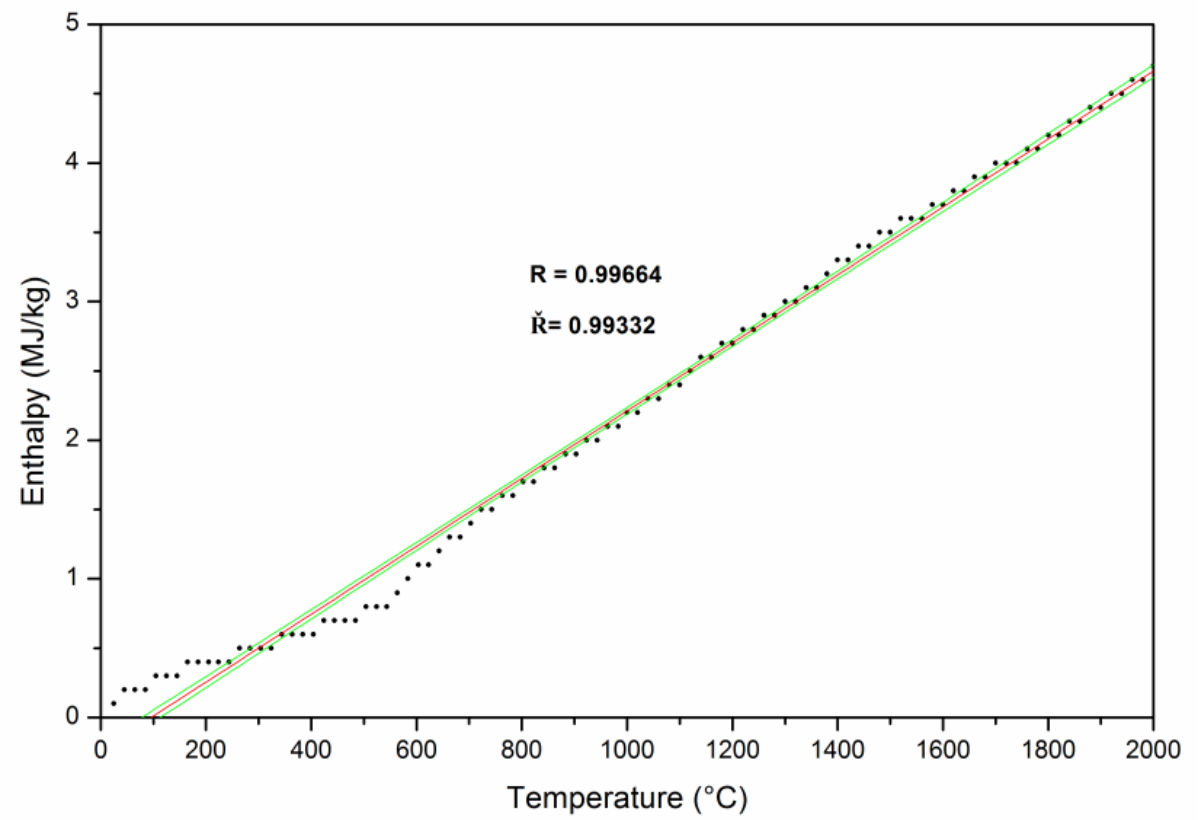

Figure 48: Enthalpy of SiC vs system temperature under equilibrium thermal conditions

6.4 Nanoparticle analysis

6.4.1 X-Ray diffraction

The presence of SiC particles was confirmed through the use of X-ray diffraction techniques. The resulting X-ray diffraction pattern (XRD) is shown in Figure 49, indicating diffraction peaks at positions typical of β-SiC (cubic).

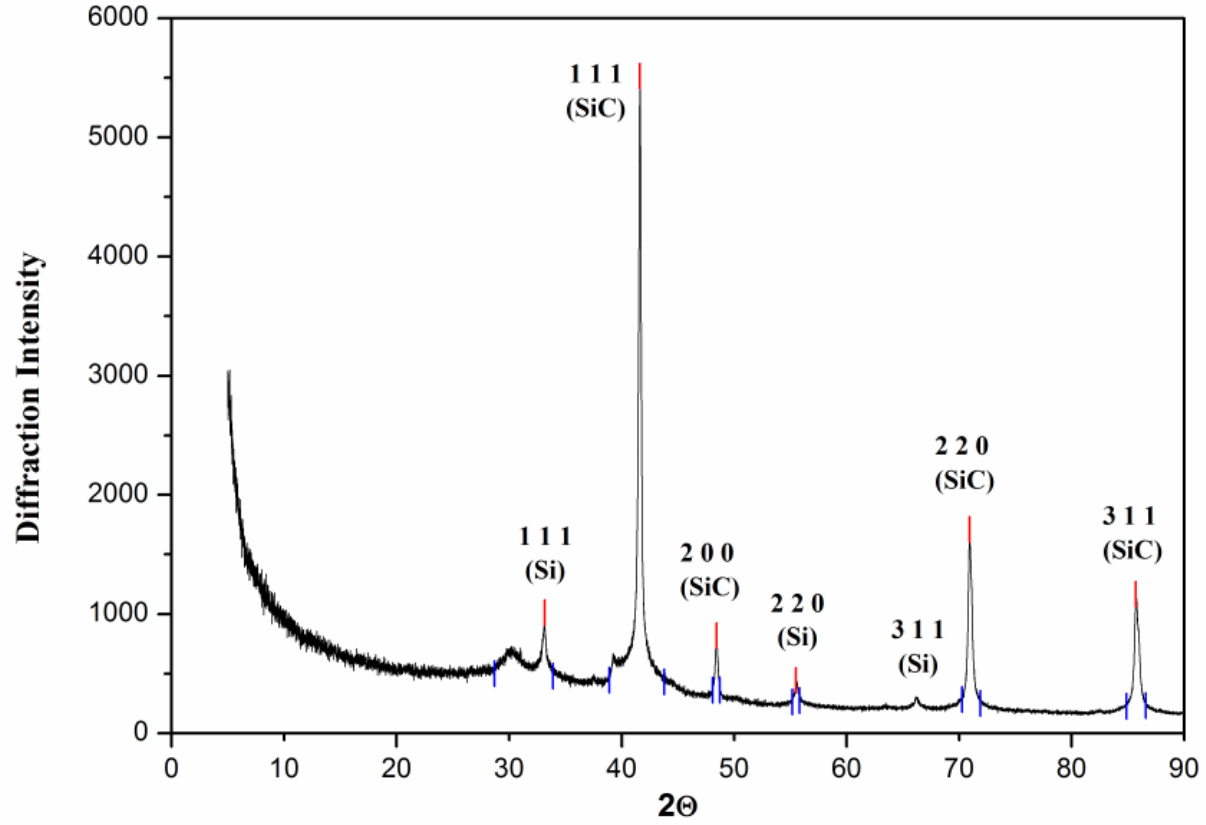

Figure 49: XRD spectrum of a product sample synthesised at an H_2:MTS ratio of 4; SiC refers to the β phase

6.4.2 Scanning electron microscopy

The presence of nanoparticles was confirmed through the use of SEM. Each experiment showed the presence of SiC nanoparticles within the range of 50 to 135 nm. The SEM photographs from experiments 4, 11 and 12 are displayed in Figure 50, Figure 51 and Figure 52. These images show that large agglomerates are formed.

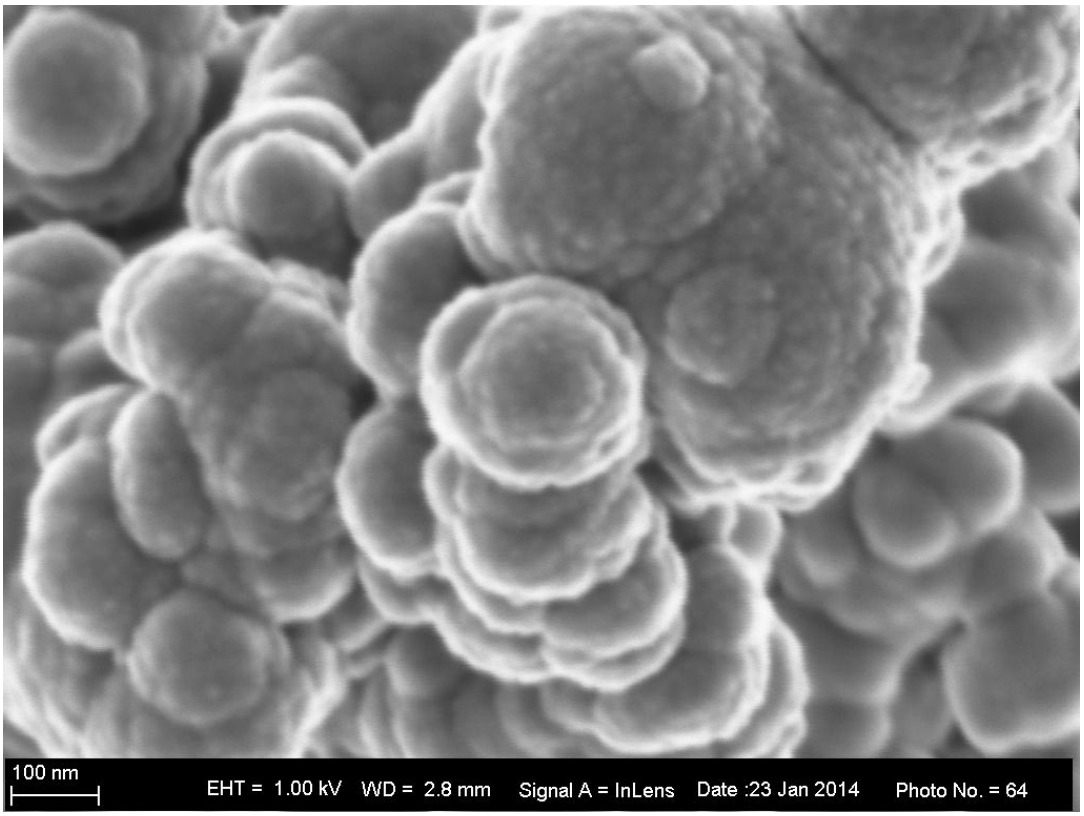

Figure 50: SEM micrograph from experiment no. 12

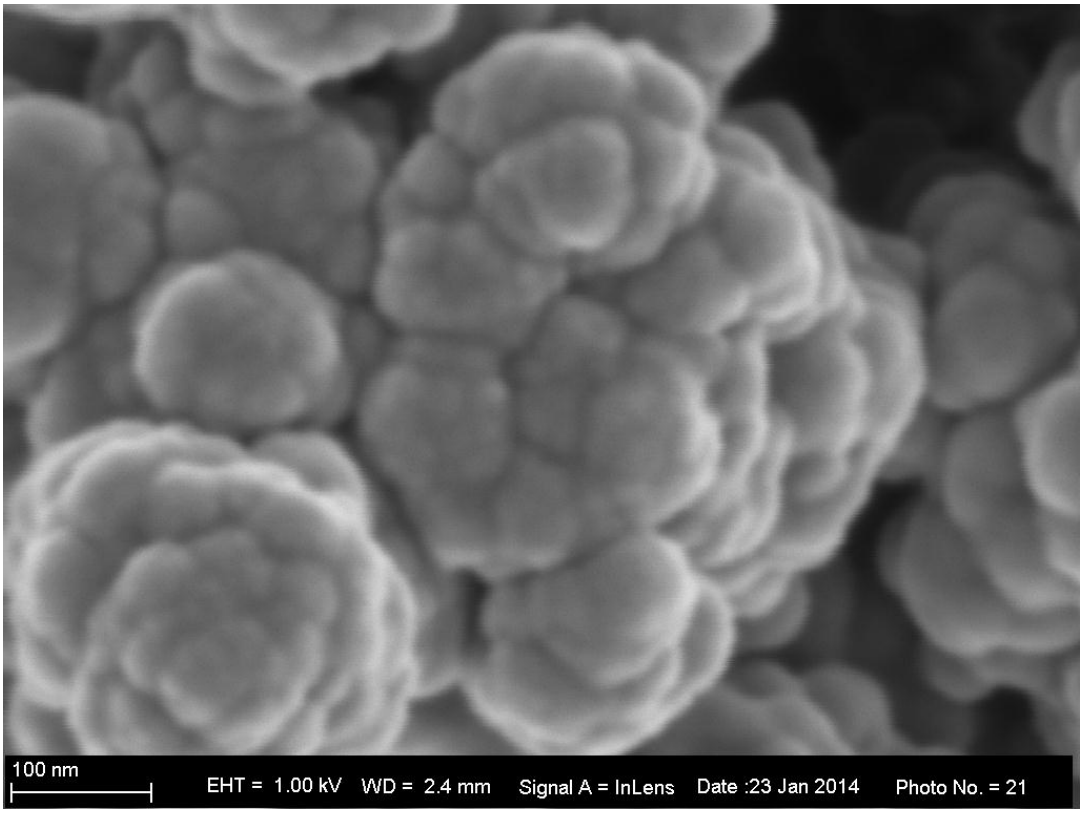

Figure 51: SEM micrograph from experiment no. 4

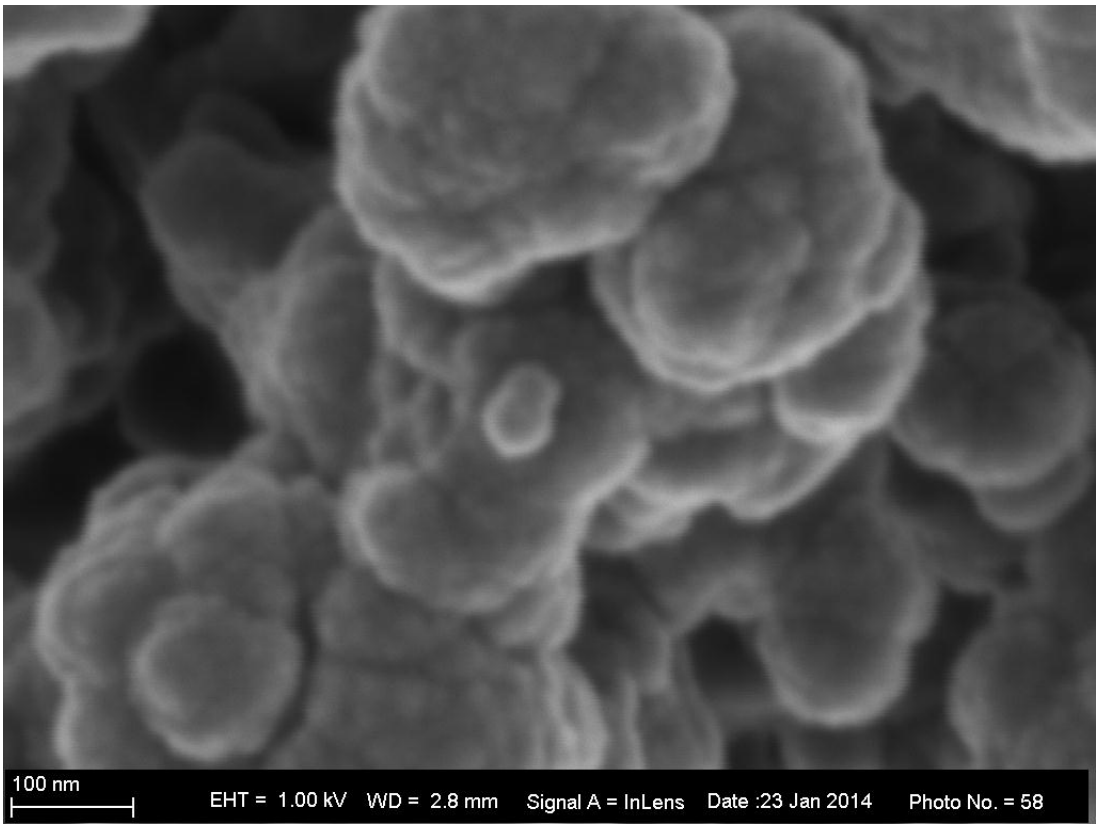

Figure 52: SEM micrograph from experiment no. 11

The individual particle sizes were measured and the aggregate results are shown in Table 15.

Table 15: Particle sizes from SEM micrographs

Exp. number	1	2	3	4	5	6	7	8	9	10	11	12
Particle size, d_p (nm)	89	82	-	68	111	53	132	132	110	131	91	121

6.4.3 Transmission electron microscopy

The results from experiments 6 and 11, displayed with the help of a TEM, are shown in Figure 53, Figure 54 and Figure 55.

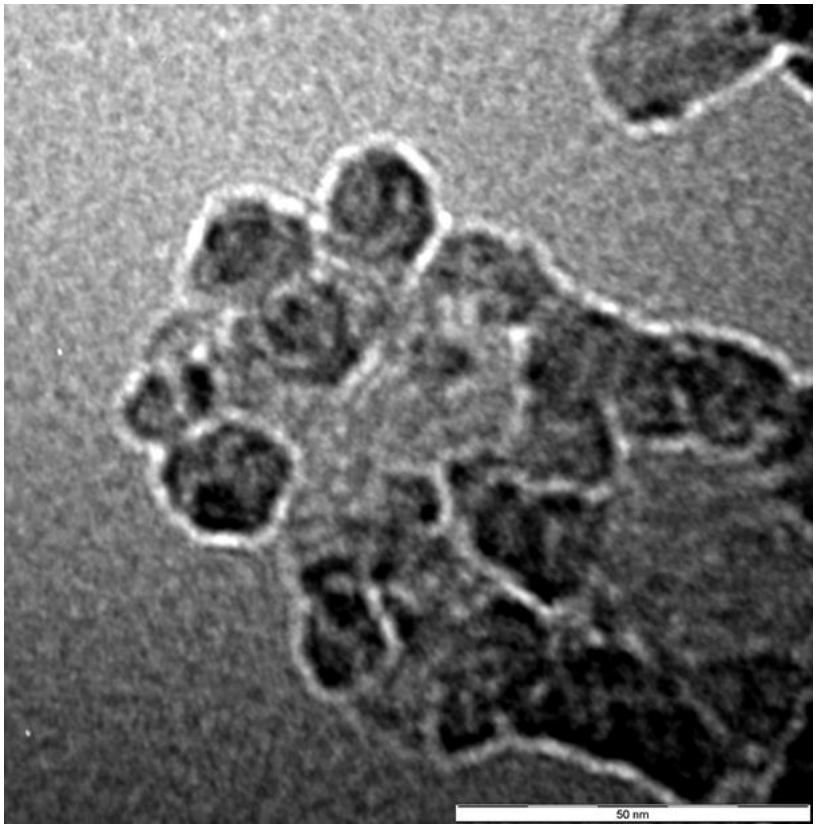

Figure 53: TEM image from experiment 6 showing individual particle sizes

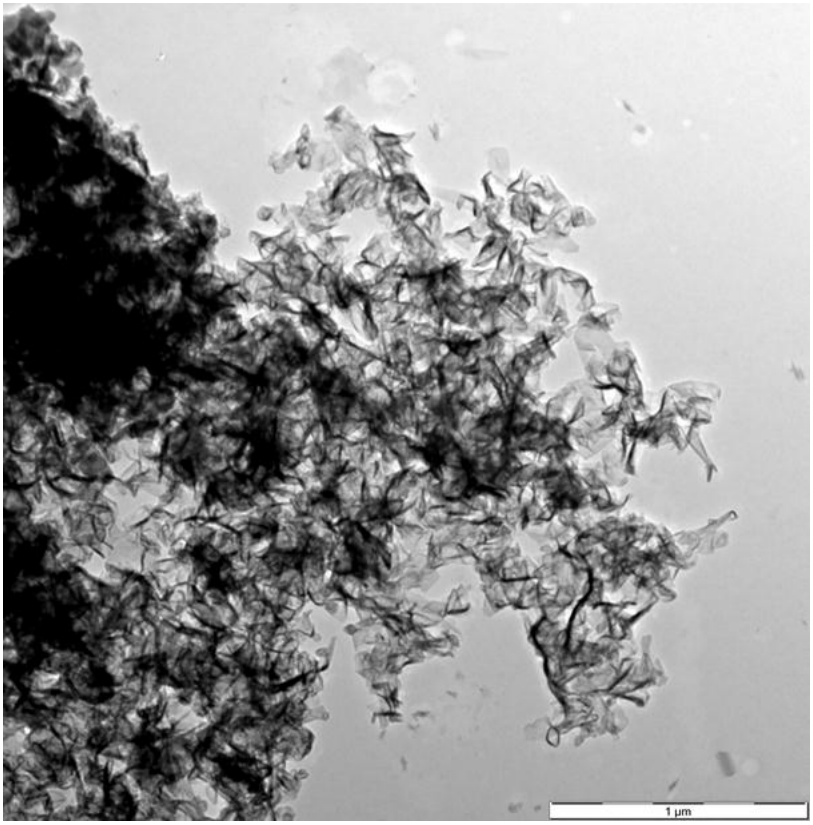

Figure 54: TEM image from experiment 6 showing agglomerates

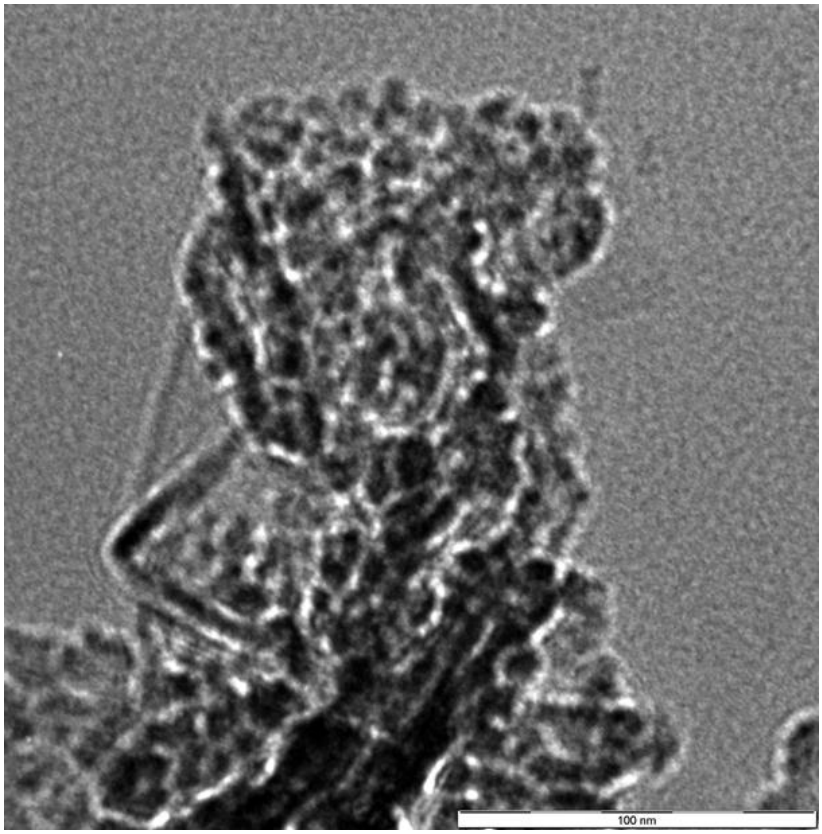

Figure 55: TEM image from experiment 11

6.4.4 Particle size distribution

The average agglomerate sizes were determined by a Zetasizer, and the results are given in Table 16.

Table 16: Zetasizer results of average agglomerate sizes

Exp. number	1	2	3	4	5	6	7	8	9	10	11	12
Zetasizer d_p, (nm)	1296	1743	-	461	483	590	1233	800	744	634	675	475

6.5 Response surface methodology

Using Design Expert 9, the results of the previous three sections were analysed through RSM. This method is used to explore the relationships between several explanatory variables and one or more response variables in order to obtain an optimal response. This is achieved through the use of a sequence of designed experiments and using a second-degree polynomial model.

6.5.1 SEM results

The individual particle sizes extracted from the SEM images were analysed and the resulting surface contour plot is shown in Figure 56. The fit was obtained using a quadratic model incorporating cross-terms.

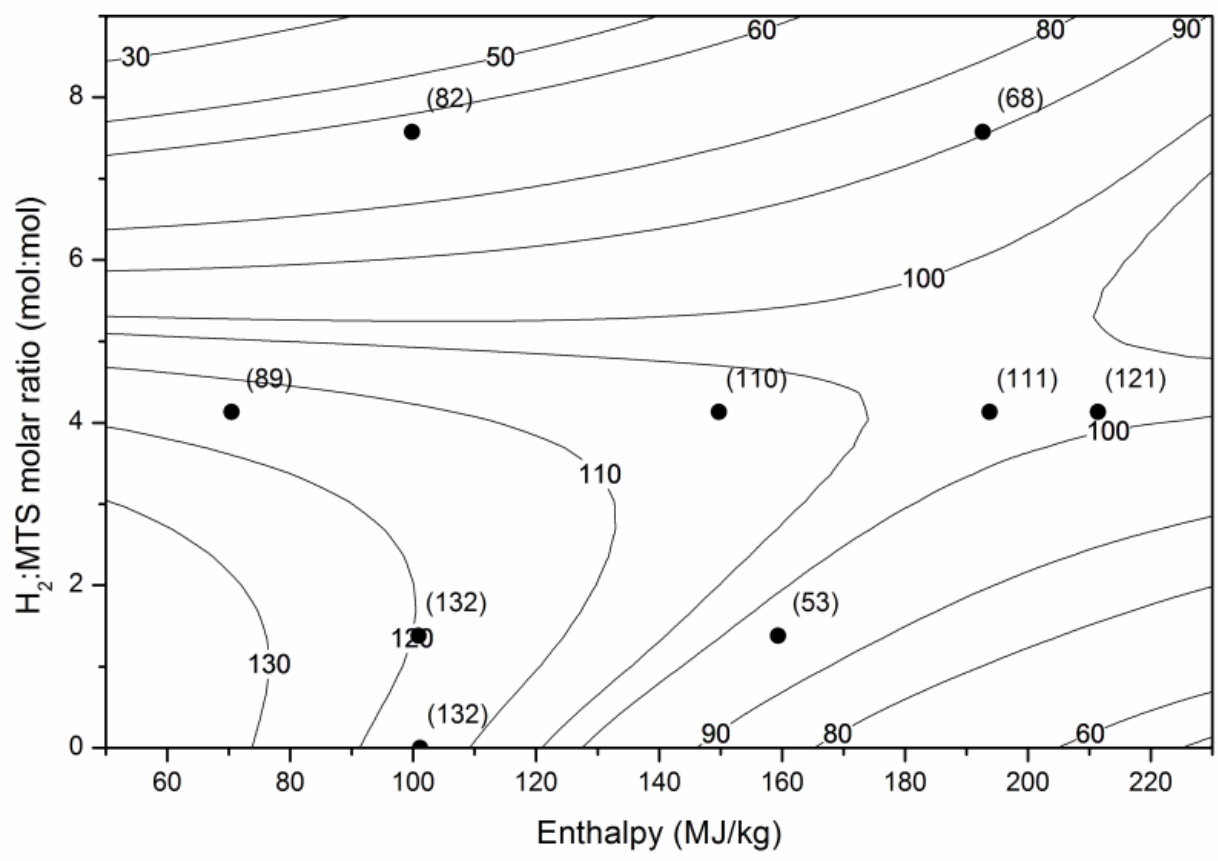

Figure 56: 2D surface contour plot of SEM results

When enthalpy and the H_2:MTS ratio increase, the average particle sizes decrease. The optimum conditions for the production of nanoparticles would therefore lie within the area of enthalpy > 180 MJ/kg and an H_2:MTS ratio of > 5. From the RSM results, it is noticeable that the H_2:MTS ratio seems to affect the agglomerated particle sizes negatively at higher ratios, whereas the opposite is true for individual particle sizes.

6.5.2 Zetasizer results

Agglomerate particle sizes are much larger than the individual particle sizes. The RSM results show that the agglomerate sizes prefer different conditions than those of individual particle sizes, as seen in Figure 57.

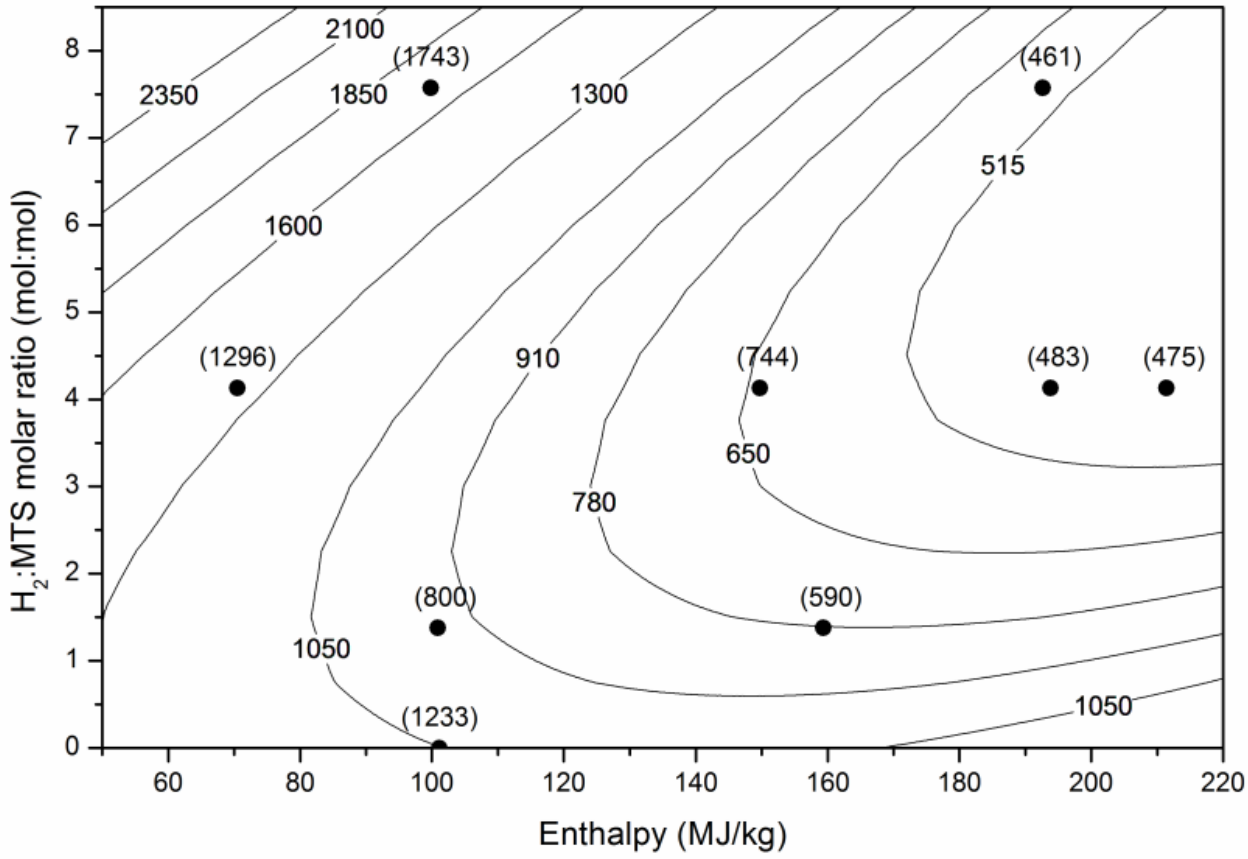

Figure 57: 2D surface contour plot of agglomerate sizes

This figure illustrates that agglomerate sizes are increased at high H_2:MTS ratios and low enthalpies. At larger enthalpy values, however, the addition of hydrogen may considerably decrease the agglomerate sizes.

6.6 Analysis of variance (ANOVA)

In their simplest form, ANOVA models test whether the means of several groups are equal by generalising the t-test to more than two groups. Usually the ANOVA test is only used in the analysis of comparative experiments, where the difference in outcomes is of interest. An experiment is determined to be statistically significant, or not, by a ratio of two variances that is independent of possible changes to the experimental observations.

There is a complication, however, when using ANOVA to study the effects of multiple factors. For example, in a three-factor ANOVA, the model includes terms for both the main effects (x, y, z) and interactions (xy, xz, yz, xyz). This increase in the number of interaction terms also increases the risk that some tests will produce a false positive by chance.

6.6.1 ANOVA of SEM results

The ANOVA results of the individual particle sizes, as determined from SEM micrographs, are given in Table 17 and continue in Table 18. A brief discussion of the results follows.

The model F-value of 0.43 implies that the model is not significant relative to the noise. There is an 80.95% chance that an F-value this large could occur due to noise.

Table 17: ANOVA for response surface quadratic model of SEM results

Source	Sum of squares	df	Mean square	F-value	p-value Prob > F	
Model	2262.17	5	452.43	0.43	0.81	not significant
A-enthalpy	112.82	1	112.82	0.10	0.76	
B-H_2:MTS	585.03	1	585.03	0.56	0.49	
AB	661.22	1	661.22	0.63	0.46	
A^2	2.96	1	2.96	0.00	0.96	
B^2	762.94	1	762.94	0.73	0.43	
Residual	5211.65	5	1042.33			
Lack of fit	4378.24	3	1459.41	3.50	0.23	not significant
Pure error	833.41	2	416.71			
Cor total	7473.82	10				

Values of "prob > F" less than 0.0500 indicate that the model terms are significant. In this case, there are no significant model terms. Values greater than 0.1000 indicate that the model terms are not significant. If there are many insignificant model terms, model reduction may improve the model.

The "lack of fit" model F-value of 3.50 implies that the lack of fit is not significant relative to the pure error. There is a 23.00% chance that a "lack of fit F-value" this large could occur due to noise. Non-significant lack of fit is preferable.

Table 18: ANOVA of SEM results (continued)

Std. Dev.	32.29	R-squared	0.30
Mean	101.75	Adj R-squared	-0.39
C.V. %	31.73	Pred R-squared	-15.93
PRESS	126539.40	Adeq precision	2.31

A negative "pred R-squared" implies that the overall mean is a better predictor of the response than the current model. "Adeq precision" measures the signal-to-noise

ratio. A ratio of 2.31 indicates an inadequate signal and that this model should not be used to navigate the design space.

6.6.2 ANOVA of Zetasizer results

The ANOVA results of the agglomerate sizes, as determined from Zetasizer results, are given in Table 19 and continue in Table 20. A brief discussion of the results follows.

Table 19: ANOVA for response surface quadratic model of Zetasizer results

Source	Sum of squares	df	Mean square	F-value	p-value Prob > F	
Model	1600171.00	5	320034.30	12.92	0.0070	significant
A-enthalpy	765238.10	1	765238.10	30.88	0.0026	
B-H_2:MTS	51635.30	1	51635.30	2.08	0.2085	
AB	177041.70	1	177041.70	7.14	0.0442	
A^2	42770.98	1	42770.98	1.73	0.2460	
B^2	194981.50	1	194981.50	7.87	0.0378	
Residual	123893.20	5	24778.65			
Lack of fit	117712.60	3	39237.52	12.70	0.0739	not significant
Pure error	6180.67	2	3090.33			
Cor total	1724065.00	10				

The model F-value of 12.92 implies that the model is significant. There is only a 0.69% chance that an F-value this large could occur due to noise.

Values of “prob > F” less than 0.0500 indicate that model terms are significant. In this case, A, AB and B^2 are significant model terms. Values greater than 0.1000 indicate that the model terms are not significant.

The “lack of fit” model F-value of 12.70 implies that there is a 7.39% chance that a “lack of fit” F-value this large could occur due to noise. Lack of fit is undesirable. This relatively low probability (<10%) is troubling.

Table 20: ANOVA of Zetasizer results (continued)

Std. Dev.	157.41	R-squared	0.93
Mean	830.36	Adj R-squared	0.86
C.V. %	18.96	Pred R-squared	-0.05
PRESS	1808306.00	Adeq precision	11.07

A negative “pred R-squared" implies that the overall mean is a better predictor of the response than the current model. "Adeq precision" measures the signal-to-noise ratio. A ratio greater than 4 is desirable. A ratio of 11.07 indicates an adequate signal. This model can be used to navigate the design space.

6.7 Emission spectrometry

An optical emission spectrometer was used to determine the elements present in the plasma environment. This is a standard diagnostic tool often used to monitor discharge emissions (Cooper, 1966). An emission spectrum for wave lengths of 200 to 1 100 nm is shown in Figure 58. Some spectral lines are expected to be that of argon. The growth of nanoparticles in the plasma can drastically change the plasma properties, e.g. the electron energy distribution function. Layden *et al*. (2011) performed optical emission spectroscopy on an RF sputtering discharge in argon during dust particle growth to analyse this change. They found that the intensities of all the argon emission lines increase, indicating an increase in the number of high-energy electrons as a result of particle growth (Layden *et al.*, 2011). The majority of peaks in this case were determined to be that of elementary silicon, carbon and argon (Di *et al*., 2011; Kaneko *et al*., 2001; Kramida *et al*., 2014; Wagatsuma & Hirokawa, 1985), indicative of MTS decomposition in the plasma.

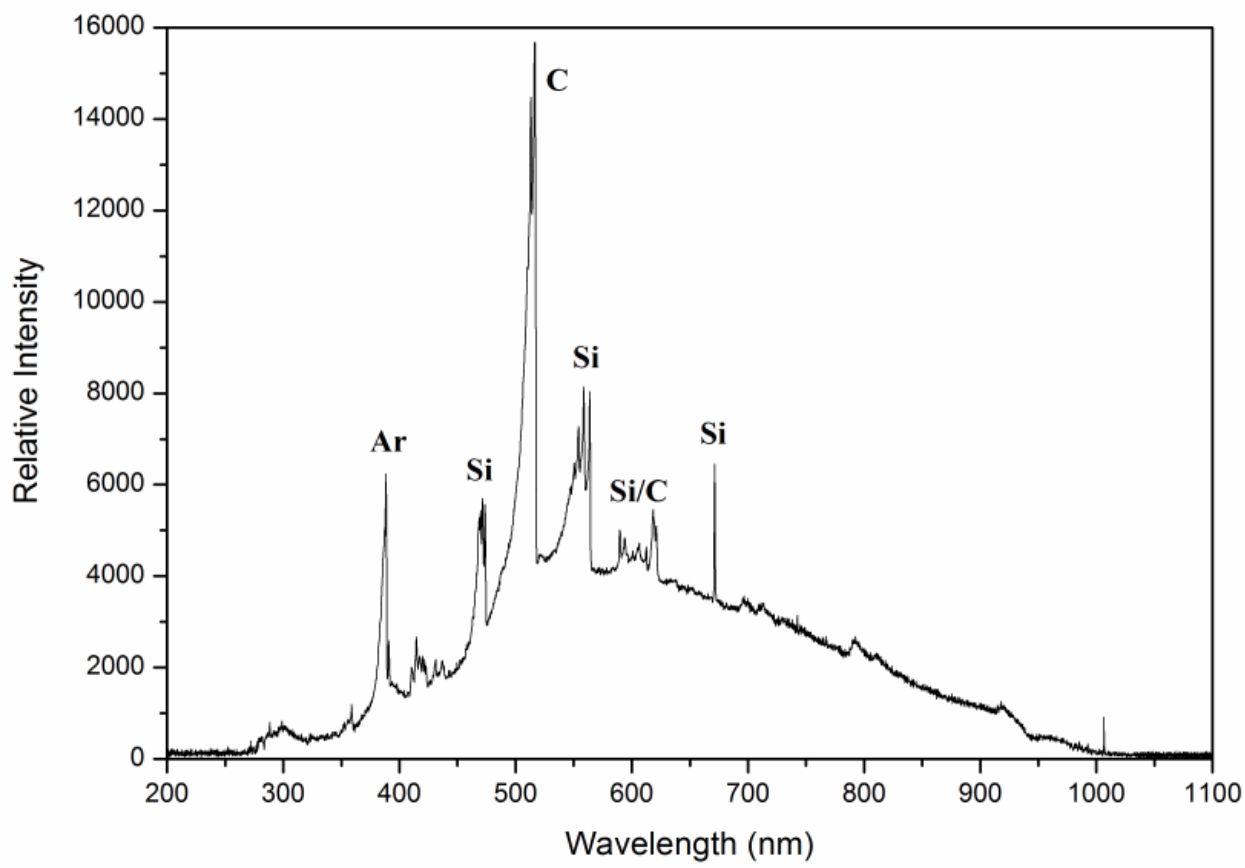

Figure 58: Emission spectograph of experiment 4

6.8 Summary

In this chapter, the experimental and statistical results of the experimental study were reported and discussed. X-ray diffraction confirmed the presence of β-SiC, and the conversion of MTS into SiC was supported by optical emission spectrograph interpretations. SEM and TEM results showed individual particle sizes down to 20 nm, and the zetasizer results showed agglomerate sizes down to 460 nm. Contour plots showed that the optimum conditions for the production of nanoparticles lie within the range of enthalpy > 180 MJ/kg and an H_2:MTS ratio of > 5.

CHAPTER 7

Summary, conclusions and recommendations

7.1 Summary

SiC nanoparticles have been shown to exhibit properties that differ substantially from that of the bulk material, encouraging the creation of new areas of application. Many different manufacturing methods for the creation of SiC nanoparticles have been reported in the literature.

The work of researchers such as Vennekamp *et al.* (2011) and Lin *et al.* (2008) has shown that it is possible to produce silicon carbide nanoparticles through the use of microwave plasmas operating at low to atmospheric pressures. However, a gap still exists in the literature with regard to this process and its potential applications.

In this study, the synthesis of SiC nanoparticles from MTS was reported using a microwave-induced plasma, operating at atmospheric pressure in an argon/hydrogen environment.

The research was done experimentally with a microwave generator operating at 2.45 GHz, a 1 500 W power supply, and a waveguide with stub tuners and a sliding short. The plasma environment was initiated and maintained in a quartz tube. The parameters studied were the H_2:MTS molar ratio and the total enthalpy, in the ranges 0 to 10 and 70 to 220 MJ/kg respectively. Particle characterisation and distribution was carried out with the help of SEM, TEM, zetasizer and X-ray diffraction results. The chemical reaction environment was studied using emission spectrographs.

7.2 Conclusions

Methyltrichlorosilane decomposes in a microwave plasma reactor to form SiC nanoparticles and HCl gas. When operating at atmospheric pressure, the

following particle sizes were obtained through further analysis of the resulting nanopowders:

- SEM results
  SEM micrographs of the SiC nanopowders showed average individual particle sizes ranging between 50 and 135 nm. Larger agglomerates were present.

- TEM results
  TEM micrographs of the SiC nanopowders showed average individual particle sizes ranging from 15 to 140 nm. Larger agglomerates were also present.

- Zetasizer
  The presence and sizes of agglomerates were again confirmed and measured using a zetasizer. The results showed agglomerate sizes ranging between 460 and 1 800 nm.

X-ray diffraction studies confirmed the presence of β-SiC, and an optical emission spectrometer was used to determine the elements present in the plasma environment. The majority of peaks were determined to be that of elementary silicon, carbon and argon, indicative of MTS decomposition in the plasma.

When enthalpy and the H_2:MTS ratio increase, the average particle sizes decrease. RSM results showed that the optimum conditions for the production of nanoparticles lie within the range of enthalpy > 180 MJ/kg and an H_2:MTS ratio of > 5. From the RSM results, it is noticeable that the H_2:MTS ratio seems to affect the agglomerated particle sizes negatively at higher ratios, whereas the opposite is true for individual particle sizes.

.

7.3 Recommendations

The conclusions clearly show that microwave plasmas have potential for the large-scale, low-cost synthesis of SiC nanoparticles. It is recommended that further research be applied to this area of development to determine its full potential uses.

8. References

Ahmed, Y.M.Z. and El-Sheikh, S.M. (2009) Influence of the pH on the Morphology of Sol-Gel-Derived Nanostructured SiC. *Journal of the American Ceramic Society*, *92*(11), 2724–2730.

Andrievski, R.A. (2009) Nano-sized silicon carbide: synthesis, structure and properties. *Russian Chemical Reviews*, *78*(9), 821–831.

Antsiferov, V., Khalturin, V. and Ainagos, A. (1998) Laser synthesis of ultrafine powders of silicon nitride and silicon carbide. *Powder Metallurgy and Metal Ceramics*, *37*(1-2), 33–36.

Baumann, H.N. (1952) The Relationship of Alpha and Beta Silicon Carbide. *Journal of The Electrochemical Society*, *99*(3), 109.

Bechstedt, F., Käckell, P., Zywietz, A., Karch, K., Adolph, B., Tenelsen, K. and Furthmüller, J. (1997) Polytypism and Properties of Silicon Carbide. *Physica Status Solidi (b)*, *202*(1), 35–62.

Beenakker, C. (1976) A cavity for microwave-induced plasmas operated in helium and argon at atmospheric pressure. *Spectrochimica Acta Part B: Atomic Spectroscopy*, *31B*(1976), 483–486.

Bilgic, A., Engel, U., Voges, E., Kückelheim, M. and Broekaert, J. (2000) A new low-power microwave plasma source using microstrip technology for atomic emission spectrometry. *Plasma Sources Science and Technology*, *9*(2000), 1–4.

Can, A. (2004) *Densification, Microstructure and Properties of Liquid-phase Sintered Silicon Carbide Materials*. *Doctoral thesis*. University of the Witwatersrand.

Cao, M., Gitzhofer, F., Gravelle, D.V, Henne, R. and Boulos, M.I. (1997) A torch nozzle design to improve plasma spraying techniques. *Plasma Sources Science and Technology*, *6*(1), 39–45.

Cardoso, R.P., Belmonte, T., Noël, C., Kosior, F. and Henrion, G. (2009) Filamentation in argon microwave plasma at atmospheric pressure. *Journal of Applied Physics*, *105*(9).

Chrisey, D.B. and Hubler, G.K. (1994) *Pulsed Laser Deposition of Thin Films*. New York: Wiley & Sons.

Conrads, H. and Schmidt, M. (2000) Plasma generation and plasma sources. *Plasma Sources Sci.*, *9*, 441–454.

Cooper, J. (1966) Plasma spectroscopy. *Reports on Progress in Physics*, *29*(1), 35.

Deng, J., Su, K., Wang, X., Zeng, Q., Cheng, L., Xu, Y. and Zhang, L. (2009) Thermodynamics of the gas-phase reactions in chemical vapor deposition of silicon carbide with methyltrichlorosilane precursor. *Theor Chem Account*, *122*, 1–22.

Dhage, S., Lee, H.C., Hassan, M.S., Akhtar, M.S., Kim, C.Y., Sohn, J.M., Kim, K., Shin, H. and Yang, O.B. (2009) Formation of SiC nanowhiskers by carbothermic reduction of silica with activated carbon. *Materials Letters*, *63*(2), 174–176.

Di, L., Shi, J.R., Wang, S.J., Dong, Q.L., Zhao, J., Li, Y.T., Fu, J., Wang, F., Shi, Y., Wan, B., Zhao, G. and Zhang, J. (2011) Emission Lines of Boron, Carbon, Oxygen and Iron in Tokamak Plasma. *Chinese Physics Letters*, *28*(7), 075201.

Fauchais, P. (2004) Understanding plasma spraying. *Journal of Physics D: Applied Physics*, *37*(9), R86–R108.

Fridman, A. (2008) *Plasma Chemistry*. New York: Cambridge University Press.

Fridman, A., and Kennedy, L.A. (2004) *Plasma physics and engineering*. CRC press.

Fu, L., Johnson, D.L., Zheng, J.G. and Dravid, V.P. (2003) Microwave Plasma Synthesis of Nanostructured γ-Al_2O_3 Powders. *Journal of the American Ceramic Society*, *86*(9), 1635–1637.

Gatti, M. and Kortshagen, U. (2008) Analytical model of particle charging in plasmas over a wide range of collisionality. *Phys. Rev. E*, *78*(4), 46402.

Giesen, B., Wiggers, H., Kowalik, A. and Roth, P. (2005) Formation of Si-nanoparticles in a microwave reactor: Comparison between experiments and modelling. *Journal of Nanoparticle Research*, *7*(1), 29–41.

Griem, H. (1963) Validity of Local Thermal Equilibrium in Plasma Spectroscopy. *Physical Review*, *131*(3), 1170–1176.

Guo, J.Y., Gitzhofer, F. and Boulos, M.I. (1997) Effects of process parameters on ultrafine SiC synthesis using induction plasmas. *Plasma Chemistry and Plasma Processing*, *17*(2), 219–249.

Harris, G.L. (1995) *Properties of Silicon Carbide*. Washington DC, USA: INSPEC.

Hollabaugh, C., Hull, D., Newkirk, L. and Petrovic, J. (1983) RF-plasma system for the production of ultrafine , ultrapure silicon carbide powder. *Journal of Materials Science*, *18*, 3190–3194.

Hong, Y., Uhm, H. and Cho, S. (2008) Argon Microwave Discharges Sustained at Atmospheric Pressure: Suppression of Plasma Filaments with Molecular Gases. *Journal of the Korean Physical Society*, *53*(6), 3220–3223.

Hull, D. and Bacon, D. (2001) *Introduction to Dislocations* (4th ed.). Liverpool, UK: Butterworth/Heinemann.

Inoue, Y., Nariki, Y. and Tanaka, K. (1989) Mechanism of production of ultra-fine silicon carbide powder by arc plasma irradiation of silicon bulk in methane-based atmospheres. *Journal of Materials Science*, *24*(11), 3819–3823.

Ishizaki, K., Egashira, T., Tanaka, K. and Celis, P. (1989) Direct production of ultra-fine nitrides (Si_3N_4 and AIN) and carbides (SIC , WC and TiC) powders by the arc plasma method. *Journal of Materials Science*, *24*, 3553–3559.

Izhevskyi, V.A., Genova, L.A., Bressiani, J.C. and Bressiani, A.H.A. (2000) Review article: silicon carbide. Structure, properties and processing. *Ceramica*, *46*(297), 4–13.

Janzen, C., Wiggers, H., Knipping, J. and Roth, P. (2001) Formation and in-situ sizing of gamma-Fe_2O_3 nanoparticles in a microwave flow reactor. *Journal of Nanoscience and Nanotechnology*, *1*(2), 221–225(5).

Kamlag, Y., Goossens, A., Colbeck, I. and Schoonman, J. (2001) Laser CVD of cubic SiC nanocrystals. *Applied Surface Science*, *184*(1-4), 118–122.

Kaneko, T., Miyakawa, N., Sone, H. and Yamazakia, H. (2001) The growth process and optical emission spectroscopy of amorphous silicon carbide films from methyltrichlorosilane by rf plasma enhanced CVD. *Surface and Coatings Technology*, *142-144*, 360–364.

Károly, Z., Mohai, I., Klébert, S., Keszler, A., Sajó, I.E. and Szépvölgyi, J. (2011) Synthesis of SiC powder by RF plasma technique. *Powder Technology*, *214*(3), 300–305.

Katoh, Y., Snead, L.L., Szlufarska, I. and Weber, W.J. (2012) Radiation effects in SiC for nuclear structural applications. *Current Opinion in Solid State & Materials Science*, *16*(3), 143–152.

Kavecky, S., Janekova, B., Madejova, J. and Pavol, S. (2000) Silicon carbide powder synthesis by chemical vapour deposition from silane / acetylene reaction system. *Journal of the European Ceramic Society*, *20*, 1939–1946.

Kim, B. and Lee, B. (2003) Effect of Plasma and Control Parameters on SiC Etching in a C_2F_6 Plasma. *Plasma Chemistry and Plasma Processing*, *23*(3), 489–499.

Knipping, J., Wiggers, H., Rellinghaus, B., Roth, P., Konjhodzic, D. and Meier, C. (2004) Synthesis of High Purity Silicon Nanoparticles in a Low Pressure Microwave Reactor. *Journal of Nanoscience and Nanotechnology*, *4*(8), 1039–1044.

Ko, S., Koo, S., Cho, W., Hwnag, K. and Kim, J. (2012) Synthesis of SiC nano-powder from organic precursors using RF inductively coupled thermal plasma. *Ceramics International*, *38*(3), 1959–1963.

Kogelschatz, U. (2000) Fundamentals and Applications of Dielectric-Barrier Discharges. *ABB Corporate Research*.

Kogelschatz, U. (2003) Dielectric-barrier Discharges: Their History , Discharge Physics, and Industrial Applications. *Plasma Chemistry and Plasma Processing*, *23*(1), 1–46.

Kogelschatz, U., Eliasson, B. and Egli, W. (1997) Dielectric-Barrier Discharges. Principle and Applications. *J. Phys IV France*, *7*(1997), 47–66.

Koinuma, H., Ohkubo, H., Hashimoto, T., Inomata, K., Shiraishi, T., Miyanaga, A. and Hayashi, S. (1992) Development and application of a microbeam plasma generator. *Applied Physics Letters*, *60*(7).

Kramida, A., Ralchenko, Y., Reader, J. and NIST ASD Team. (2014) NIST Atomic Spectra Database (ver. 5.2). Retrieved October 23, 2014, from http://physics.nist.gov/asd

Layden, B., Cheung, V. and Samarian, A.A. (2011) Effect of Dust Particle Growth on the Emission Spectrum of a Complex Plasma. *IEEE Transactions on Plasma Science*, *X*(X), 6–7.

Leconte, Y., Leparoux, M., Portier, X. and Herlin-Boime, N. (2008) Controlled Synthesis of β-SiC Nanopowders with Variable Stoichiometry Using

Inductively Coupled Plasma. *Plasma Chemistry and Plasma Processing*, *28*(2), 233–248.

Li, B., Zhang, C., Hu, H. and Qi, G. (2007) Preparation of nanosized silicon carbide powders by chemical vapor deposition at low temperatures. *Frontiers of Materials Science in China*, *1*(3), 309–311.

Li, J., Tian, J. and Dong, L. (2000) Synthesis of SiC precursors by a two-step sol-gel process and their conversion to SiC powders. *Journal of European Cermaic Society*, *77*, 1853–1857.

Lin, H., Gerbec, J.A., Sushchikh, M. and Mcfarland, E.W. (2008) Synthesis of amorphous silicon carbide nanoparticles in a low temperature, low pressure plasma reactor. *Nanotechnology*, *19*(325601), 1–8.

Massines, F. and Gouda, G. (1998) A comparison of polypropylene-surface treatment by filamentary, homogeneous and glow discharges in helium at atmospheric pressure. *Journal of Physics D: Applied Physics*, *31*(1998), 3411–3420.

Moisan, M., Sauvè, G., Zakrzewski, Z. and Hubert, J. (1994) An atmospheric pressure waveguide-fed microwave plasma torch: the TIA design. *Plasma Sources Science and Technology*, *3*, 584–592.

Moshtaghioun, B.M., Poyato, R., Cumbrera, F.L., de Bernardi-Martin, S., Monshi, A., Abbasi, M.H., Karimzadeh, F. and Dominguez-Rodriguez, A. (2012) Rapid carbothermic synthesis of silicon carbide nano powders by using microwave heating. *Journal of the European Ceramic Society*, *32*(8), 1787–1794.

Mousavipour, S.H., Saheb, V. and Ramezani, S. (2004) Kinetics and Mechanism of Pyrolysis of Methyltrichlorosilane. *The Journal of Physical Chemistry A*, *108*(11), 1946–1952.

Oh, S., Cappelli, M. and Park, D. (2002) Preparation of nano-sized silicon carbide powder using thermal plasma. *Korean Journal of Chemical Engineering*, *19*(5), 903–907.

Papasouliotis, G.D. and Sotirchos, S.V. (2011) Experimental study of atmospheric pressure chemical vapor deposition of silicon carbide from methyltrichlorosilane. *Journal of Materials Research*, *14*(08), 3397–3409.

Paschen, F. (1889) Ueber die zum Funkenübergang in Luft, Wasserstoff und Kohlensäure bei verschiedenen Drucken erforderliche Potentialdifferenz. *Annalen Der Physik*, *273*(5), 69–96.

Patnaik, P. (2002) *Handbook of Inorganic Chemicals*. USA: McGraw-Hill.

Payling, R. (2013) Glow Discharge dot Com. Retrieved September 03, 2013, from http://www.glow-discharge.com/?Physical_background:Glow_Discharges:Discharge_Regimes

Physandtech.net. (2001) Pulsed Laser Deposition (PLD). Retrieved November 02, 2014, from physandtech.net

Rao, N., Girshick, S., Heberlein, J., McMurry, P., Jones, S., Hansen, D. and Micheel, B. (1995) Nanoparticle formation using a plasma expansion process. *Plasma Chemistry and Plasma Processing*, *15*(4), 581–606.

Sachdev, H. and Scheid, P. (2001) Formation of silicon carbide and silicon carbonitride by RF-plasma CVD. *Diamond and Related Materials*, *10*(3-7), 1160–1164.

Saddow, S., & Agarwal, A. (2004) *Advances in silicon carbide processing and applications*. Norwood, USA: ARTECH HOUSE, INC.

Satapathy, L.N., Ramesh, P.D., Agrawal, D. and Roy, R. (2005) Microwave synthesis of phase-pure , fine silicon carbide powder. *Materials Research Bulletin*, *40*(2005), 1871–1882.

Schutze, A., Jeong, J.Y., Babayan, S.E., Park, J., Selwyn, G.S. and Hicks, R.F. (1998) The atmospheric-pressure plasma jet: a review and comparison to other plasma sources. *Plasma Science, IEEE Transactions on*, *26*(6), 1685–1694.

Shimada, M., Wang, W. and Okuyama, K. (2010) Synthesis of Gallium Nitride Nanoparticles by Microwave Plasma-Enhanced CVD. *Chemical Vapor Deposition*, *16*(4-6), 151–156.

Shukla, P. and Mamun, A. (2002) *Introduction to Dusty Plasma Physics*. Cornwall: Institute of Physics Publishing.

Smith, Z.G. (1991) *The Fabrication of Silicon Carbide heating elements*. University of Cape Town.

Sone, H., Kaneko, T. and Miyakawa, N. (2000) In situ measurements and growth kinetics of silicon carbide chemical vapor deposition from methyltrichlorosilane. *Journal of Crystal Growth*, *219*(3), 245–252.

Szabo, D.V. (2013) Microwave Plasma Syntheis of Nanoparticles: From Theoretical Background and Experimental Realization to Nanoparticles with Special Properties. In S. Horikoshi & N. Serpone (Eds.), *Microwaves in Nanoparticle Synthesis* (pp. 271 – 301). Weinheim: Wiley-VCH.

Taylor, P.R. and Pirzada, S.A. (1992) An Investigation of Silicon Carbide Synthesis in a Nontransferred Arc Thermal Plasma Reactor. *Metallurgical Transactions B*, *23*(August), 443–451.

Tendero, C., Tixier, C., Tristant, P., Desmaison, J. and Leprince, P. (2006) Atmospheric pressure plasmas: A review. *Spectrochimica Acta Part B: Atomic Spectroscopy*, *61*(1), 2–30.

Tong, L. and Reddy, R.G. (2006) Thermal plasma synthesis of SiC nano-powders/nano-fibers. *Materials Research Bulletin*, *41*(12), 2303–2310.

Trusov, B. (2006) Terra - Phase and Chemical Equilibrium of Multicomponent Systems. Moscow: Bauman Moscow State Technical University.

Vennekamp, M., Bauer, I., Groh, M., Sperling, E., Ueberlein, S., Myndyk, M., Mäder, G. and Kaskel, S. (2011) Formation of SiC nanoparticles in an atmospheric microwave plasma. *Beilstein Journal of Nanotechnology*, *2*, 665–673.

Voice, E. (1970) *The formation & structure of silicon carbide pyrolytically deposited in a fluidised bed of microspheres*. OECD Dragon High Temperature Reactor Project.

Wagatsuma, K. and Hirokawa, K. (1985) Characterization of Atomic Emission Lines from Argon , Neon , and Nitrogen Glow Discharge Plasmas. *Anal. Chem.*, *57*, 2901–2907.

Yao, S., Yamamoto, S., Kodama, S., Mine, C. and Fujioka, Y. (2009) Characterization of Catalyst-Supported Dielectric Barrier Discharge Reactor. *The Open Catalysis Journal*, *2*(1), 79–85.

Yaws, C.L. (2008) *Thermophysical Properties of Chemicals and Hydrocarbons*. Elsevier Science.

Yokoyama, T., Kogoma, M., Moriwaki, T. and Okazaki, S. (1990) A comparison of polypropylene-surface treatment by filamentary, homogeneous and glow discharges in helium at atmospheric pressure. *Journal of Physics D: Applied Physics*, *23*(1990), 1125–1128.

Young, R.M. and Pfender, E. (1985) Generation and behavior of fine particles in thermal plasmas: A review. *Plasma Chemistry and Plasma Processing*, *5*(1), 1–37.

Zhang, H.X., Feng, P.X., Makarov, V., Weiner, B.R., & Morell, G. (2009) Synthesis of nanostructured SiC using the pulsed laser deposition technique. *Materials Research Bulletin*, *44*(1), 184–188.

Zhu, C., Zhao, G., Revankar, V. and Hlavacek, V. (1993) Synthesis of ultra-fine SiC powders in a d.c. plasma reactor. *Journal of Materials Science*, *28*(1993), 659–668.

Zinkle, S. and Snead, L. (1998) Thermophysical and Mechanical Properties of SiC/SiC Composites. Oak Ridge National Laboratory.